Process intensification of Taylor-Couette flow reactor with complex fluids

Masuda, Hayato

(Degree)
博士（工学）
(Date of Degree)
2016-03-25
(Date of Publication)
2018-03-25
(Resource Type)
doctoral thesis
(Report Number)
甲第6644号
(URL)
https://hdl.handle.net/20.500.14094/D1006644

Doctoral Dissertation

博士論文

Process intensification of Taylor−Couette flow reactor with complex fluids

(テイラー・クエット流反応装置を用いた複雑流体プロセスの強化に関する研究)

January, 2016

平成 28 年 1 月

Graduate School of Engineering, Kobe University

神戸大学大学院　工学研究科

Hayato Masuda

増田　勇人

Contents

1. Introduction

2. Effective Reynolds number for Taylor–Couette with non-Newtonian fluids

3. Process intensification of continuous starch hydrolysis with a Taylor–Couette reactor

4. Gas–liquid two-phase Taylor–Couette flow with a ribbed inner cylinder

List of Achivements

1. Introduction

1. 1. Reactor design for achieving "Process Intensification"

"Process Intensification (PI)" has been attracting a great deal of attention in the field of chemical engineering. Imperial Chemistry Industries Ltd. in England first suggested the concept of PI for the construction of compact plants (Ramshaw, 1983). At the time of suggestion, "intensification" had the same meaning as "miniaturization of the reactor" because improvement of safety was the main objective. However, the definition of PI has changed over the decades. At present, the concept of PI as defined by Stankiewicz and Moulijn (2000) has been widely accepted. They defined PI as having the objective of making a quantum leap in process/plant efficiency with respect to space, time, energy, raw materials, environment, etc. From a practical viewpoint, PI can be regarded as a toolbox that is classified under two domains: a "hardware" domain (equipment) and a "software" domain (methods) as shown in **Fig. 1–1**. **Figure 1–1** also shows a number of examples of novel equipment and methods used to intensify chemical processes. Overlaps between these two domains are observed in several cases because new processes are required for PI (Stankiewicz, 2005).

Reay *et al.* (2008) proposed two strategies of reactor design leading towards PI:

1. PI significantly enhances transport rates.
2. PI gives every molecule the same processing experience.

If perfect mixing and heat/mass transfer within the reactor are accomplished, the reaction proceeds at its inherent rate. However, the reaction does not proceed at its inherent rate in a larger stirred tank reactor because it is limited by incomplete mixing, or the insufficient specific interfacial area for heat/mass transfer within the vessel. In order to perform the reaction at its inherent rate, it is necessary to remove such limitations. Thus, enhancement of transport rates, i.e. mixing and heat/mass transfer, is crucially important for PI. Moreover, the quality of products becomes uniform if every molecule experiences the same processing, leading to a reduction of byproducts. As a result, the total size of processes can be reduced because a post-processing apparatus, such as equipment for separation of byproducts, is unnecessary.

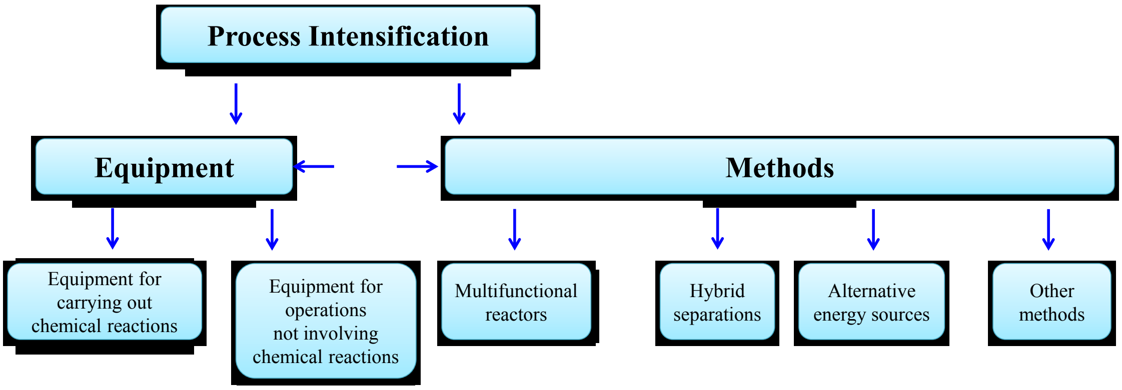

Examples

Spinning disk reactor Static mixer reactor Static mixing catalysts Monolithic reactors Heat exchange reactors Supersonic gas/liquid reactor Jet-impingement reactor Rotating packed-bed reactor	Static mixers Compact heat exchangers Microchannel heat exchanger Rotor/stator mixer Rotating packed beds Centrifugal absorber	Reverse-flow reactors Reactive distillation Reactive extraction Reactive crystallization Chromatographic reactors Periodic separating reactors Membrane reactors Reactive extrusion Reactive comminution Fuel cells	Membrane absorption Membrane distillation Adsorptive distillation	Centrifugal fields Ultrasound Solar energy Microwaves Electric fields Plasma technology	Supercritical fluids Dynamic (periodic) reactor operation

Fig. 1–1 Process intensification and its components, from the paper by Stankiewicz and Moulijn (2000)

Another important concept of PI is “conversion from batch to continuous operation”. Continuous reactors are usually smaller than equivalent batch reactors. Because batch vessels are tied to the ‘batch cycle’, meaning that much time is spent on processes such as filling, emptying, cleaning, heating and cooling, during which their space-time yield is reduced, the reactor does not generate the product during these processes (Boodhoo and Harvey, 2013). In contrast, the continuous operation leads to several benefits, such as:

- Improved control
- Better product quality
- Less hazardous operation
- Reduced running costs

In a continuous reactor, residence time distribution (RTD) is classified into “perfect mixed type (broad RTD)” and “plug flow type (narrow RTD)” (Levenspiel, 1999). In order to achieve tight control of processing history, the reactor having a plug flow property is desirable. Summarizing the strategy of reactor design to achieve PI, a continuous reactor that has both sufficient mixing performance and narrow RTD is necessary.

Conventional chemical processes usually have some “bottlenecks”. In order to achieve PI, bottlenecks for the system should be understood, and overcome based on the above-mentioned strategies of reactor design. As a result, new types of reactors are required for PI. For example, Jongen *et al.* (2003) applied a segmented flow tubular reactor (SFTR) to the synthesis process of fine particles, as shown in **Fig. 1–2**. In this process, the shear-rate in the reactor significantly affects the particle size distribution. The wider distribution of shear-rate in the conventional stirred tank reactor leads to a wider distribution of particle size. In order to overcome this bottleneck, uniform mixing is desirable. The SFTR is composed of a micromixer where the co-reactants are efficiently mixed, and a segmenter in which the reaction mixture is separated with immiscible fluid into micro-batch volumes or liquid "bubbles" in a continuous mode. Each micro-batch then circulates through a tube with identical residence times within the tubular reactor. The segmentation with the immiscible fluid produces a quasi-plug flow and avoids any back-mixing. Jongen *et al.* (2003) showed that the particles obtained using the SFTR has a narrow distribution of particle size and particles are more homogeneous compared to batch synthesis.

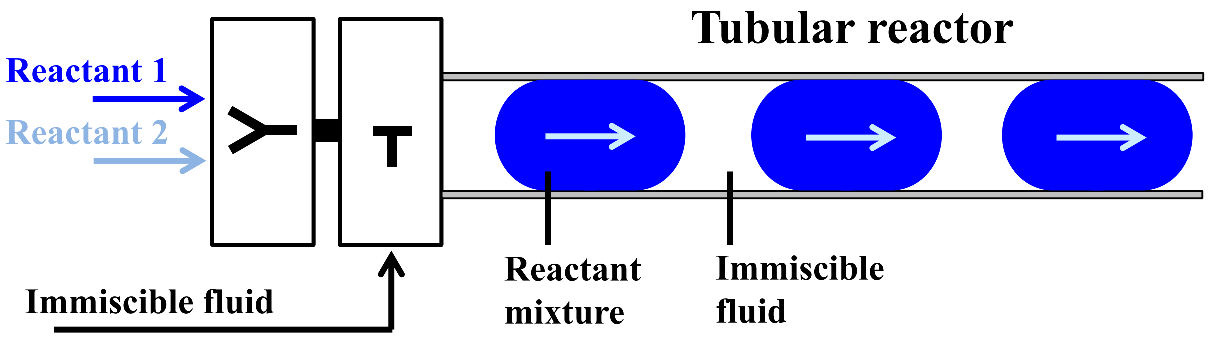

Fig. 1–2 Schematic picture of SFTR,
from the paper by Jongen *et al.* (2003)

Another successful example of process design for PI is an oscillatory baffled reactor (OBR) shown in **Fig. 1–3**. The OBR is a novel type of continuous reactor, in which tubes fitted with orifice plate baffles have an oscillatory motion superimposed upon the net flow of the fluid. The interaction of the baffles with the oscillatory motion of the fluid generates excellent mixing and enhanced transport rates, whilst maintaining a close approach to plug flow (Stonestreet and Harvey, 2002). Aiming at PI of bioprocess using the OBR, Ni *et al*. (1995) and Ni and Gao (1996) investigated the mass transfer characteristics between gas and liquid. Although the conventional stirred tank reactor is used in bioprocess, obtaining the sufficient gas hold–up and specific interfacial area is difficult. This is one of the bottlenecks of bioprocess. On the other hand, it is expected that vortices in the OBR capture more bubbles and this leads to higher gas hold–up and large specific interfacial area between gas and liquid. As a result, they successfully showed that the volumetric mass transfer coefficient in the OBR was on average 75% higher than the one in the conventional stirred tank at the same power density. Furthermore, Abbott *et al*. (2014) reported that the OBR has the potential to intensify the enzymatic saccharification process with lower power consumption than a stirred tank. As with the SFTR and OBR, a Taylor–Couette flow reactor has quite simple geometry and has potential for PI.

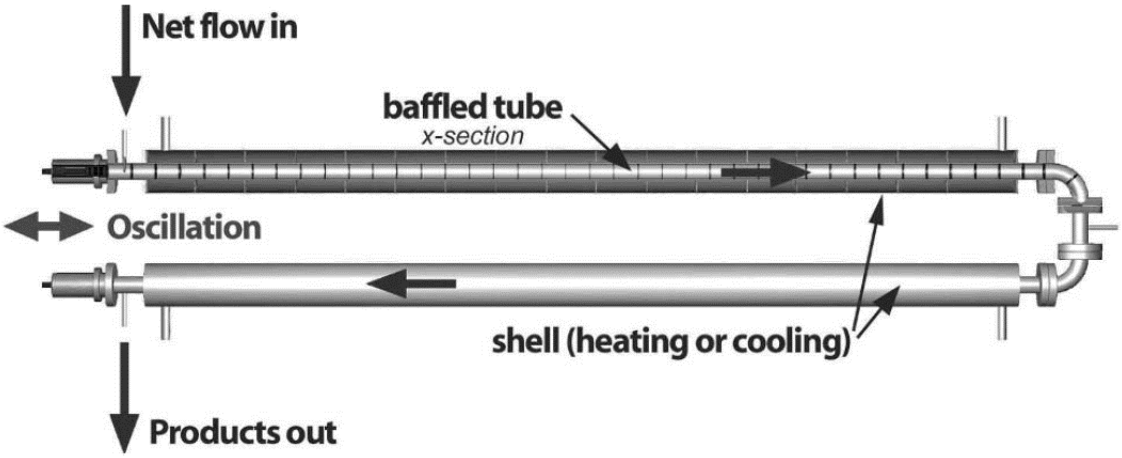

Fig. 1−3 Schematic picture of OBR,
from the paper by Stonestreet and Harvey (2002)

1. 2. Taylor−Couette flow reactor

The flow between two concentric cylinders with the inner one rotating has been studied from various points of view for many years. Taylor (1923) first investigated the instability of such a flow system and found that, when the Reynolds number (*Re*) exceeds a critical value, Re_{cr}, there appear pairs of counter-rotating toroidal vortices spaced regularly along the cylinder axis, arising from the basic shear flow (Couette flow), as shown in **Fig. 1−4**. *Re* is defined as follows,

$$Re = \frac{\rho R_{\mathrm{i}} \omega d}{\eta} \tag{1-1}$$

where ρ is the fluid density, R_{i} is the inner cylinder radius, ω is the angular velocity of inner cylinder, d is the gap width and η is the fluid viscosity. Taylor–Couette flow dynamics for Newtonian fluids has been investigated by many researchers (e.g. Davey, 1962; Coles, 1965; Andereck *et al*., 1986; Stuart, 1986; Kataoka, 1986).

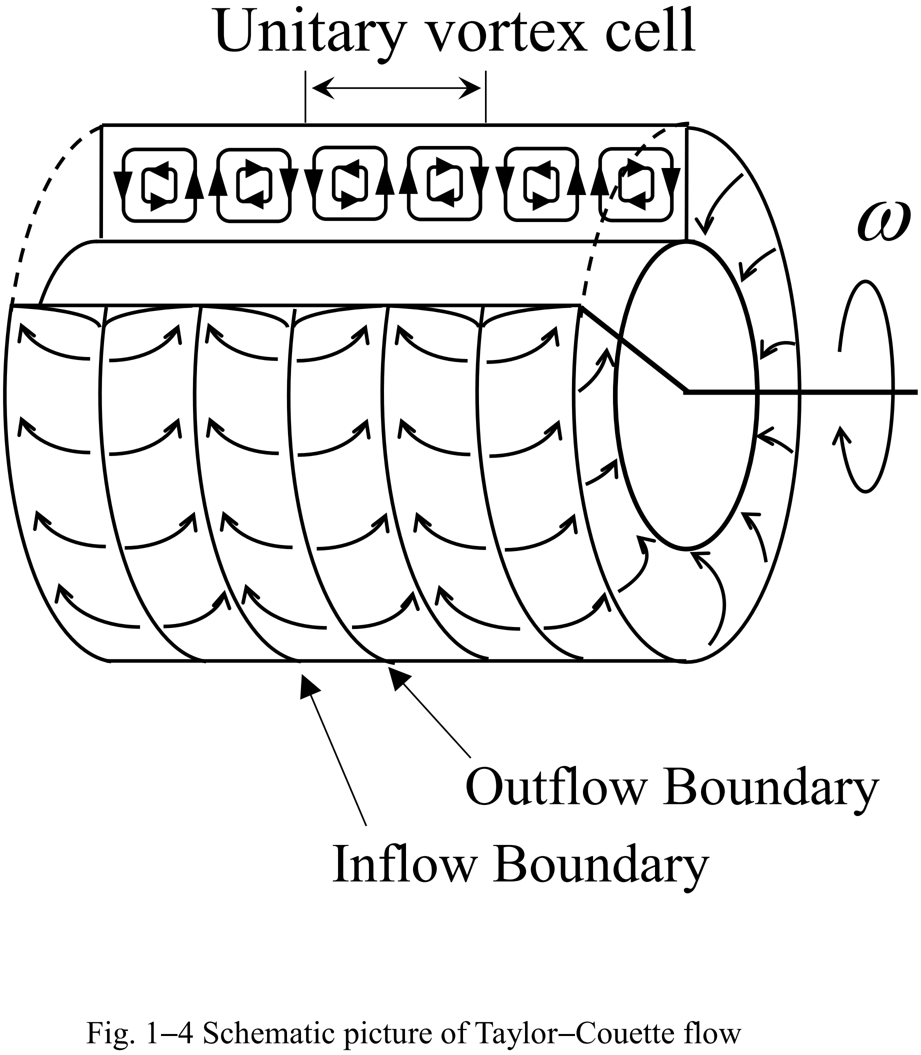

Fig. 1–4 Schematic picture of Taylor–Couette flow

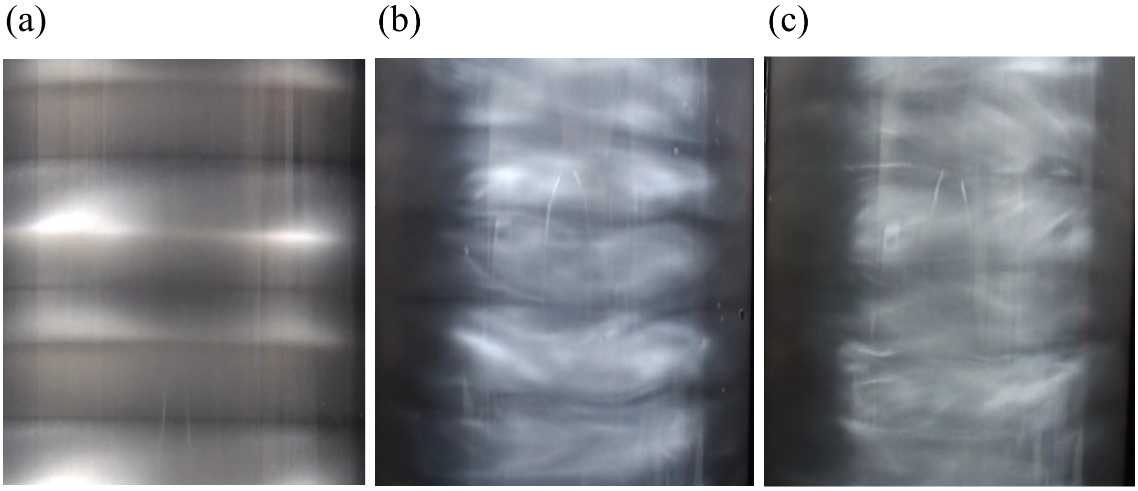

Fig. 1−5 Taylor−Couette flow
at (a) Re = 212(laminar Taylor vortex flow), (b) Re = 994 (wavy vortex flow),
and (c) Re = 3862 (weakly turbulent wavy vortex flow)

As shown in **Fig. 1−5**, Taylor−Couette flow shows the transition sequence from Couette flow to turbulent vortex flow with an increase of Re. The fluid flow was visualized using a vertical Taylor−Couette flow reactor (TCFR) of $R_i/R_o = 0.66$ (R_i = 25.0 mm, R_o = 38.0 mm) and h = 300 mm, with 40 wt% glycerol solution seeded with Kalliroscope AQ-1000 flakes (Matisse and Gorman, 1984; Savaş, 1985). Since the toroidal motion of fluid elements causes highly effective radial mixing and heat/mass transfer within each vortex cell, each cell can be regarded as a well-mixed batch vessel. (Kataoka, 1975; Kataoka *et al*., 1977). Additionally, all the fluid elements leaving the annulus have the same residence time when a relatively small axial flow is added (Kataoka *et al.*, 1975). Therefore, the reactor enables converting a batch operation to a continuous one. For these reasons, TCFR has been applied to various chemical processes and has successfully showed its superiority to the conventional stirred tank reactor (e.g. Kataoka *et al.*, 1995; Ogihara *et al.*, 1995; Sczechowski *et al.*, 1995; Giordano *et al.*, 2000; Lee and Lueqtow, 2001; Dutta and Ray, 2004; Orlowska *et al.*, 2014). Most applications, however, have been limited to simple fluid processes in which the interaction between molecules or phases can be neglected.

1. 3. PI of chemical processes with complex fluids

Interactions between molecules or phases significantly influence the fluid flow. There are a wide variety of industries dealing with fluids having such interactions that cannot be neglected, and these fluids are called “complex fluids”. For example, polymeric fluids consist of many polymer chains. Because of the interaction between polymer chains, many polymeric fluids show non-Newtonian behavior, especially a shear-thinning property: the viscosity decreases with increasing shear-rate. This non-Newtonian behavior causes several distinct flow phenomena, reviewed in many books and papers (Skelland, 1967; Elson *et al.*, 1986; Bird *et al.*, 1987; Larson, 1988; Galindo and Nienow, 1992; Amanullah *et al.*, 1998; Larson, 1998; Ascanio *et al.*, 2004; Fontaine *et al.*, 2013). Moreover, multiphase flow appears frequently in chemical processes, e.g. bubble columns, packed columns and bioreactors, and phase interactions extremely complicate the flow field in the reactor (e.g. Landeghem, 1980; Abubakar *et al.*, 2014; Wang *et al.*, 2014).

In this study, representative examples of complex fluid processes were selected: the non-Newtonian fluid process that is strongly affected by the molecule interaction; and the gas–liquid two-phase flow process that is strongly affected by the phase interaction.

In the non-Newtonian fluid process, one of the most serious problems is the viscosity distribution in connection with the distribution of velocity gradient in the reactor. Because this viscosity distribution causes the formation of poor fluidity region, the viscosity distribution, i.e. the shear-rate distribution, should be suppressed. Furthermore, in many non-Newtonian fluid processes, the fluid viscosity intricately changes during a reaction. Because of this, optimization of the impeller is difficult if a stirred tank reactor is used. Further, there is a basic bottleneck for the reactor design of non-Newtonian fluid processes.

Fluid flows are governed by the Navier–Stokes equations. When the Navier–Stokes equations are expressed in a non-dimensional form, two non-dimensional parameters, *Re* and *Fr* (Froude number), appear in the forms of 1/*Re* and 1/*Fr*, as shown in Eq. (1–2).

$$\frac{\partial \boldsymbol{u}^*}{\partial t} + \left(\boldsymbol{u}^* \cdot \nabla^*\right)\boldsymbol{u}^* = -\nabla^* p^* + \frac{1}{Re}\nabla^* \cdot \left[\left(\nabla^* \boldsymbol{u}^* + \nabla^* \boldsymbol{u}^{*T}\right)\right] + \frac{1}{Fr}\boldsymbol{g}^* \qquad (1\text{–}2)$$

where $\boldsymbol{u}$ is the velocity, t is the time, p is the pressure, ρ is the density, μ is the viscosity, and $\boldsymbol{g}$ is the gravitational acceleration. The asterisk symbol denotes the non-dimensional form. For a forced convection, Eq. (1–2) shows that *Re* is the only flow parameter because $Fr \approx \infty$. Therefore, fluid flows and reactor design are controlled based on *Re*. Theoretically speaking, the scale up or down for a Newtonian fluid process can be conducted by keeping $V \times L$ constant. However, in a non-Newtonian fluid process, because the viscosity spatially changes in connection with the distribution of velocity gradient (V/L) in the reactor, the definition of Re becomes complicated. Keeping both $V \times L$ and V/L constant is nearly impossible. Thus, because the scale up or down based on Re is impossible, another parameter which expresses the flow condition is necessary. As Ohta (2013) pointed out, the practical construction of effective Re, Re_{eff}, for the system based on the effective viscosity, η_{eff}, is required for design of non-Newtonian fluid process.

Meanwhile, gas–liquid two-phase flow is frequently encountered in the overall industrial processes, especially food processes or bio-processes. In such processes, the traditional stirred tank reactor is usually used. For process design and control, one of the most important parameters is the volumetric mass transfer coefficient. Many researchers have made an effort to construct a correlation between the volumetric mass transfer coefficient and the operation conditions in stirred tanks (Schlüter and Deckwer, 1992; Kapic and Heindel, 2006; Ungerman and Heindel, 2007; Labík *et al.*, 2014). Their results indicate that a higher rotational speed of impeller is necessary for keeping more bubbles in the tank. In addition, the higher rotation of impeller enhances the mass transfer. However, the high shear force caused by the high rotation of impeller damages enzymes or microorganisms in food processes and bioprocesses (e.g. Ganesh *et al.*, 2000; Gunjikar *et al.*, 2001). On the other hand, the sufficient mass transfer under low rotational speed cannot be conducted. This trade–off relation is the bottleneck. A mild but effective mixing is required for these processes.

TCFR is suitable for PI of these processes with complex fluids, for non-Newtonian fluid process and for gas–liquid two-phase flow processes. Because TCFR has a narrow gap, the shear-rate distribution can be suppressed compared with the traditional stirred tank reactor. Further, it has a mild but effective mixing performance compared with the traditional stirred tank reactor. From the viewpoint of strategies of reactor design toward PI, TCFR is a satisfactory reactor. For these reasons, the potential of PI with complex fluids was investigated in this study.

1. 4. Construction of this thesis

Based on the above sections, the construction of this thesis is as shown in the schematic chart **Fig. 1–6**.

In Chapter 1, the general introductions about PI, Taylor–Couette flow and complex fluids were described.

In Chapter 2, the construction of Re_{eff} for Taylor–Couette flow with non-Newtonian fluids was attempted. How to estimate η_{eff} is the key to defining Re_{eff}. First, the viscosity distribution was clarified by numerical simulation. Subsequently, based on the effective viscosity estimated from the distribution, Re_{eff} was defined.

In Chapter 3, the TCFR was applied to a starch hydrolysis process as a typical example of non-Newtonian fluid process. Starch hydrolysis is a process for the production of reducing sugar from starch suspension, and is conducted under a batch operation. In this chapter, the starch hydrolysis process was converted from the batch to the continuous operation using the TCFR. The key operation of this process is mixing of gelatinized starch with enzymes. The effect of flow condition on the sugar yield was investigated based on the Re_{eff} defined in Chapter 2.

In Chapter 4, the gas–liquid two-phase Taylor–Couette flow was investigated. In order to overcome its bottleneck, it is necessary to enhance the centrifugal force and to stabilize the vortex structure even at a relatively lower rotational speed of inner cylinder. Therefore, in this chapter, a novel TCFR with a ribbed inner cylinder was emplyed. Further, the effect of the novel TCFR on mass transfer between gas and liquid was investigated.

In Chapter 5, the studies in Chapter 2–4 were concluded. Additionally, future work toward PI of complex fluids was described.

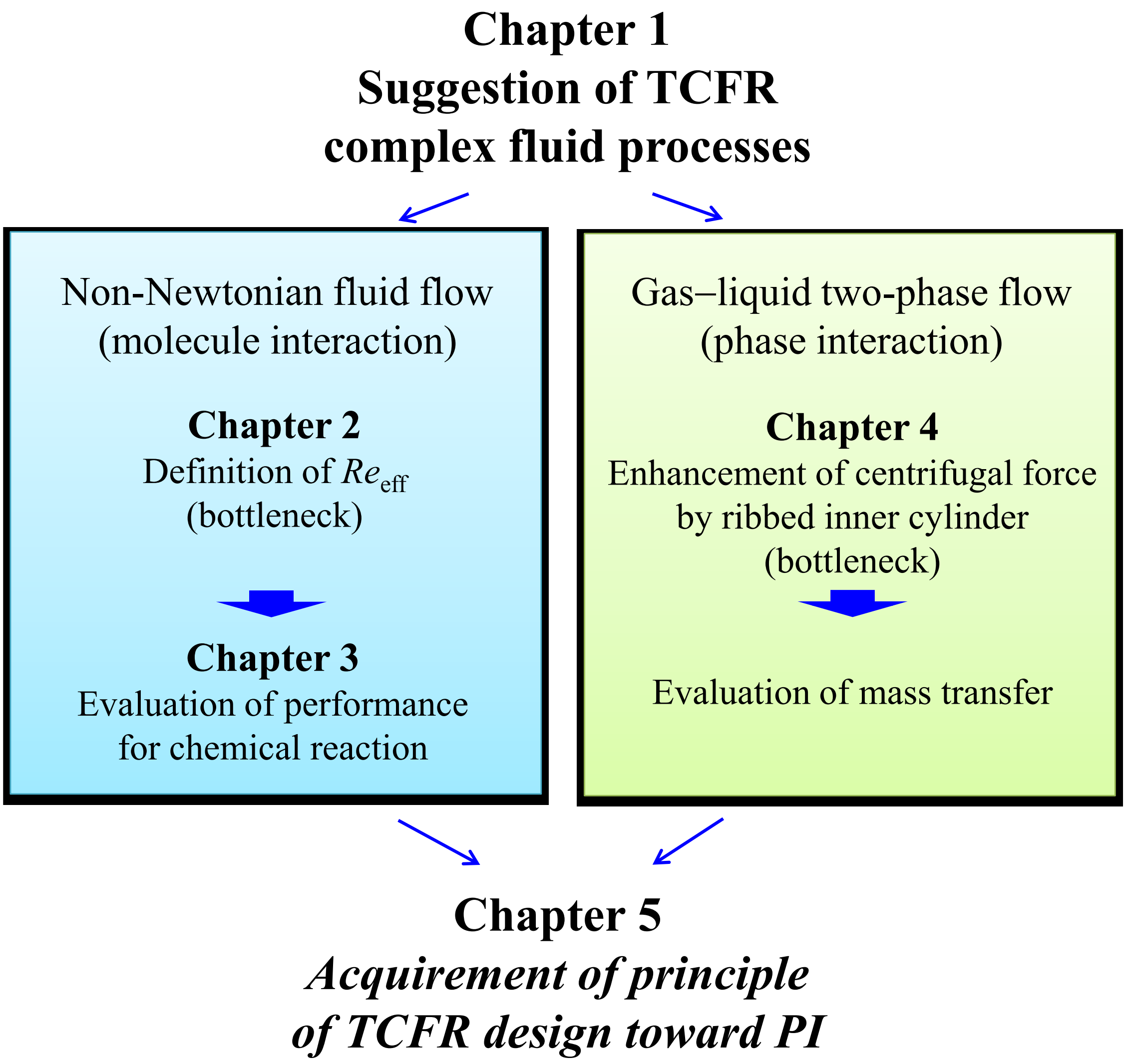

Fig. 1–6 Schematic chart of this thesis

Nomenclature

d : gap width, m

D : representative length, m

Fr : Froude number (= V^2/Dg), -

g : gravity acceleration (= 9.8 $\mathrm{m/s^2}$), $\mathrm{m/s^2}$

h : height of apparatus, m

L : representative length, m

p : pressure, Pa

Re : Reynolds number (= $\rho R_\mathrm{i}\omega d/\eta$), -

Re_cr : critical Reynolds number, -

Re_eff : effective Reynolds number (= $\rho R_\mathrm{i}\omega d/\eta_\mathrm{eff}$), -

R_i : inner cylinder radius, m

R_o : outer cylinder radius, m

t : time, s

$\boldsymbol{u}$: velocity, m/s

V : representative velocity, m/s

Greek letters

η : fluid viscosity, Pa·s

η_{eff} : effective viscosity, Pa·s

ρ : fluid density, kg/m^3

ω : angular velocity of inner cylinder, rad/s

References

M. S. R. Abbott, G. V. Rerez, A. P. Harvey, M. K. Theodorou, Reduced power consumption compared to a traditional stirred tank reactor (STR) for enzymatic saccharification of alpha-cellulose using oscillatory baffled reactor (OBR) technology, *Chem. Eng. Res. Des.*, **92**, 1969–1975 (2014)

A. Abubakar, T. Al-Wahaibi, Y. Al-Wahaibi, A. R. Al-Hashmi, A. Al-Ajmi, Roles of drag reducing polymers in single- and multi-phase flowas, *Chem. Eng. Res. Des.*, **92**, 2153–2181

A. Amanullah, S. A. Hjorth, A. W. Nienow, A new mathematical model to predict cavern diameters in highly shear thinning, power law liquids using axial flow impellers, *Chem. Eng. Sci.*, **53**, 455–469 (1998)

C. D. Andereck, S. S. Liu, H. L. Swinney, Flow regimes in a circular Couette system with independently rotating cylinders, *J. Fluid Mech.*, **164**, 155−183 (1986)

G. Ascanio, S. Foucault, P. A. Tanguy, Time-periodic mixing of shear-thinning fluids, *Chem. Eng. Res. Des.*, **82**, 1199−1203 (2004)

R. B. Bird, R. C. Armstrong, O. Hassager, Dynamics of polymeric liquids, Fluid mechanics (Volume 1), John Wiley & Sons, Inc., U.S.A. (1987)

K. Boodhoo, A. Harvey, Process intensification for Green chemistry, John Wiley & Sons, Inc., U. K. (2013)

D. Coles, Transition in circular Couette flow, *J. Fluid Mech.*, **21**, 385–425 (1965)

S. J. Curran, R. A. Black, Quantitative experimental study of shear stresses and mixing in progressive flow regimes within annular-flow bioreactor, *Chem. Eng. Sci.*, **59**, 5859−5868 (2004)

A. Davey, The growth of Taylor vortices in flow between rotating cylinders, *J. Fluid Mech.*, **14**, 336–368 (1962)

P. K. Dutta, A. K. Ray, Experimental investigation of Taylor vortex photocatalytic reactor for water purification, *Chem. Eng. Sci.*, **59**, 5249−5259 (2004)

P. T. Elson, D. J. Cheesman, A. W. Nienow, X-ray studies of cavern sizes and mixing performance with fluid possessing a yield stress, *Chem. Eng. Sci.*, **41**, 2555–2562 (1986)

A. Fontaine, Y. Guntzburger, F. Bertrand, L. Fradette, M. C. Heuzey, Experimental investigation of the flow dynamics of rheologically complex fluids in a Maxblend impeller system using PIV, *Chem. Eng. Res. Des.*, **91**, 7−17 (2013)

E. Galindo, A. W. Nienow, Mixing of highly viscous simulated Xanthan fermentation broths with the Lightnin A315 impeller, *Biotechnol. Prog.*, **8**, 233–239 (1992)

K. Ganesh, J. B. Joshi, S. B. Sawant, Cellulase deactivation in a stirred reactor, *Biochem. Eng. J.*, **4**, 137−141 (2000)

X. Gao, B. Kong, R. D. Vigil, CFD investigation of bubble effects on Taylor-Couette flow patterns in the weakly turbulent vortex regime, *Chem. Eng. J.*, **270**, 508−518 (2015)

R. L. C. Giordano, R. C. Giordano, C. L. Cooney, Performance of a continuous Taylor−Couette−Poiseuille vortex flow enzymic reactor with suspended particles, *Process Biochem.*, **35**, 1093−1101 (2000)

T. P. Gunjikar, S. B. Sawant, J. B. Joshi, Shear deactivation of cellulase, exoglucanase, endoglucanase, and *β*-glucosidase in a mechanically agitated reactor, *Biotechnol. Prog.*, **17**, 1166−1168 (2001)

B. Haut, H. B. Amor, L. Coulon, A. Jacquet, V. Halloin, Hydrodynamics and mass transfer in a Couette-Taylor bioreactor for the culture of animal cells, *Chem. Eng. Sci.*, **58**, 777−784 (2003)

N. Jongen, M. Donnet, P. Bowen, J. Lemaître, H. Hofmann, R. Schenk, C. Hofmann, M. Aoun-Habbache, S. Guillemet-Fritsch, J. Sarrias, A. Rousset, M. Viviani, M. T. Buscaglia, V. Buscaglia, P. Nanni, A. Testino, J. R. Herguijuela, Development of a continuous segmented flow tubular reactor and the "Scale-out" Concept – In search of perfect powders, *Chem. Eng. Technol.*, **26**, 303–305 (2003)

A. Kapic, T. J. Heindel, Correlating gas-liquid mass transfer in a stirred-tank reactor, *Chem. Eng. Res. Des.*, **84**, 239−245 (2006)

K. Kataoka, Heat-transfer in a Taylor vortex flow, *J. Chem. Eng. Japan*, **8**, 271−276 (1975)

K. Kataoka, H. Doi, T. Hongo, M. Futagawa, Ideal plug-flow properties of Taylor vortex flow, J. *Chem. Eng. Japan*, **8**, 472−476 (1975)

K. Kataoka, H. Doi, T. Komai, Heat/mass transfer in Taylor vortex flow with constant axial flow rates, *Int. J. Heat Mass Transfer*, **20**, 57−63 (1977)

K. Kataoka, Taylor vortices and instabilities in circular Couette flows, in *Encyclopedia of Fluid Mechanics*, vol. 1, ed. by N. P. Cheremisinoff, pp. 236−274, Gulf Publications, Houston, U.S.A. (1986)

K. Kataoka, N. Ohmura, M. Kouzu, Y. Simamura, M. Okubo, Emulsion polymerization of styrene in a continuous Taylor vorex flow reactor, *Chem. Eng. Sci.*, **50**, 1409−1416 (1995)

L. Labík, R. Vostal, T. Moucha, F. Rejl, M. Kordač, Volumetric mass transfer coefficient in multiple-impeller gas-liquid contactors. Scaling-up study for various impeller types, *Chem. Eng. J.*, **240**, 55−61 (2014)

H. V. Landeghem, Multiphase reactors: mass transfer modeling, *Chem. Eng. Sci.*, **35**, 1912–1949

R. G. Larson, Constitutive Equations for Polymer Melts and Solutions: Butterworths Series in Chemical Engineering, Butterworth-Heinemann, U.S.A. (1988)

R. G. Larson, The Structure and Rheology of Complex Fluids, Oxford University Press, U.S.A. (1998)

S. Lee, R. M. Lueqtow, Rotating reverse osmosis: a dynamic model for flux and rejection, *J. Memb. Sci.*, **192**, 129–143 (2001)

O. Levenspiel, Chemical reaction engineering 3rd edition, John Wiley & Sons, Inc., U.S.A. (1999)

P. Matisse, M. Gorman, Neutrally buoyant anisotropic particles for flow visualization, *Phys. Fluids*, **27**, 759–760 (1984)

X. Ni, S. Gao, R. H. Cumming, D. W. Pritchard, A comparative study of mass transfer in yeast for batch pulsed baffled bioreactor and a stirred tank fermenter, *Chem. Eng. Sci.*, **50**, 2127–2136 (1995)

X. Ni, S. Gao, Scale-up correlation for mass transfer coefficients in pulsed baffled reactors, *The Chem. Eng. J.*, **63**, 157–166 (1996)

T. Ogihara, G. Matsuda, T. Yanagawa, N. Ogata, K. Fujita, M. Nomura, Continuous synthesis of monodispersed silica particles using Couette–Taylor vortex flow, *J. Ceram. Soc. Japan*, **103**, 151–154 (1995)

M. Ohta, Process intensification of non-Newtonian fluid system, SCEJ 45th Autumn Meeting, XE113 (2013)

M. Orlowska, T. Koutchma, M. Kostrzynska, J. Tang, C. Defelice, Evaluation of mixing flow conditions to inactivate Escherichia coli in opaque liquids using pilot–scale

Taylor–Couette UV unit, *J. Food. Eng*,. **120**, 100–109 (2014)

N. Patel, V. Choy, T. White, G. Munkvold, J. Thibault, Design of a novel Couette flow bioreactor to study the growth of fungal microorganism, *J. Biotechnol.*, **145**, 264–272 (2010)

C. Ramshaw, “Higee” Distillation – An example of process intensification, *Chem. Eng.*, **389**, 13–14 (1983)

D. Reay, C. Ramshaw, A. Harvey, Process intensification, Butterworth-Heinemann, Oxford, UK (2008)

Ö. Savaş, On flow visualization using reflective flakes, *J. Fluid Mech.*, **152**, 235–248 (1985)

V. Schlüter, W. D. Deckwer, Gas/liquid mass transfer in stirred vessels, *Chem. Eng. Sci.*, **47**, 2357–2362 (1992)

J. G. Sczechowski, C. A. Koval, R. D. Noble, A Taylor vortex reactor for heterogeneous photocatalysis, *Chem. Eng. Sci.*, **50**, 3163–3173 (1995)

A. H. P. Skelland, Non-Newtonian flow and heat transfer, John Wiley & Sons, U.S.A. (1966)

A. I. Stankiewicz, J. A. Moulijn, Process intensification: Transforming chemical engineering, *Chem. Eng. Prog.*, **96**, 22–34 (2000)

A. I. Stankiewicz, Serving the triple bottom line: Process intensification role in sustainable manufacturing, *Kagaku kougaku*, **69**, 148–151 (2005)

P. Stonestreet, A. P. Harvey, A mixing-based design methodology for continuous oscillatory flow reactors, *Chem. Eng. Res. Des.*, **80**, 31–44 (2002)

J. T. Stuart, Taylor-vortex flow: A dynamical system, *SIAM Rev.*, **28**, 315–342 (1986)

G. I. Taylor, Stability of a viscous liquid contained between two rotating cylinders, *Phil.*

Trans. Roy. Soc. A, **223**, 289–343 (1923)

A. J. Ungerman, T. J. Heindel, Carbon monoxide mass transfer for syngas fermentation in a stirred tank reactor with dual impeller configurations, *Biotechnol. Prog*., **23**, 613–620 (2007)

S. Wang, G. Metcalfe, R. L. Stewart, J. Wu, N. Ohmura, X. Feng, C. Yang, Solid–liquid separation by particle-flow –instability, *Energy Environ. Sci*., **7**, 3982–3988 (2014)

2. Effective Reynolds number for Taylor–Couette flow with non-Newtonian fluids

2. 1. Introduction

In non-Newtonian fluid processes (e.g. food processing, polymerization process and bioprocesses etc.), the viscosity spatially changes in connection with the distribution of the velocity gradient in the reactor. This viscosity distribution causes serious problems. For example, in a traditional stirred tank, a cavern around the impeller is formed with strong shear-thinning fluid which is the most popular fluid among non-Newtonian fluids, and there are many dead zones in the continuous stirred tank reactor (Saeed and Ein-Mozaffari, 2008; Patel *et al*., 2011). Therefore, Niederkorn and Ottino (1994) state that the current practice of designing industrial mixers for non-Newtonian fluids is more art than science. On the other hand, a TCFR mixes the fluid in the narrow gap, which can suppress the distribution of velocity gradient and consequently reduce the viscosity distribution. Therefore, the TCFR is especially advantageous in application to non-Newtonian fluid processes. In fact, Hubacz and Buczyńska (2011) and Hubacz *et al*. (2013) applied the TCFR to starch gelatinization selected as a typical example of a shear-thinning fluid process. These studies reported that the enhanced heat transfer and mixing due to Taylor vortices improved starch gelatinization. However, it has been difficult to predict a transition point from circular Couette flow at which Taylor vortices first appear. Numerical simulation using rheological properties of the effluent is the only way to prove whether Taylor vortices generate or not.

From the viewpoint of practical applications, the definition of an effective Reynolds number (Re_{eff}) for the non-Newtonian fluid system is crucially important. The reason for the difficulty in predicting the critical condition has its roots in the insufficiency of definition of *Re* for the non-Newtonian fluid system, especially shear-thinning fluid system (Alibenyahia *et al.*, 2012). In other words, how to appropriately define the effective viscosity, η_{eff}, is the key to defining Re_{eff}. In order to determine the effective viscosity, the viscosity distribution in a TCFR should be clarified. Computational fluid dynamics (CFD) can be a powerful tool for investigating not only the flow condition but also the viscosity distribution in the reactor. Sinevic *et al.* (1986) first determined the onset of Taylor vortices for shear-thinning fluids by measuring the torque exerted by the fluid on the rotating inner cylinder. The Re_{cr} varied with the strength of shear-thinning properties, and they could not find any correlation between Re_{cr} and shear-thinning properties. Jastrzębski *et al.* (1992) determined the critical Taylor number, Ta_{cr}, from a linear stability analysis. Ta has the same physical meaning as Re. They concluded that the shear-thinning property had a destabilizing effect. Lockett *et al.* (1992) defined Ta_{cr} using 2D numerical simulation and found that the stabilizing or destabilizing effect induced by the shear-thinning property depends on the radius ratio. Coronado-Matutti *et al.* (2004) investigated the onset of instability by using 2D numerical simulation. They concluded that if Ta was defined based on the viscosity at $\dot{\gamma} = R_{\mathrm{i}}\omega / d$, the Ta_{cr} calculated for Newtonian fluid could be diverted for an estimation of the onset of instability for shear-thinning fluids. Nevertheless, the rheological parameters used in their study were such that the viscosity profile hardly departed from that of a Newtonian fluid. For the shear-thinning fluid system, it can be summarized that there is no practical basis because of the variability of Re_{cr}.

In this chapter, focusing on shear-thinning fluids, the definition of Re_{cr} was discussed. Furthermore, in order to estimate the approximate Re_{eff} from rheological properties and the operational condition, the construction of a correlation equation between the rotational speed of the inner cylinder and the effective shear-rate, $\dot{\gamma}_{\mathrm{eff}}$, resulting to η_{eff} was attempted. The Re_{eff} calculated by the correlation equation allows to judgment of whether Taylor vortices are generated or not without numerical simulation. Finally, the critical condition predicted by the correlation equation was validated through the experiment of flow visualization.

2. 2. Numerical simulation and experiment

2. 2. 1. Governing equations

The fluid was considered as an incompressible shear-thinning fluid. In a three-dimensional calculation, the governing equations of the shear-thinning fluid flow are the conservation equations of mass and momentum given by

$$\nabla \cdot \boldsymbol{u} = 0 \tag{2–1}$$

$$\frac{\partial \boldsymbol{u}}{\partial t} + (\boldsymbol{u} \cdot \nabla)\boldsymbol{u} = -\frac{\nabla p}{\rho} + \frac{1}{\rho}\nabla \cdot (2\eta \boldsymbol{D}) + \boldsymbol{g} \tag{2–2}$$

where $\boldsymbol{u}$ is the velocity, t is the time, p is the pressure, ρ is the density, η is the viscosity depending on the shear-rate, $\boldsymbol{D}$ (= $(\nabla\boldsymbol{u} + \nabla\boldsymbol{u}^{\mathrm{T}}) / 2$) is the rate of deformation tensor, and $\boldsymbol{g}$ is the gravitational acceleration. In this simulation, the steady state was assumed.

For most of all practical shear-thinning fluids, viscosity against shear-rate curves exhibit two Newtonian plateaus in low and high shear-rate regions and the power-law property in the transition region. As the Carreau model (1972) takes these features into account, the model is the most flexible in comparison to other rheological models, such as the power-law model. Furthermore, contrary to the power-law model that predicts an infinite viscosity at the limit of zero shear-rate, the Carreau model leads to a smooth transition to a constant viscosity at the limit of zero shear-rate. This smooth transition is useful for numerical simulation. This study, therefore, adopted Carreau model to express the shear-thinning property:

$$\eta = (\eta_0 - \eta_\infty)\left[1 + (\beta \cdot \dot{\gamma})^2\right]^{(n-1)/2} + \eta_\infty \qquad (2\text{–}3)$$

where $\dot{\gamma}$ is the shear-rate, η_0 is the zero shear-rate viscosity, η_∞ is the infinite shear-rate viscosity, β is the characteristic time and n is the power index. Here, the shear-rate is defined as $\dot{\gamma} = \sqrt{2\boldsymbol{D}:\boldsymbol{D}}$, which is the magnitude of the rate of deformation tensor. When the square root is taken, the sign must be so chosen that $\dot{\gamma}$ is a positive quantity. η_0 is usually much larger than η_∞ for shear-thinning fluids and it follows that the value of η_∞ could be ignored in this simulation (Bird *et al.*, 1987). A simplified Carreau model that is used in the numerical algorithm is given by Eq. (2–4):

$$\eta = \eta_0\left[1 + (\beta \cdot \dot{\gamma})^2\right]^{(n-1)/2} \qquad (2\text{–}4)$$

The value of η_0 strongly depends on the kind of fluids, e.g. η_0 = 86.5 Pa·s for 1wt% carboxymethyl cellulose solution with 60wt% glucose (Fontaine *et al.*, 2013), η_0 = 0.78 Pa·s for milk (Matsumoto *et al.*, 2015), η_0 = 0.56 Pa·s for blood (Cho *et al.*, 1991) and

η_0 = 0.022 Pa·s for 0.02wt% polyacrylamide solution (Poole *et al.*, 2004). From the viewpoint of process design using the TCFR, an extremely high viscous fluid such as a polymer melt is undesirable because an unrealistic rotational speed of the inner cylinder is required to generate Taylor vortices. For example, the critical rotational speed of the inner cylinder, ω_{cr}, is 13,120 rad/s for R_{i} = 0.0125 m and R_{o} = 0.0175 m if the fluid viscosity is 10 Pa·s. Practically, a maximum ω is about 100 rad/s with a standard motor. Thus, the value of η_0 was fixed at 0.2 Pa·s as a moderate viscosity. n and β indicate the slope of decreasing viscosity with the shear-rate and the inverse of the shear-rate where the viscosity begins to decrease, respectively. Both values of n and β are much influenced depending on the fluids in the practical applications (Yasuda *et al.*, 1981). Yap *et al.* (1979) and Escudier *et al.* (2005) summarized the Carreau model parameters for various shear-thinning fluids. For many shear-thinning fluids, the value of n is usually 0.3–0.7, which is the same range as used in this chapter. However, the value of β is widespread, from 0.01 to 100. If the value of β is too small, the shear-thinning property may not appear. Therefore, in this simulation, 2, 10 and 50 s were selected for β. The rheological properties of each fluid are summarized in **Fig. 2–1**.

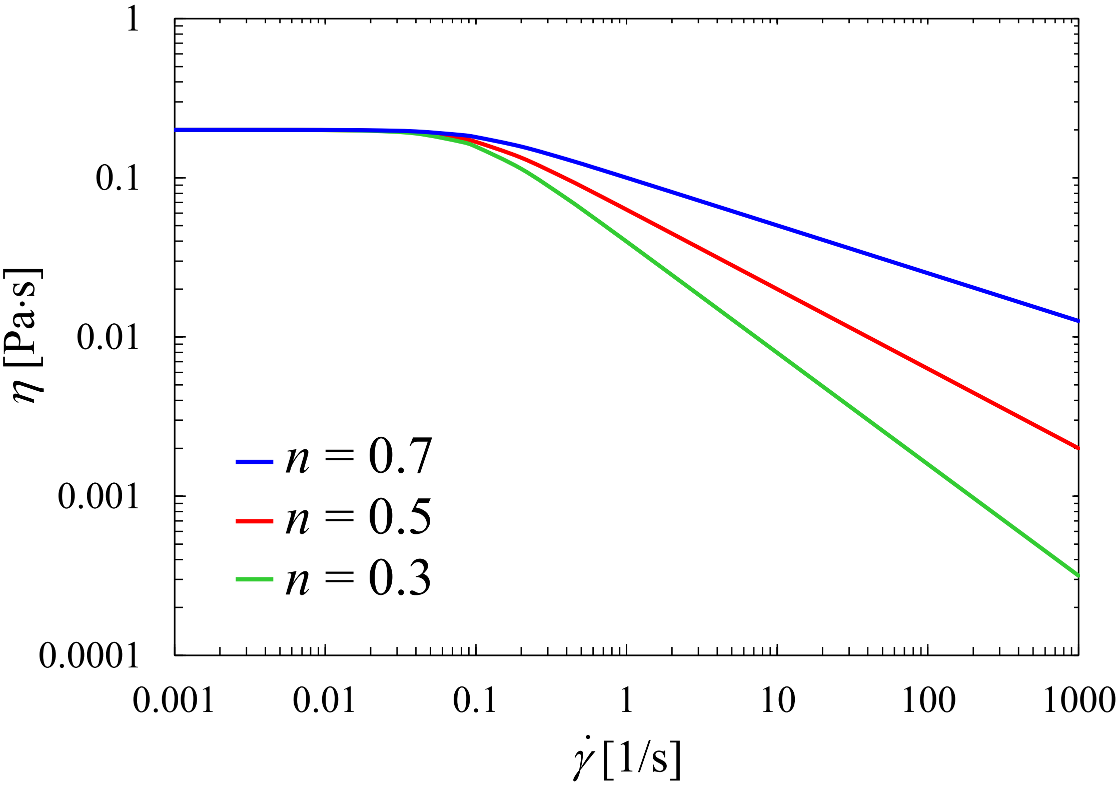

Fig. 2−1 Rheological properties of shear-thinning fluids ($\beta = 10$ s)

2. 2. 2. Computational system

A computational domain for the TCFR is shown in **Fig. 2–2**. The TCFR consisted of concentric cylinders (length: L = 150 mm), a rotating inner cylinder (outer radius: R_i = 9.5–15.5 mm) and a fixed outer cylinder (inner radius: R_o = 17.5 mm). In other words, the radius ratio ($R_\mathrm{i}/R_\mathrm{o}$) varied from 0.54 to 0.89 and the gap width, d, varied from 2.0 to 8.0 mm. The origin of the coordinates was set at the center of the left wall of the inner cylinder as shown in **Fig. 2–2**.

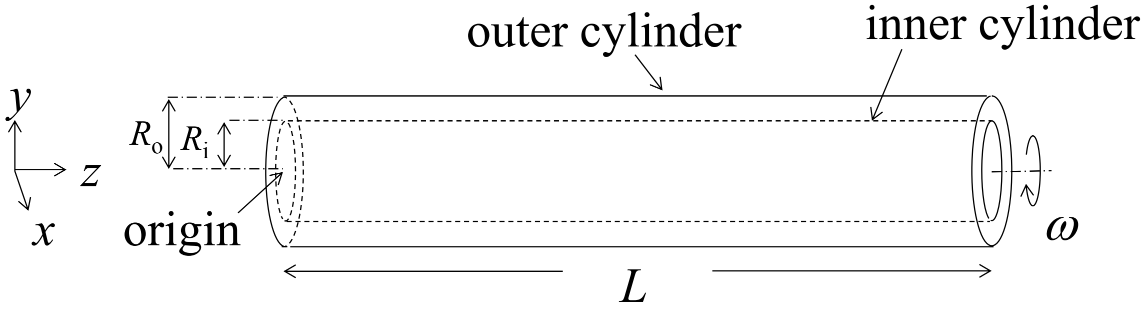

Fig. 2–2 Computational domain of the TCFR

OpenFOAM® 2.3.0 code, an open-source CFD code, was employed for the calculation. Because Cartesian coordinates are normally used in this software, a non-uniform grid is generated due to the calculation of annular flows such as Taylor–Couette flow. For Taylor–Couette flow, non-uniform grids in Cartesian coordinates can give sufficient results with a high calculation precision if the grid configuration, including the number of grids, is appropriately chosen (Nemri *et al.*, 2013; Poncet *et al.*, 2013). Thus, the number of non-orthogonal structured grids was 1,310,720 (32 × 64 × 640 in radial, azimuthal and axial directions, respectively), in this study. Unequally spaced grids were selected because finer resolution near the cylinder was necessary due to the steep velocity gradient (Hwang and Yang, 2004). The dependency of the number of cells on the results will be discussed later.

With respect to the boundary conditions of velocity, the circumferential velocity at the surface of the inner cylinder was set to $R_\mathrm{i} \times \omega$ and the other walls were assumed to be fixed (velocity is 0). For the boundary condition of pressure, the gradient was zero at all walls. The governing equations were discretized based on a finite volume method, and the second-order central difference scheme was applied to a convection and viscous term. The SIMPLE scheme was used for pressure–velocity coupling.

2. 2. 3. Flow visualization

The fluid flow was visualized using the horizontal TCFR of $R_\mathrm{i}/R_\mathrm{o} = 0.71$ ($R_\mathrm{i} = 12.5$ mm, $R_\mathrm{o} = 17.5$ mm) and $L = 150$ mm, as shown in **Fig. 2–3**. In order to maintain the temperature of the fluid, water at 25°C was passed through the jacket. The 3 wt% carboxymethyl cellulose (CMC; MP Biomedicals, LLC) and 0.1 wt% xanthan gum (XG; Sansho Co., Ltd.) solution were selected as model fluids. The densities of solution are 1011.6 kg/m^3 for CMC and 1000.4 kg/m^3 for XG. The flow pattern was visualized using an aqueous solution seeded with Kalliroscope AQ-1000 flakes (2 wt%). These particles consist of small, light reflecting slabs that align themselves along streamlines. The viscosity was measured at 25°C using a rotational rheometer (HAAKE Viscotester 550, Thermo Fisher Scientific Inc.). The rheological properties of CMC and XG are shown in **Fig. 2–4.** Also, lines in the figure were drawn using the Carreau model with the parameters shown in **Table 2–1**.

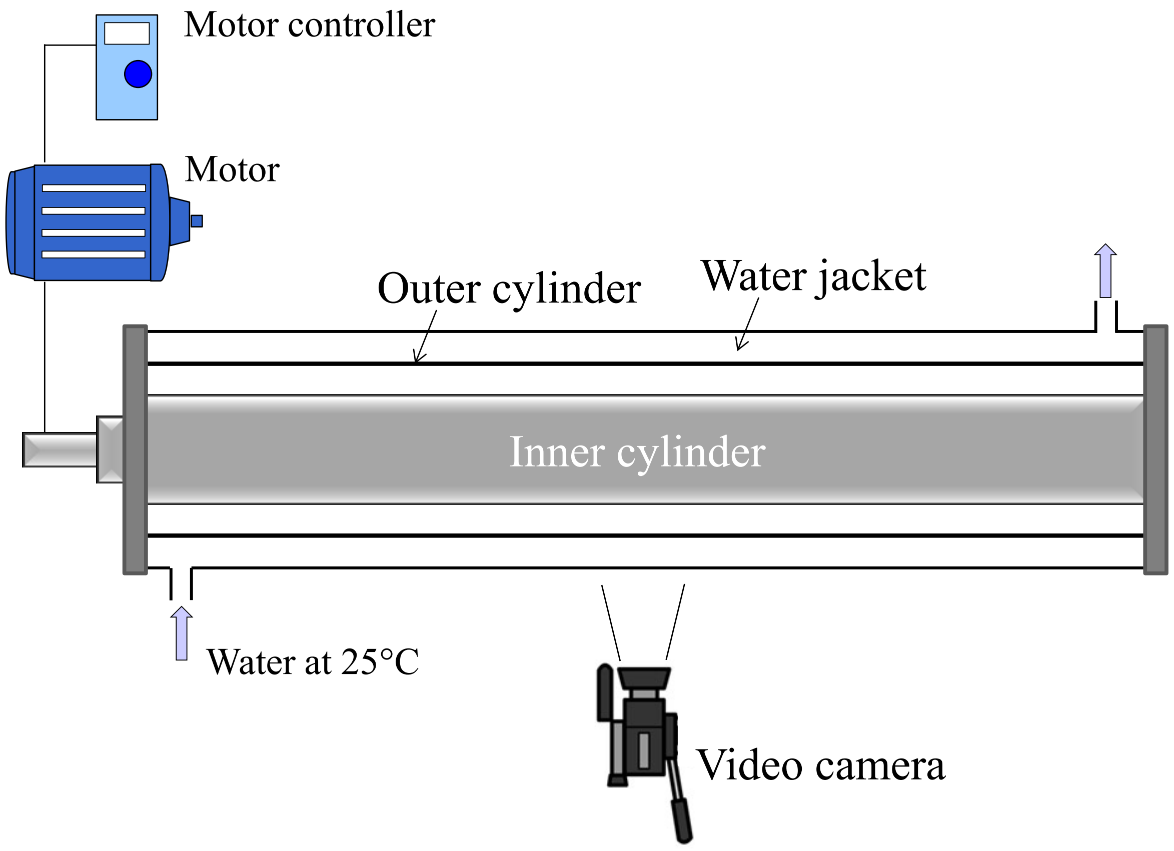

Fig. 2–3 Experimental set up for flow visualization

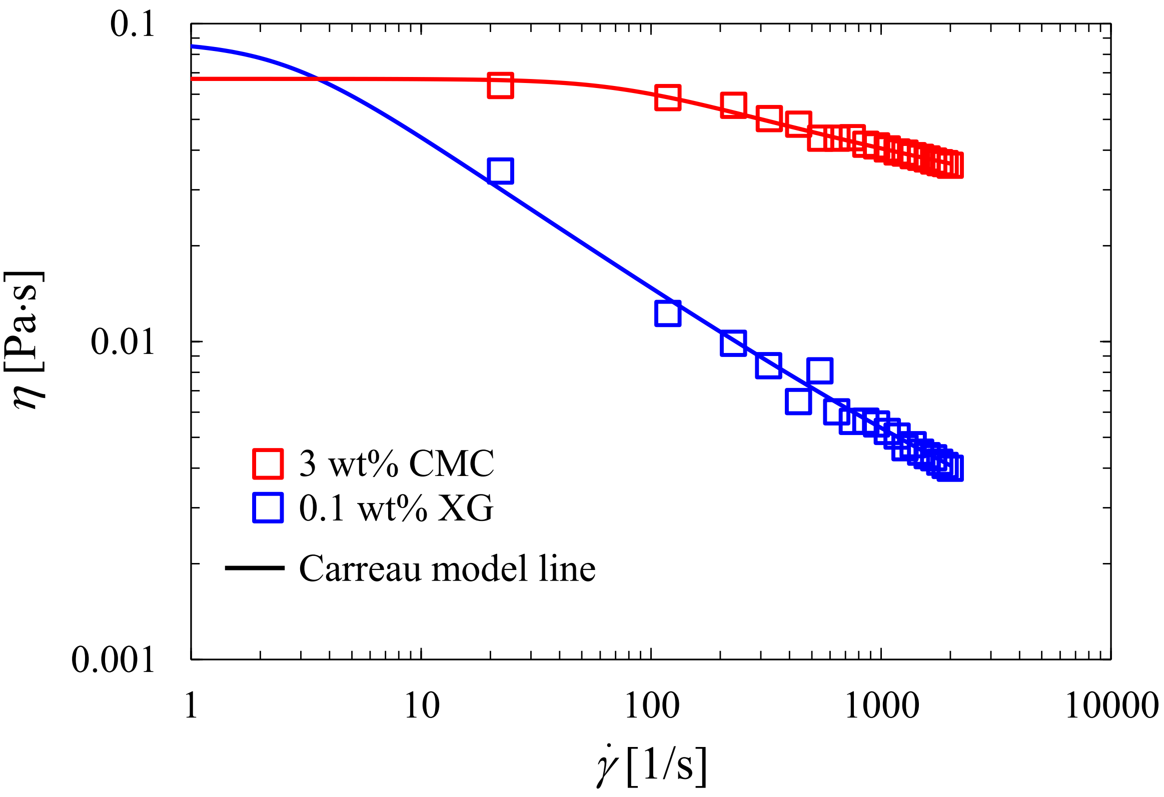

Fig. 2–4 Rheological properties for 3 wt% CMC and 0.1 wt% XG solutions

Table 2–1 Carreau model parameters for CMC and XG

	η_0 [Pa·s]	η_∞ [Pa·s]	n [–]	β [s]
3wt% CMC	0.067	0.018	0.7	0.013
0.1wt% XG	0.088	0.001	0.5	0.4

2. 3. Results and discussion

2. 3. 1. Validation of computational code

In the beginning, in order to validate the computational method, the experimental result by Makino *et al.* (2001) was reproduced. The geometry of the cylinder system (R_i = 37.5 mm, R_o = 50.0 mm, L = 45.0 mm) and conditions for the calculation were the same as their experimental conditions stated above. Note that this geometry was used only for validation of the computational code. In this calculation, Newtonian fluid was assumed and *Re* was set at 358.7. The radius ratio was 0.625, and the aspect ratio was 2. The mesh number was 16 × 64 × 32 in the radial, azimuthal and axial directions, respectively. Results of the present calculation and Makino's experiment are summarized in **Fig. 2–5**: (a) the velocity distribution on *y-z* plane, (b) the circumferential velocity (U_θ) and (c) the axial velocity (U_z). The numerical distribution of U_θ within a vortex at the center of gap along the axis was compared with the experimental one. Here, U_θ means the circumferential velocity ($U_\theta = (xU_y - yU_x)/(x^2+y^2)^{0.5}$) and z means the axial position. The calculation results of velocity distribution along inspected lines in **Fig. 2–5** (a) were compared with the experimental results. The slight deviation between the velocity obtained by numerical analysis and the experimental measurement near the inner and outer cylinder in **Fig. 2–5** (b) could be explained by the experimental error. In fact, such difference is observed in the reference (Makino *et al.*, 2001). As shown in **Fig. 2–5** (b) and (c), both numerical results for U_θ and U_z corresponded with the experimental results.

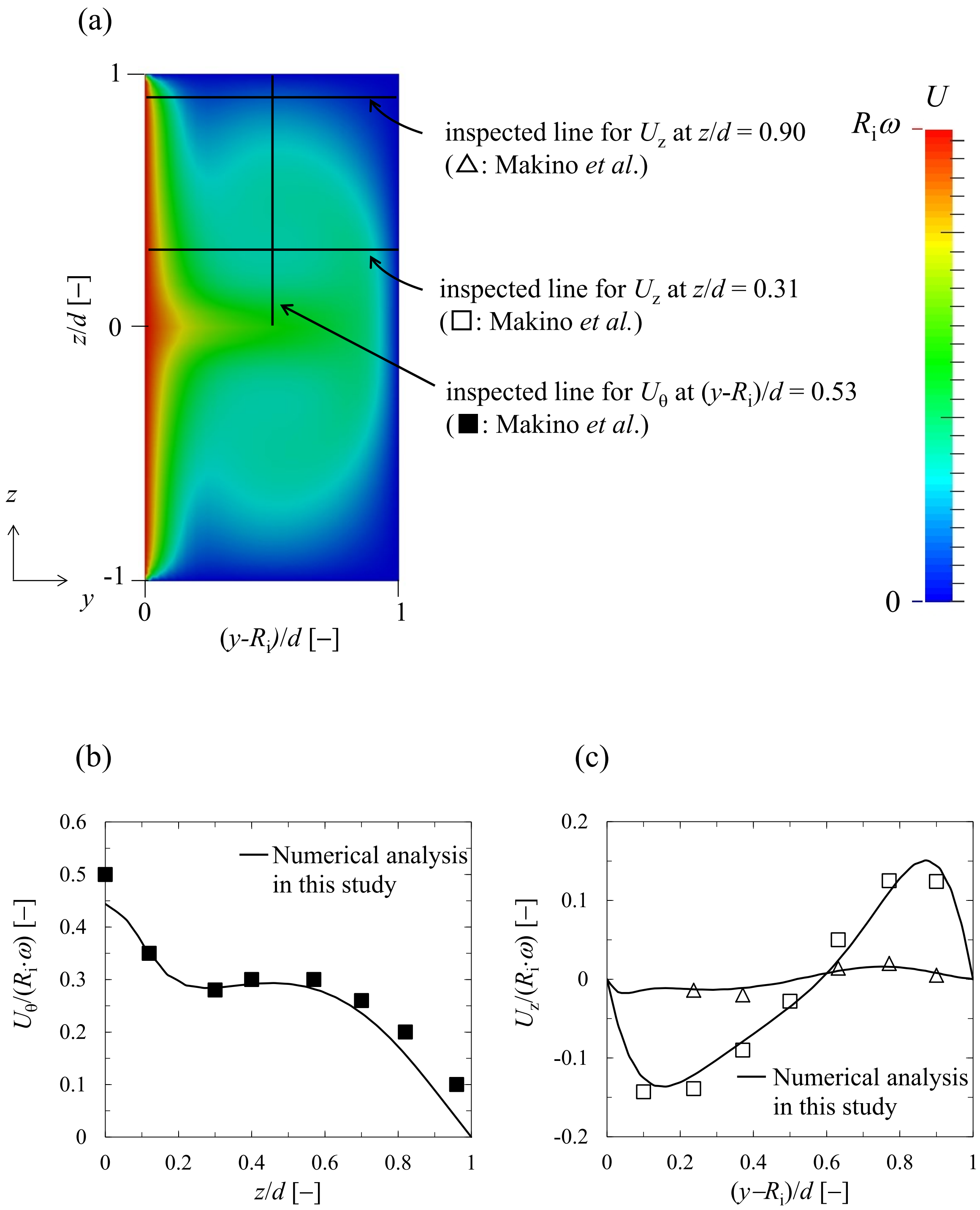

Fig. 2−5 Relationship between numerical and experimental velocity fields at $Re = 358.7$;
(a) velocity distribution, (b) circumferential velocity and (c) axial velocity

The dependency of the number of grids in the calculation result was investigated by varying the number of grids. Here, Newtonian fluid ($\eta = 0.002$ Pa·s) was assumed, and *Re* was set at 87.0. Here, $R_\mathrm{i}/R_\mathrm{o}$ was 0.71, and the aspect ratio was 30. The number of grids was 32 × 64 × 640 (system-1), 40 × 64 × 320 (system-2) or 32 × 80 × 640 (system-3) in radial, azimuthal and axial directions, respectively. For each system, the magnitude of velocity distribution at the center of the gap along the axis is shown in **Fig. 2–6**. Similarly, the distribution of shear stress at the inner cylinder surface along the axis is shown in **Fig. 2–7**. Here, the velocity and shear stress were normalized by $R_\mathrm{i}\omega$ and $d/\eta R_\mathrm{i}\omega$, respectively. In these two figures, no significant difference between the systems could be observed. Therefore, in this calculation, 32 × 64 × 640 meshes (system-1) was selected to save time on calculations. Further, it is necessary to keep cell Reynolds number (Re_cell) below 2 when the central difference scheme is applied to the convection term (Tanahashi, 1993):

$$Re_\mathrm{cell} = \frac{\rho U_i (\Delta V_i)^{1/3}}{\eta_i} \tag{2–5}$$

Here, U_i [m/s] is the local velocity magnitude, ΔV_i [m^3] is the cell volume and η_i [Pa·s] is the local viscosity. ΔV_i was defined as $\Delta x_i \times \Delta y_i \times \Delta z_i$. In all calculations, it was confirmed the Re_cell was below 2.

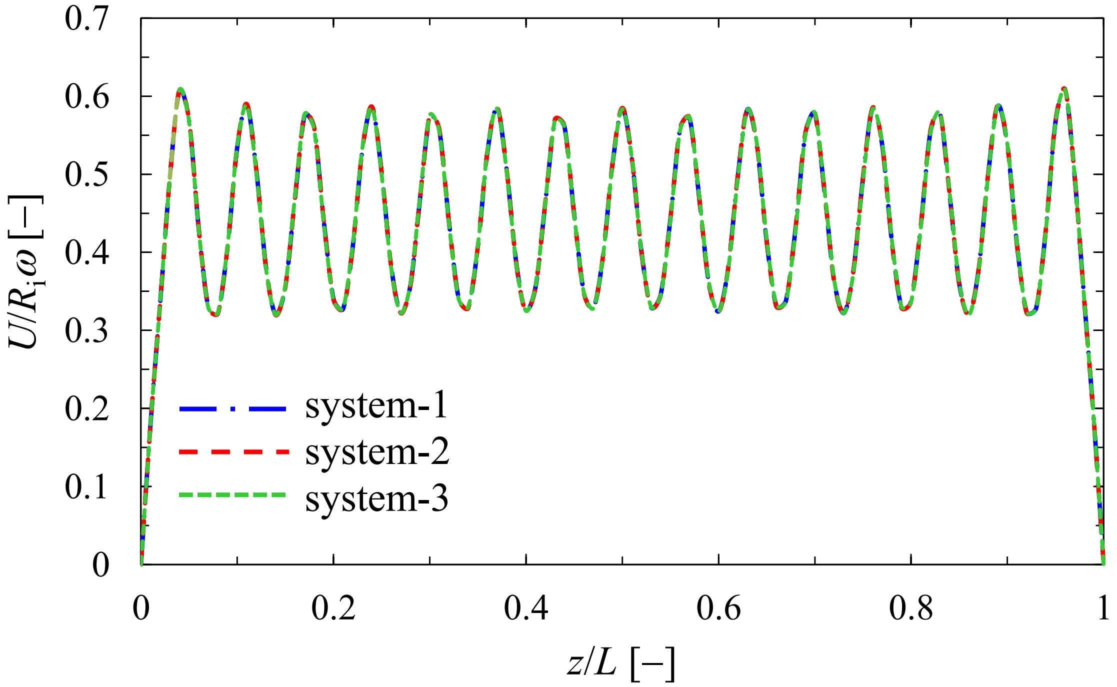

Fig. 2–6 Dependency of the number of grids
on the calculation results (velocity) at $Re = 87.0$

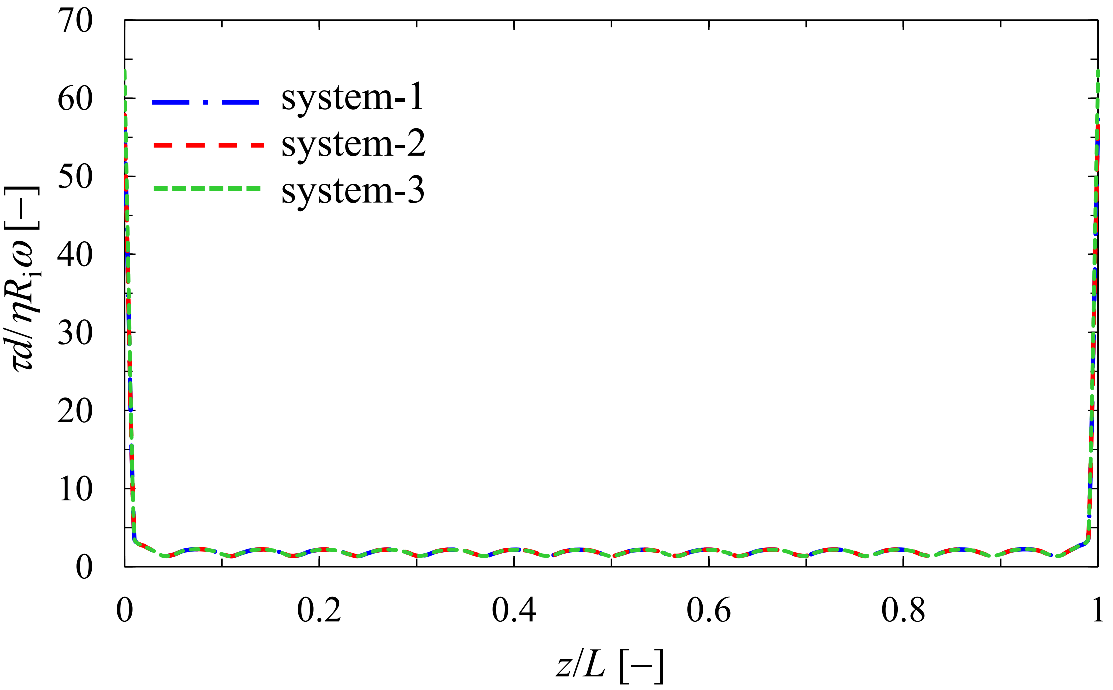

Fig. 2–7 Dependency of the number of the number of grids
on the calculation results (shear stress at the surface of inner cylinder) at *Re* = 87.0

2. 3. 2. Determination method of Re_{cr}

Escudier *et al.* (1995) suggested the method to experimentally determine Re_{cr} by focusing on the development of an axial velocity component at a certain location when the rotational speed of the inner cylinder was increasing. This method can be extended to the numerical determination of Re_{cr} (Coronado-Matutti *et al.*, 2004). This study focused on the growth of variation of the velocity magnitude along the axis. The magnitude of velocity periodically varies above Re_{cr} along the axis due to the toroidal motions of Taylor vortices. **Figure 2–8** shows the distribution of velocity at the middle of the gap along the axis for Newtonian fluid at Re = 80.0 and 82.2 in the case where R_i/R_o = 0.71. The variation of velocity grows from both ends with increasing Re due to the effect of the Ekman layer (Sobolík *et al.*, 2000). Because Taylor vortices fully develop at Re_{cr}, the velocity variation can be observed in the entire region along the axis. In order to investigate the Re_{cr}, the rotational speed of the inner cylinder was varied by 0.1 rad/s in each calculation near the Re_{cr}. As shown in **Fig. 2–8**, the fully developed variation of velocity magnitude could be first observed at Re = 82.2. On the other hand, the development of velocity was in transition at Re = 81.1. Therefore, the Re_{cr} for R_i/R_o = 0.714 is simply inferred to be 82.2. The theoretical Re_{cr} for R_i/R_o = 0.71 is about 81.1 (Di Prima and Swinney, 1981). This difference can be ignored. In fact, this amount of difference from theoretical Re_{cr} is shown when Re_{cr} is experimentally determined, e.g. by measuring the torque exerted by the fluid on the rotating inner cylinder (Coronado-Matutti *et al.*, 2004). Therefore, the method for evaluating Re_{cr}, focusing on the growth of variation of the velocity magnitude along the axis as proposed here, has sufficient accuracy.

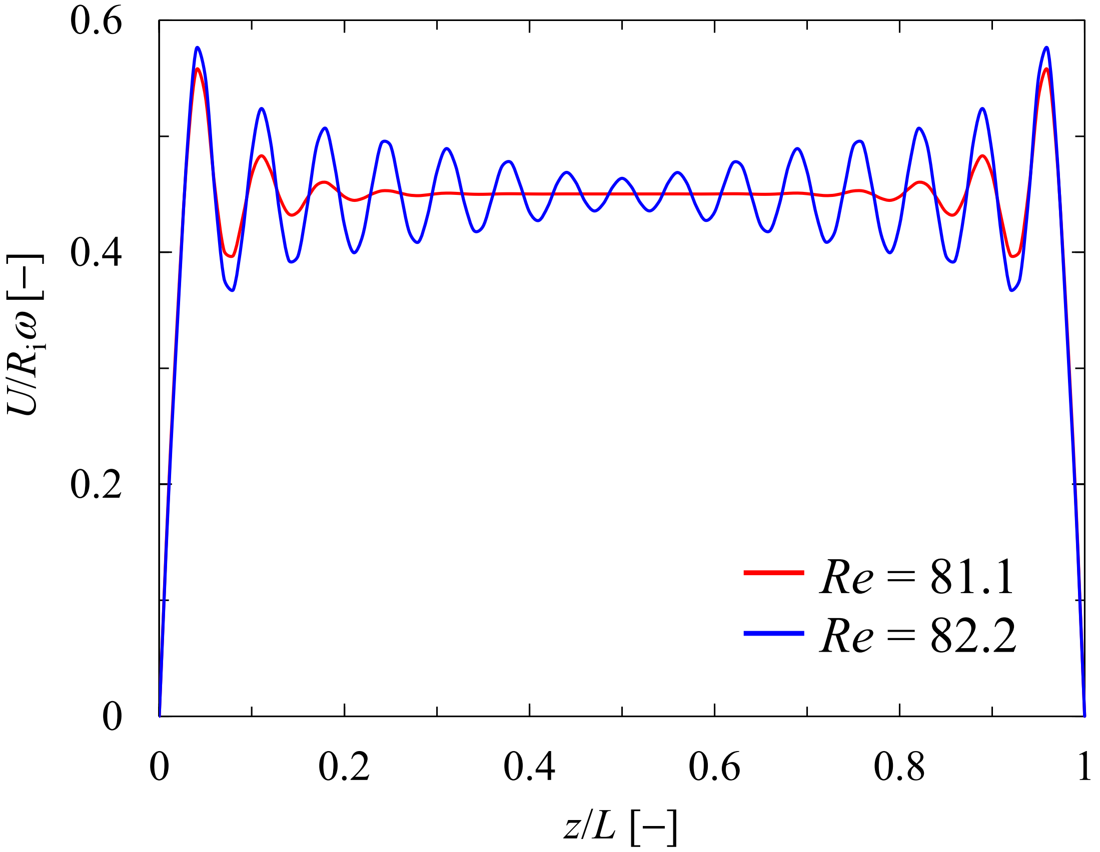

Fig. 2−8 Velocity distribution at the middle of the gap along the axis around Re_{cr}

2. 3. 3. Re_{cr} for shear-thinning fluids

In order to estimate Re_{eff} for shear-thinning fluid flows in the stirred tank reactor, Metzner–Otto method is widely used (Metzner and Otto, 1957). The outline of Metzner–Otto method is as follows: 1) A power number, N_p (= $P / \rho n^3 d^5$), against Re (N_p–Re) correlation curve is drawn as a reference for a given Newtonian fluid, as shown in **Fig. 2–9**. Here, N_p is independent of the viscosity. 2) The power number for a shear-thinning fluid is obtained from estimation of the power consumption, P, for the same impeller. 3) The corresponding Re, is estimated from the correlation curve for the Newtonian fluid, can be regarded as Re_{eff}.

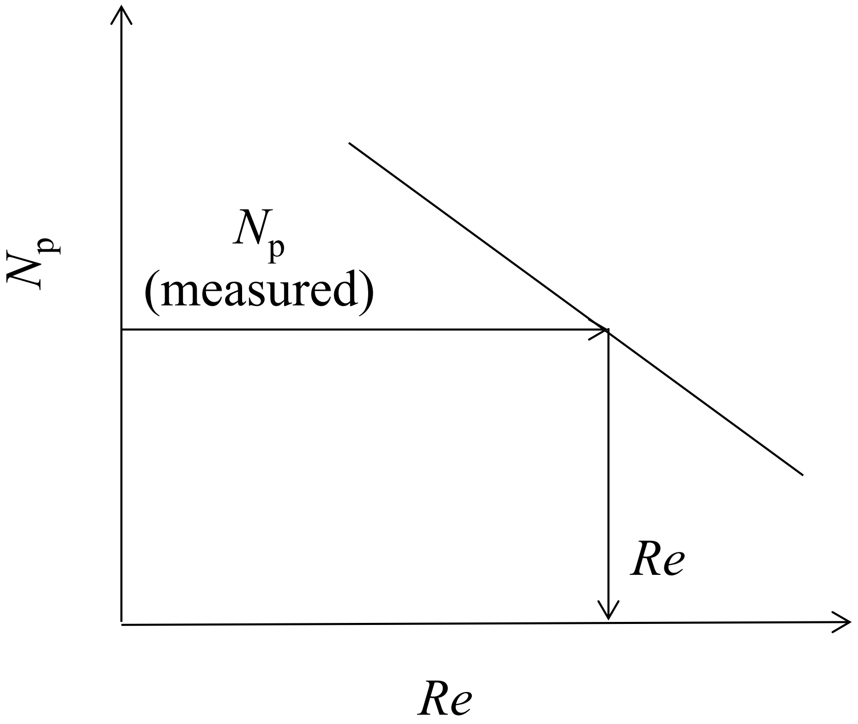

Fig. 2–9 N_p–Re correlation curve for a Newtonian fluid

According to Sinevic *et al*. (1986), for the TCFR, $N_{\mathrm{p\_TC}}$ is defined as,

$$N_{\mathrm{p\_TC}} = \frac{T\omega}{\rho\omega^3 L R_{\mathrm{i}}^4} \tag{2–6}$$

In this study, the torque, T, was calculated from the shear stress exerted at the surface of inner cylinder. **Fig. 2–10** shows the $N_{\mathrm{p\_TC}}$–Re correlation curve for the Newtonian fluid at $R_{\mathrm{i}}/R_{\mathrm{o}} = 0.71$.

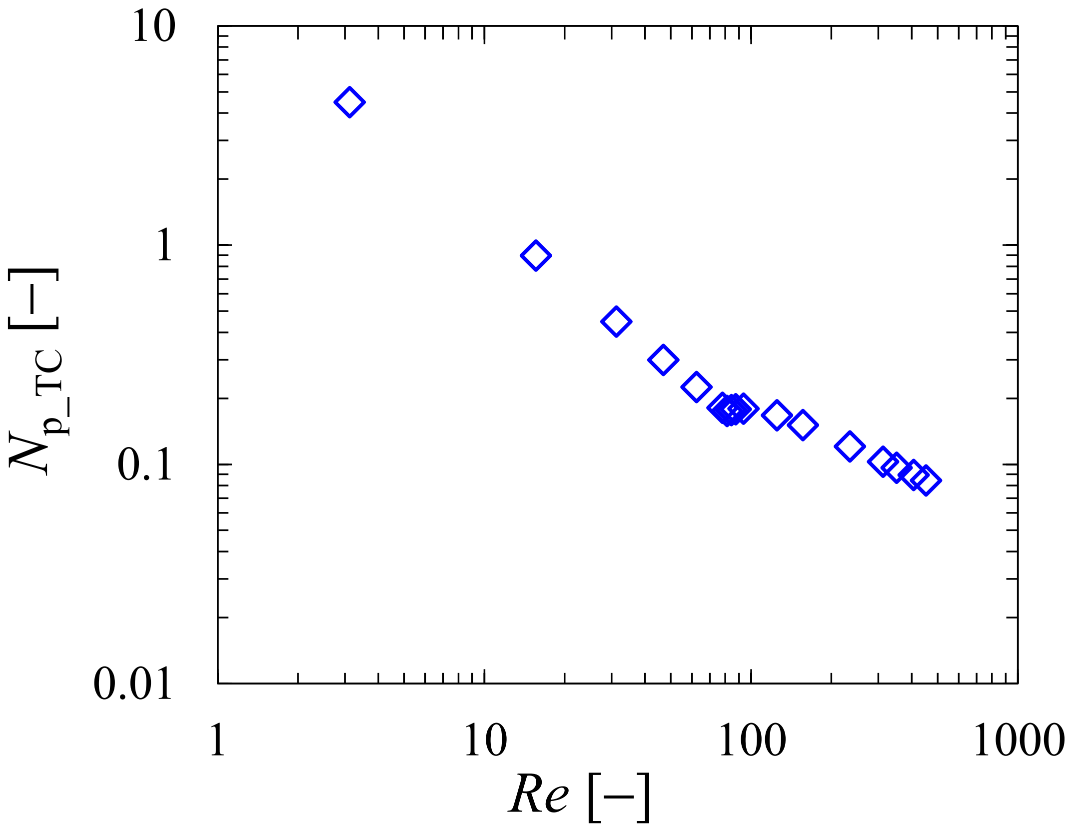

Fig. 2–10 $N_{\mathrm{p\_TC}}$–Re correlation curve for Newtonian fluids at $R_{\mathrm{i}}/R_{\mathrm{o}} = 0.71$

Around Re = 80, i.e. the transition region from Couette flow to Taylor vortex flow, the value of $N_{\mathrm{p\_TC}}$ is almost constant (about 0.18). This means that it is difficult to identify Re_{eff} from this correlation if $N_{\mathrm{p\_TC}}$ is near 0.18. Therefore, other method to determine Re_{eff} is required.

Meanwhile, for shear-thinning fluids, a generalized Re (Re_{g}) is often applied (Metzner and Reed, 1955; Kozicki *et al.*, 1966; Güzel *et al.*, 2009). The Re_{g} for Taylor–Couette flow is defined as follows:

$$Re_{\mathrm{g}} = \frac{\rho R_{\mathrm{i}} \omega d}{\eta(\dot{\gamma})|_{\dot{\gamma}=V/D}} \tag{2–7}$$

where, V is the representative velocity (usually $R_{\mathrm{i}}\omega$ in Taylor–Couette flow), and D is the representative length (usually d in Taylor–Couette flow). **Figure 2–11** shows the dependency of the critical Re_{g} for a shear-thinning fluid (n = 0.7 and β = 10 s) on the radius ratio ($R_{\mathrm{i}}/R_{\mathrm{o}}$). The theoretical Re_{cr} for Newtonian fluid system was derived by Taylor (1923) as shown in Eq. (2–8). The theoretical Re_{cr} (Eq. (2–8)) denoted dashed line in **Fig. 2–11**.

$$Re_{\mathrm{cr}} = \frac{\pi^4 (1 + d/2R_{\mathrm{i}})}{0.0571(1-0.652d/R_{\mathrm{i}}) + 0.00056(1-0.652d/R_{\mathrm{i}})^{-1}} \left(\frac{d}{R_{\mathrm{i}}}\right)^{-1/2} \tag{2–8}$$

As shown in **Fig. 2–11**, the critical Re_{g} was deviated from the theoretical Re_{cr}, especially for wider gap. From the practical viewpoint, the Re_{g} is inconvenient because not only the geometry (d and $R_{\mathrm{i}}/R_{\mathrm{o}}$) but also the rheological parameters must be considered for the prediction of the onset of Taylor–Couette instability.

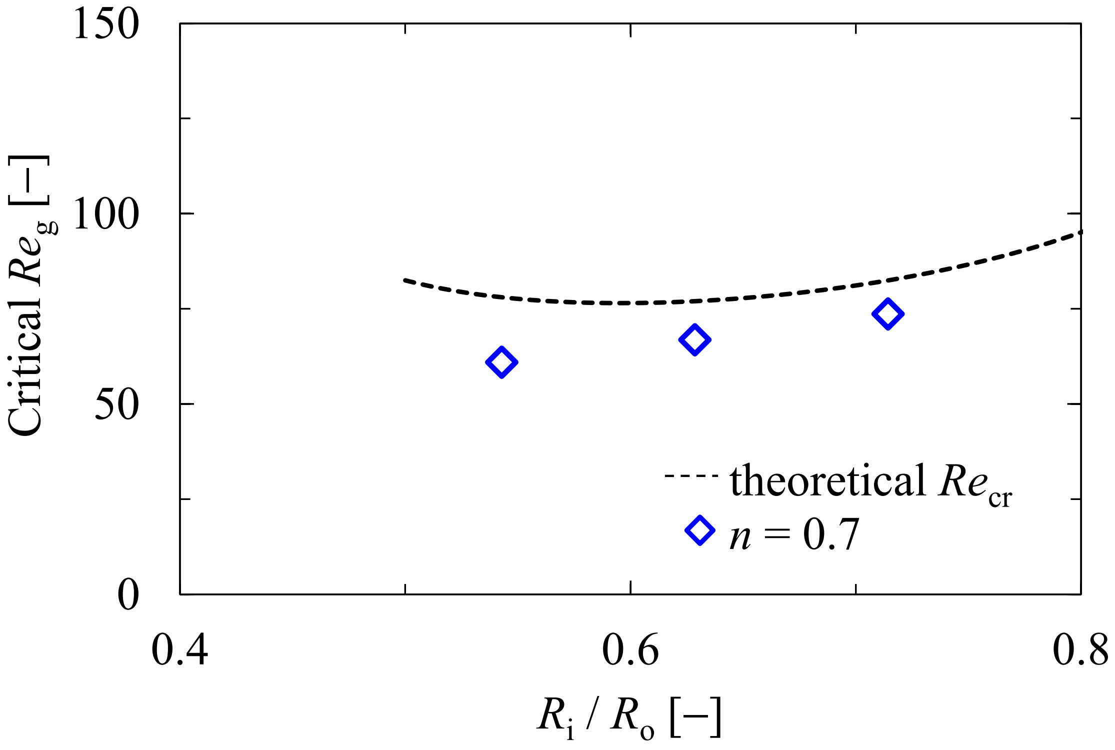

Fig. 2–11 The critical Re_g for a shear-thinning fluid (n = 0.7, β = 10 s)

According to Kaminoyama *et al*. (2011), the power consumption, P, in the stirred vessel is given by Eq. (2–9), assuming that P is a summation of the energy of viscous dissipation throughout the whole fluid in the vessel.

$$P = \sum_{i=1}^{N} \dot{\gamma}_i^2 \eta_i \Delta V_i \tag{2–9}$$

where N is the total mesh number, η_i [Pa·s] is the local viscosity, $\dot{\gamma}_i$ [1/s] is the local shear–rate and ΔV_i [m^3] is the cell volume. Here, ΔV_i was defined as $\Delta x_i \times \Delta y_i \times \Delta z_i$. The distributions of η and $\dot{\gamma}$ could be obtained from the results of numerical simulations of the flow analysis. The temperature change due to the viscous dissipation energy was negligible because the time scale for a heating time by the dissipation energy is typically quite large in comparison with the time scale until the generation of Taylor vortices (White and Muller, 2002). Eq. (2–10) can be obtained by substituting the effective viscosity, η_{eff}, into the local viscosity, η_{i}, so that η_{eff} is independent of the local position in the reactor.

$$\sum_{i=1}^{N} \dot{\gamma}_i^2 \eta_i \Delta V_i = \eta_{\mathrm{eff}} \sum_{i=1}^{N} \dot{\gamma}_i^2 \Delta V_i \tag{2–10}$$

Consequently, the term η_{eff} can be obtained by Eq. (2–11) by rearranging Eq. (2–10).

$$\eta_{\mathrm{eff}} = \frac{\sum_{i=1}^{N} \dot{\gamma}_i^2 \eta_i \Delta V_i}{\sum_{i=1}^{N} \dot{\gamma}_i^2 \Delta V_i} \tag{2–11}$$

Eq. (2–11) implies that η_{eff} can be given by an arithmetic mean of the local viscosity, η_{i}, using a weight of dissipation function, $\dot{\gamma}^2$, at each point. This method for the estimation of effective viscosity has been applied for other flow systems and verified, e.g. Rayleigh–Bénard convection with shear-thinning fluids (Parmentier, 1978; Jenny *et al.*, 2015).

Figure 2–12 shows the dependency of Re_{cr} calculated based on the effective viscosity obtained by Eq. (2–9) on the radius ratio (R_i/R_o) for various shear-thinning fluids at constant β (= 10 s). The theoretical Re_{cr} for Newtonian fluid system was derived by Taylor (1923) as shown in Eq. (2–8). The theoretical Re_{cr} (Eq. (2–8)) denoted by the dashed line in **Fig. 2–12**.

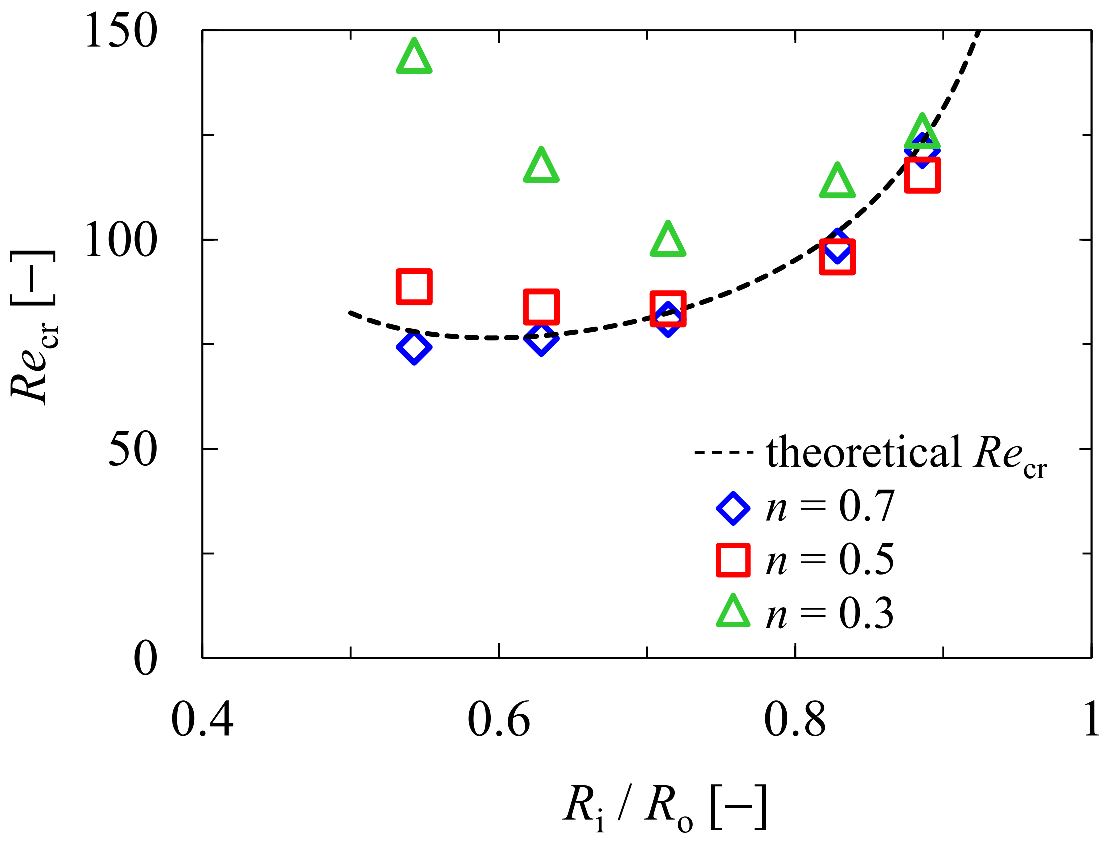

Fig. 2–12 Re_{cr} for various shear-thinning fluids

The Re_{cr} for shear-thinning fluids shows good agreement with the theoretical Re_{cr} except the cases of $n = 0.3$ and $R_i/R_o < 0.7$. This result indicated that Re_{cr} for a shear-thinning fluid with smaller n tends to deviate from the instability theory in wide gap systems. The smaller n means the stronger shear-thinning property that may lead to larger viscosity distribution in wider gap systems. In order to investigate the effect of viscosity distribution in the radial direction at Re_{cr} on the deviation from theoretical Re_{cr}, the ratio of the viscosity at the outer cylinder surface to the one at the inner cylinder surface at $z = 0.075$ m is summarized in **Fig. 2–13**.

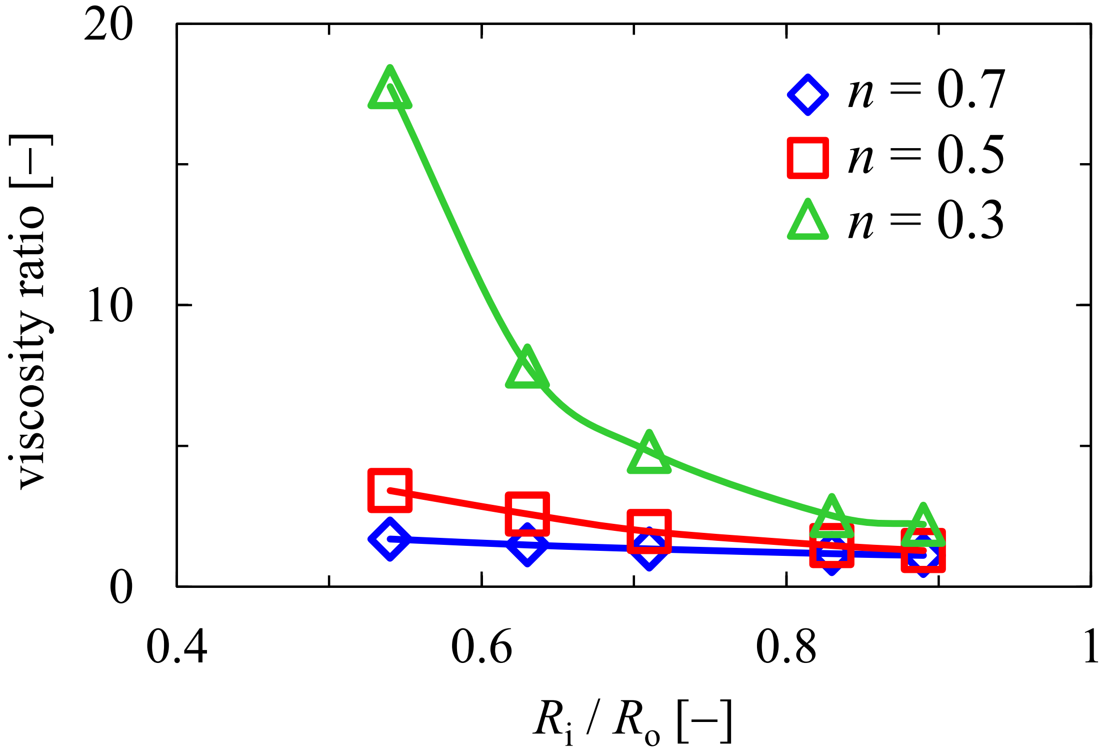

Fig. 2–13 Ratio of viscosity at the outer cylinder to the one at the inner cylinder at $z = 0.075$ m

As clearly shown in **Fig. 2–13**, the viscosity ratio becomes larger with the wider gap and stronger shear-thinning property. However, the TCFR for chemical processes is usually designed above $R_i/R_o = 0.7$. For example, $R_i/R_o = 0.75$ to gas-liquid contactor (Ramezani *et al.*, 2015), $R_i/R_o = 0.71$ to emulsion polymerization (Kataoka *et al.*, 1995) and $R_i/R_o = 0.75$ to photocatalytic reaction (Dutta and Ray, 2004). Furthermore, **Fig. 2–14** indicates that the Re_{cr} is independent of β for $n = 0.7$ and 0.5 in the case of $R_i/R_o = 0.71$. Therefore, it is concluded that Re_{cr} using η_{eff} derived from Eq. (2–11) is applicable to the TCFRs.

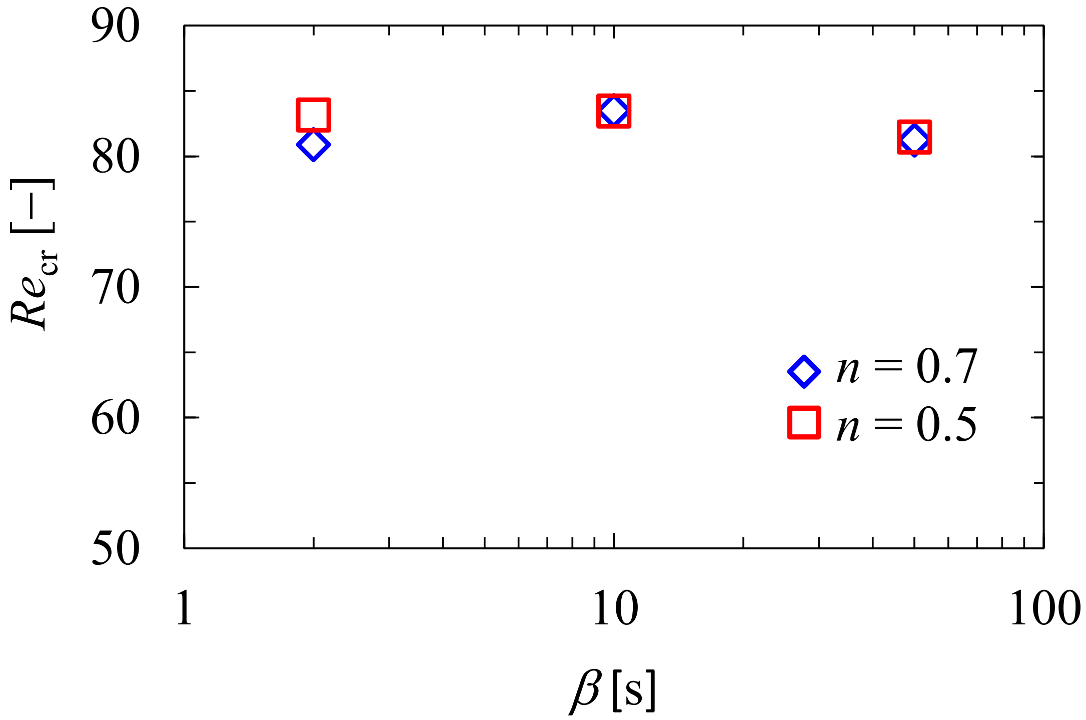

Fig. 2–14 Dependency of Re_{cr} on β for $n = 0.7$ and 0.5 in the case of $R_i/R_o = 0.71$

It is important to understand the radial position corresponds to η_{eff}. **Figure 2–15** shows the viscosity distribution at Re_{cr} in the radial direction ($R_{\mathrm{i}}/R_{\mathrm{o}} = 0.71$) at the axial position of the middle of apparatus, $z = 0.75$ m, where the end effect is not influenced. Below the rotational speed at the formation of Taylor vortices, the viscosity monotonically increased from the inner cylinder surface to the outer cylinder surface in association with the shear-rate distribution (e.g. Alibenyahia et al., 2014). The viscosity profile along the $(r–R_{\mathrm{i}})/d$ at Re_{cr} also increased monotonically. The position where the viscosity was identical with the η_{eff} was defined as the representative radial position, r^*. For example, η_{eff} were 0.0246 Pa·s for $n = 0.7$, the $(r^*–R_{\mathrm{i}})/d$ could be identified to 0.28 from **Fig. 2–15**. As η_{eff} for $n = 0.5$ and 0.3 were 0.00943 and 0.00399 Pa·s, the $(r^*–R_{\mathrm{i}})/d$ were identified to be 0.27 and 0.22, respectively. This means that the representative radial position gradually shifted toward the inner cylinder surface with higher intensity of shear-thinning property. In order to investigate the cause of this shift, the velocity and shear-rate distribution in the radial direction were analytically derived. **Figure 2–16** shows the profiles of (a) the circumferential velocity and (b) the shear-rate in the radial direction for Newtonian fluid ($n = 1$) and shear-thinning fluids ($n = 0.7, 0.5, 0.3$). The velocity and the shear-rate were normalized by $R_{\mathrm{i}}\omega$ and $R_{\mathrm{i}}\omega/d$, respectively. The power-law model fluid was used for shear-thinning fluids due to the simplicity of constitutive equation, as shown in Eq. (2–12):

$$\eta = K\dot{\gamma}^{n-1} \tag{2–12}$$

where K is a constant characterizing the fluid and is related to η_0 (Bird et al., 2007). By solving Navier–Stokes equation (Eq. (2–2)) with Eq. (2–12), the circumferential velocity distribution in the radial direction for Couette flow was obtained, as Eq. (2–13).

$$U_\theta = \frac{r\omega}{R_\mathrm{o}^{-2/n} - R_\mathrm{i}^{-2/n}} \left(R_\mathrm{o}^{-2/n} - r^{-2/n} \right) \tag{2–13}$$

Furthermore, the shear-rate distribution in the radial direction is given by Eq. (2–14).

$$\dot{\gamma} = -\frac{dU_\theta}{dr} = \frac{\omega}{R_\mathrm{o}^{-2/n} - R_\mathrm{i}^{-2/n}} \left\{ R_\mathrm{o}^{-2/n} + \left(\frac{2}{n} - 1 \right) r^{-2/n} \right\} \tag{2–14}$$

Note that Couette flow was assumed because the flow condition below Re_cr is sufficient to be discussed in this section. As shown in **Fig. 2–16** (a), the shape of velocity profile changed from linear to parabolic with increasing of strength of shear-thinning property. As a result, the shear-rate increased near the inner cylinder and decreases near the outer cylinder in **Fig. 2–16** (b). In other words, the magnitude of shear-rate inclined towards the inner cylinder with increasing of strength of shear-thinning property. Because the average viscosity was weighted with the dissipation function which is the square of $\dot{\gamma}$, the representative radial position was shifted toward the inner cylinder with increasing of shear-thinning property.

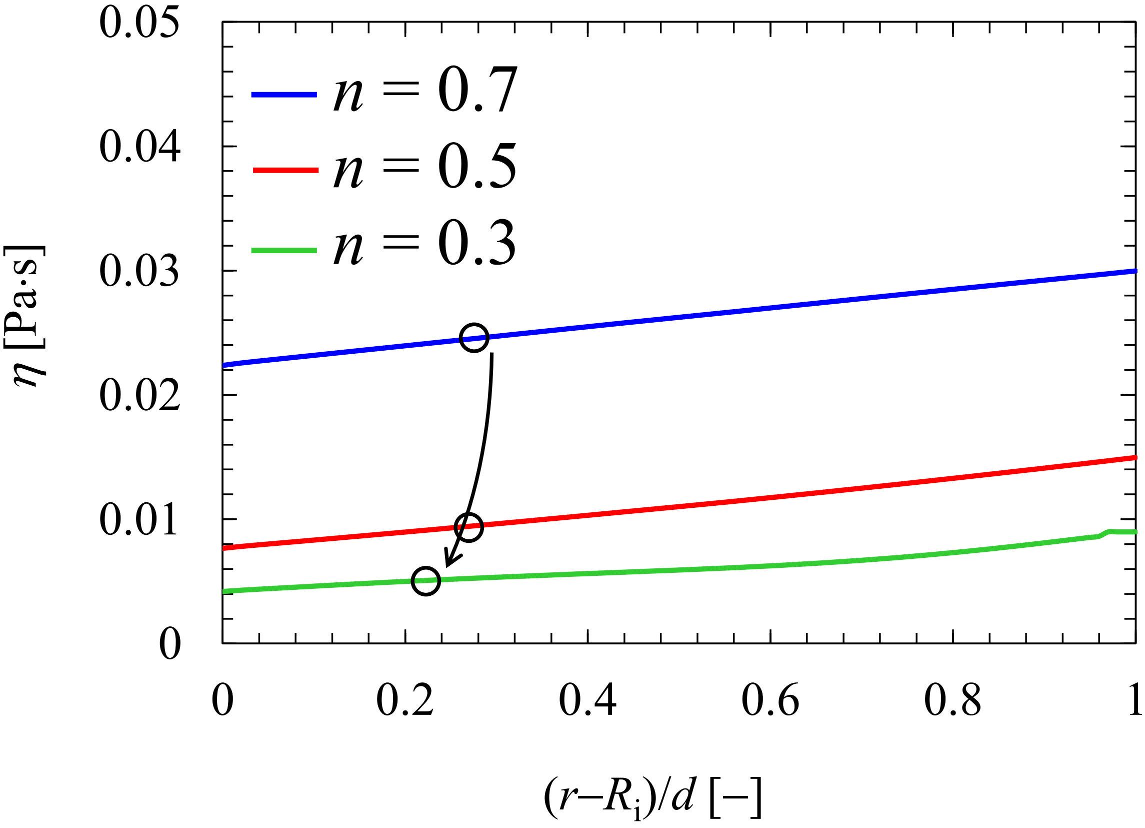

Fig. 2–15 Viscosity profiles in the radial direction: circles indicate $(r^*-R_i)/d$

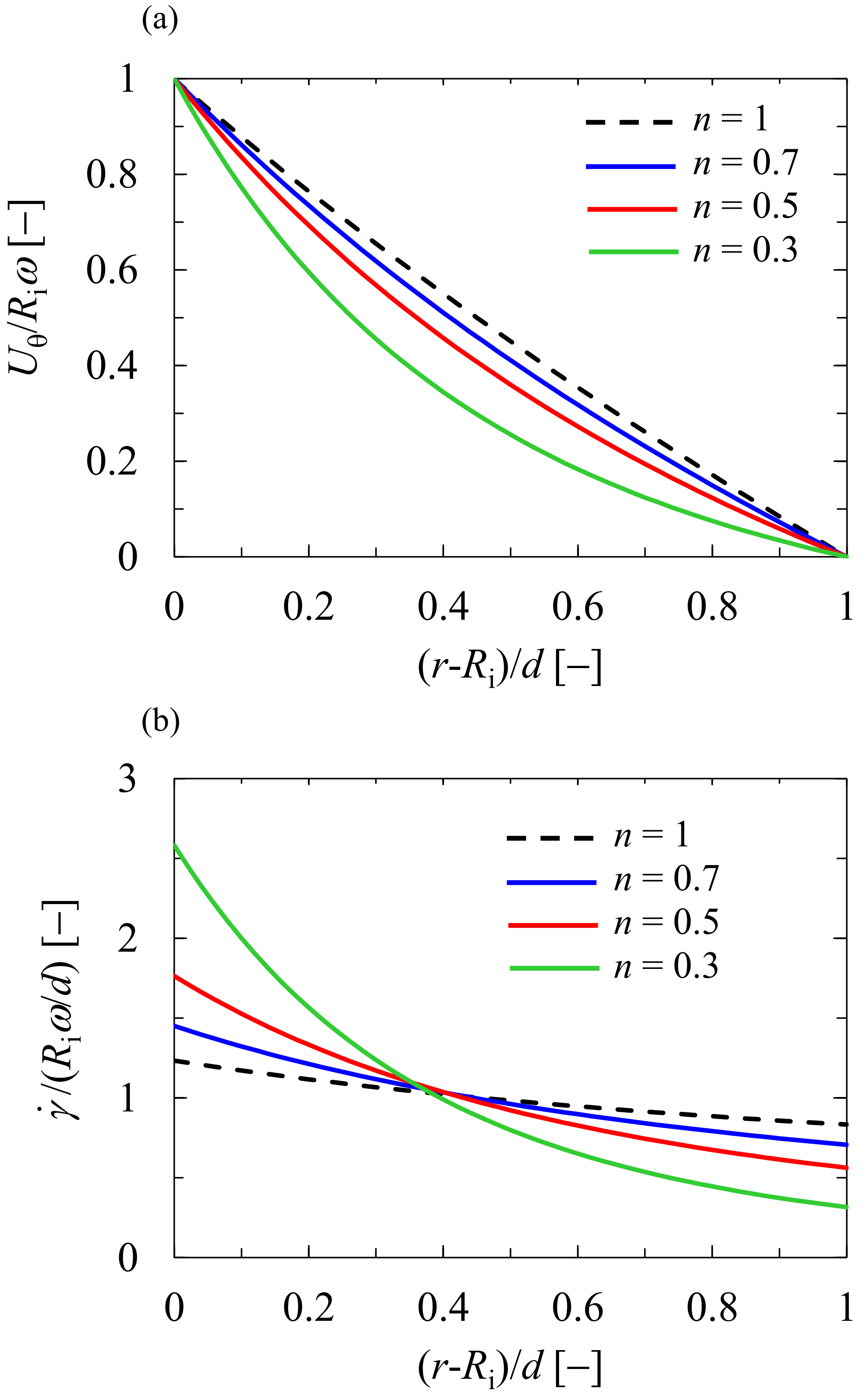

Fig. 2–16 Profiles for Couette flow in radial direction
(a) circumferential velocity and (b) shear-rate for power-law fluid

2. 3. 4. Prediction of critical condition

The procedure for the calculation of Re_{eff} in section 2. 3. 3. requires CFD simulation. In order to predict the critical rotational speed of inner cylinder, at which Re_{eff} exceeds Re_{cr}, without numerical simulation, it is necessary to find out the relation between the operational condition and the effective viscosity. In other words, a simple method to estimate the effective shear-rate from the operational condition should be constructed. **Figure 2–17** shows that the relation between the effective shear-rate and the rotational speed of inner cylinder for (a) n = 0.7, (b) n = 0.5, and (c) n = 0.3, obtained by numerical simulation. $\dot{\gamma}_{\mathrm{eff}}$ is the corresponding shear-rate to the η_{eff} obtained from the rheological properties **(Fig. 2–1)**. The $\dot{\gamma}_{\mathrm{eff}}$ is proportional to the rotational speed of inner cylinder as shown in Eq. (2–15), and the proportional constant, k, is the function of the geometry of apparatus ($R_{\mathrm{i}}/R_{\mathrm{o}}$):

$$\dot{\gamma} = k\omega \tag{2–15}$$

This relation was quite similar to Metzner–Otto's concept in the stirred tank (Metzner and Otto, 1957), and the proportional constant could be treated in the same way as the Metzner–Otto constant which is one of the most important parameters for designing the impeller in a stirred vessel for non-Newtonian fluids. As previously described, the proportional constants depend on the apparatus geometry.

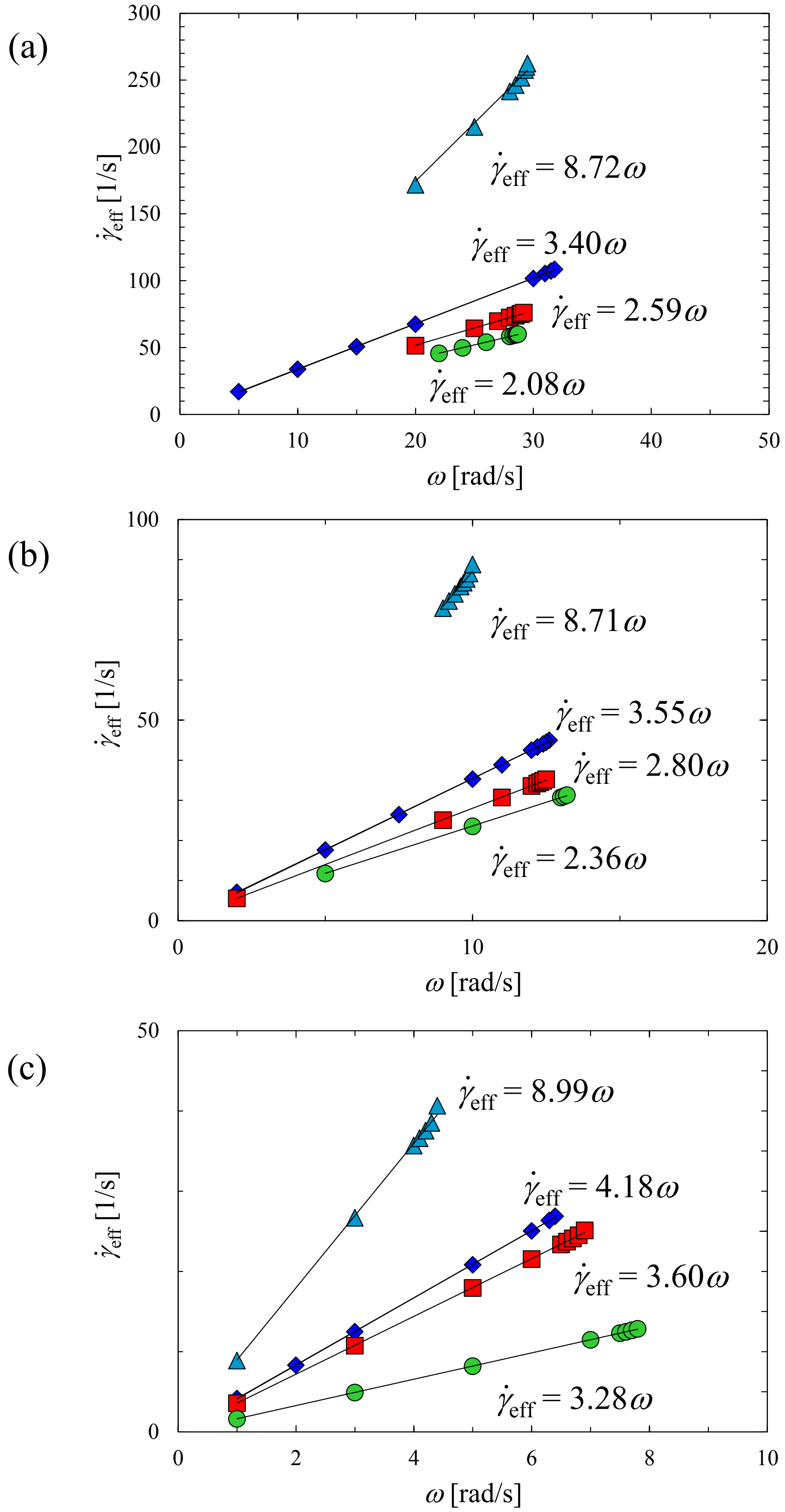

Fig. 2–17 Relationship between the rotational speed of inner cylinder and the effective shear-rate obtained by numerical simulation: (a) $n = 0.7$, (b) $n = 0.5$, and (c) $n = 0.3$

Figure 2–18 shows the dependency of k on the radius ratio for (a) $n = 0.7$, (b) $n = 0.5$ and (c) $n = 0.3$. For each n, the dependency of k on $R_\mathrm{i}/R_\mathrm{o}$ could be expressed by the following parabolic equation with three parameters (A, B and C):

$$k = A\left(\frac{R_\mathrm{i}}{R_\mathrm{o}}\right)^2 + B\left(\frac{R_\mathrm{i}}{R_\mathrm{o}}\right) + C \tag{2–16}$$

Furthermore, **Fig. 2–19** (a) – (c) shows the dependency of the values of A, B and C on rheological properties, n. From **Figs. 2–18** and **2–19**, Eq. (2–17) was derived.

$$k = 77.05n^{0.32}\left(\frac{R_\mathrm{i}}{R_\mathrm{o}}\right)^2 - 88.73n^{0.31}\left(\frac{R_\mathrm{i}}{R_\mathrm{o}}\right) + 26.85n^{0.21} \tag{2–17}$$

$\dot{\gamma}_\mathrm{eff}$ can be derived from the operational condition (ω), the rheological property (n) and the apparatus geometry ($R_\mathrm{i}/R_\mathrm{o}$) by using Eqs. (2–15) and (2–17). As a result, if the rheological property of the fluid is measured in advance, Re_eff can be calculated, and Re_cr can be easily predicted by this procedure.

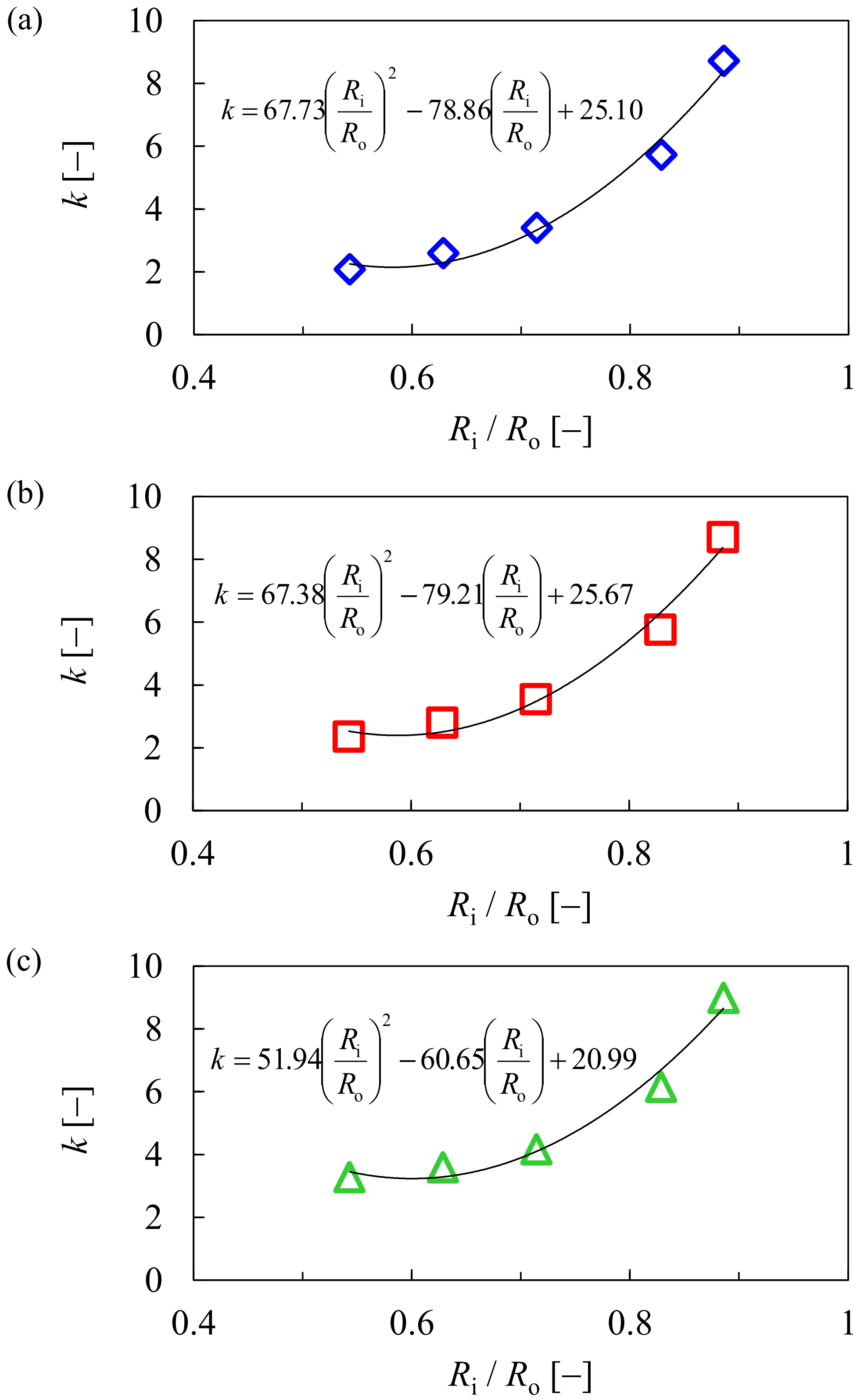

Fig. 2−18 Dependency of k on the radius ratio: (a) $n = 0.7$, (b) $n = 0.5$ and (c) $n = 0.3$

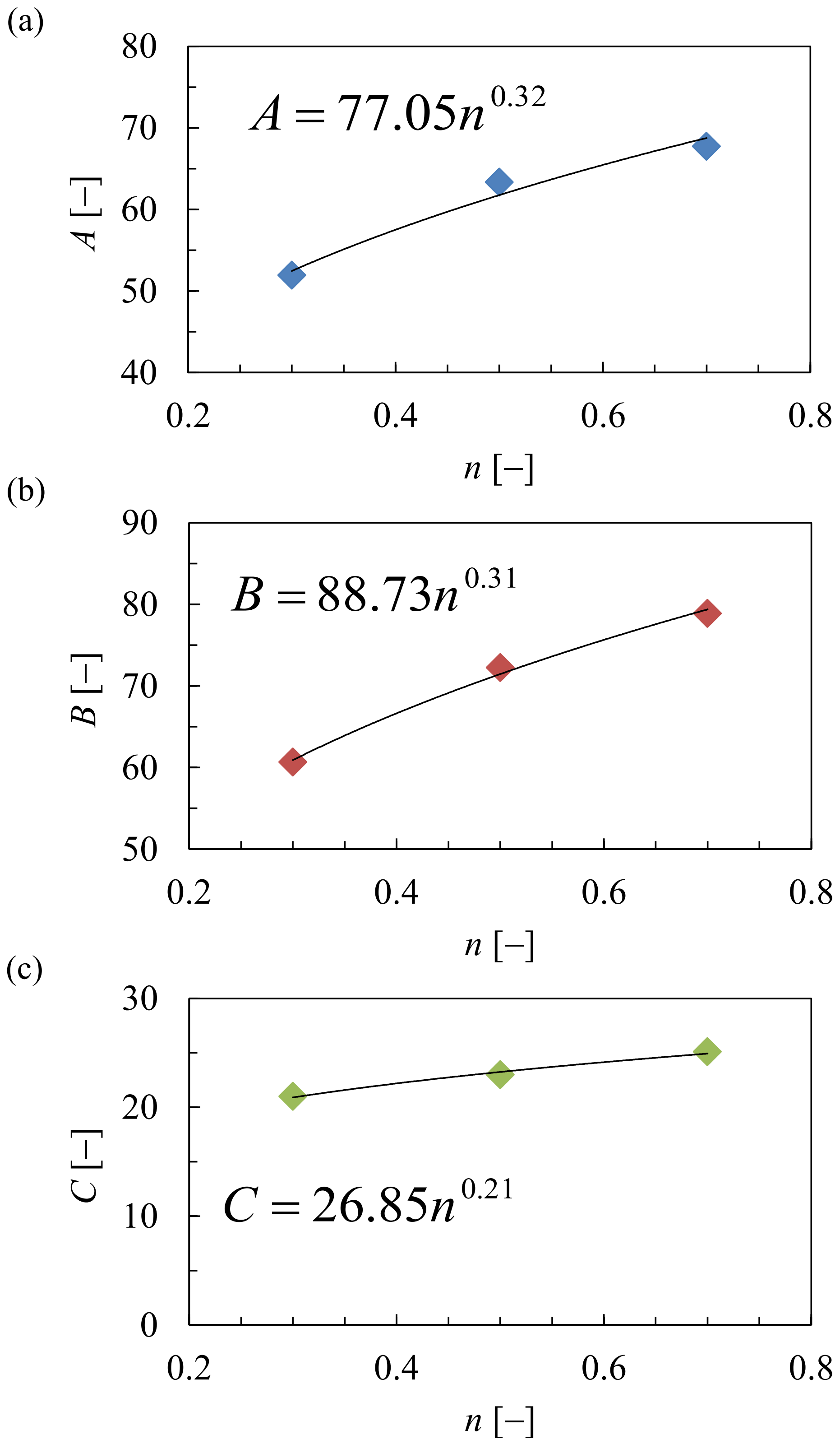

Fig. 2−19 Dependency of parameters on rheological properties: (a) A, (b) B, and (c) C

Based on Eq. (2−17), the prediction of the critical condition was conducted through an experiment of flow visualization. The value of k was 3.16 for CMC (n = 0.7) and 3.51 for XG (n = 0.5) when R_i/R_o was 0.71. Furthermore, the critical rotational speeds of the inner cylinder, ω_{cr}, were approximately estimated at 68.0 rad/s and 22.0 rad/s for CMC and XG, respectively. **Figure 2−20** shows the images of flow visualization for CMC (a) at ω = 65.0 rad/s, Re_{eff} = 76.75 and (b) at ω = 68.0 rad/s, Re_{eff} = 80.93, and **Fig. 2−21** shows the flow visualization for XG (a) at ω = 20.0 rad/s, Re_{eff} = 71.82 and (b) at ω = 22.0 rad/s, Re_{eff} = 82.62. As shown in Figs. 16 and 17, Taylor vortices were formed above ω_{cr} as predicted, and the prediction could be validated experimentally.

It is well known that Taylor vortices in viscoelastic fluids continuously oscillate in the axial direction because of the elastic instability (Larson *et al*., 1990; Shaqfeh *et al*., 1992; Baumert and Muller, 1995). However, the oscillation phenomenon was not observed for both CMC and XG. In future, it is necessary to check whether the proposed method using Eq. (2−17) is available even for viscoelastic fluids.

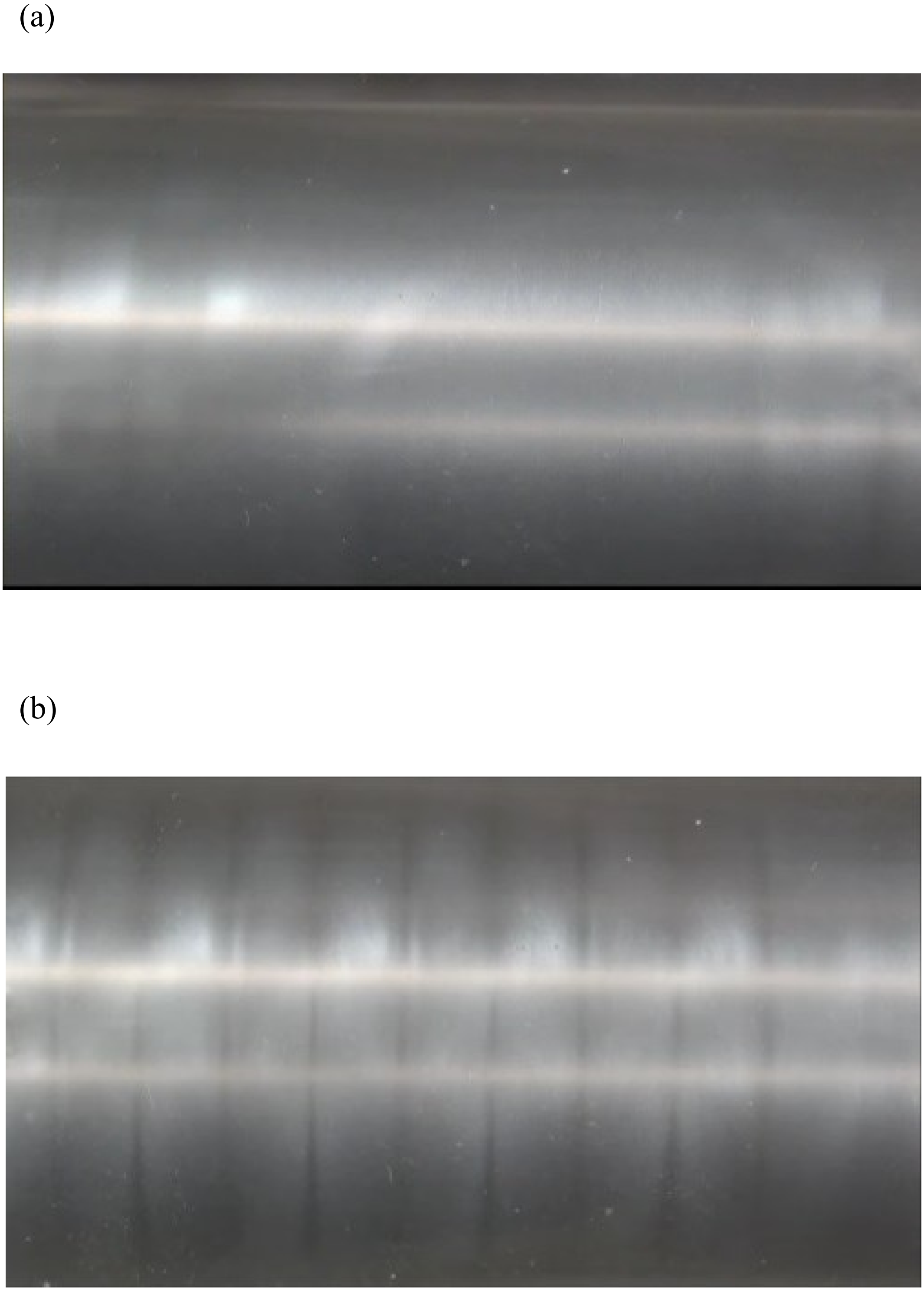

Fig. 2‒20 Flow visualization of CMC
at (a) $\omega = 65.0$ rad/s, $Re_{\mathrm{eff}} = 76.75$, (b) $\omega = 68.0$ rad/s, $Re_{\mathrm{eff}} = 80.93$

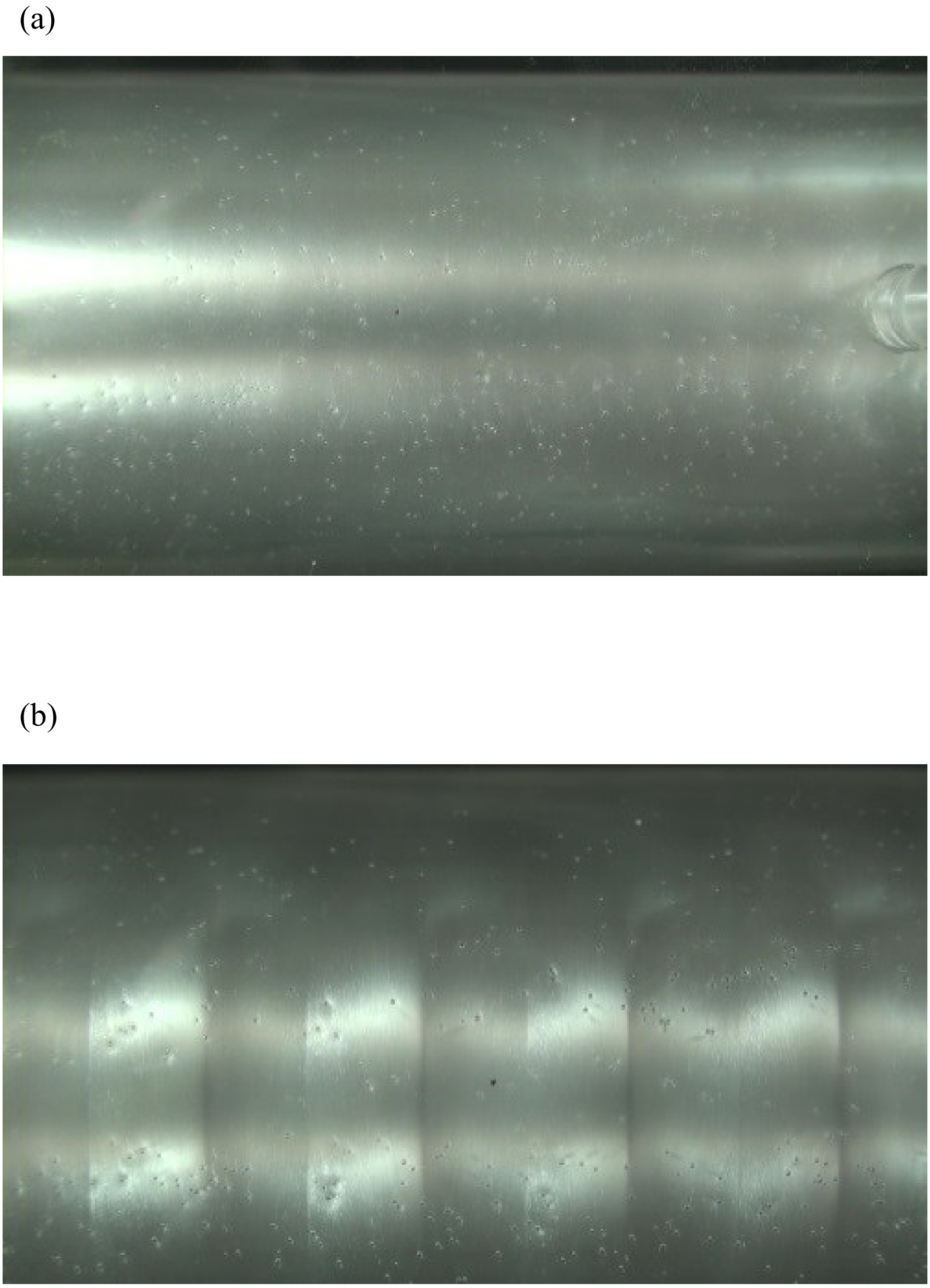

Fig. 2–21 Flow visualization of XG
at (a) $\omega = 22.0$ rad/s, $Re_{\mathrm{eff}} = 71.82$, (b) $\omega = 23.0$ rad/s, $Re_{\mathrm{eff}} = 82.62$

2. 4. Conclusions

In this chapter, Re_{eff} for the shear-thinning fluid system was defined based on the average viscosity, η_{eff}, in the reactor using a weight of dissipation function. When $R_{\mathrm{i}}/R_{\mathrm{o}}$ is larger than 0.71, Re_{cr} showed good agreement with the theoretical value for Newtonian fluid. On the contrary, in the TCFR with wider gaps (less than $R_{\mathrm{i}}/R_{\mathrm{o}} = 0.71$), Re_{cr} for shear-thinning fluids deviated from the theoretical Re_{cr} especially for $n = 0.3$ due to a wider viscosity distribution. However, as the TCFR is usually designed above $R_{\mathrm{i}}/R_{\mathrm{o}} = 0.71$ in researches about its application to chemical processes, Re_{cr} is applicable as the practical basis.

The $\dot{\gamma}_{\mathrm{eff}}$ estimated from η_{eff} obtained by the numerical simulation was proportional to the rotational speed of the inner cylinder. The proportional constant, k, depended not only on the apparatus geometry but also on the rheological property. The correlation equation for calculating k from $R_{\mathrm{i}}/R_{\mathrm{o}}$ and n was suggested. Furthermore, it was experimentally confirmed that the equation made it possible to predict the critical condition without numerical simulation.

Based on Re_{eff} defined in this chapter, the flow condition of Taylor–Couette flow with non-Newtonian fluids in the reactor can be identified. The basic bottleneck of non-Newtonian fluid process was overcome.

Nomenclature

A : parameter in Eq. (2–16), -

B : parameter in Eq. (2–16), -

C : parameter in Eq. (2–16), -

D : representative length, m

$\boldsymbol{D}$: rate of deformation tensor, 1/s

d : gap width, m

g : gravity acceleration (= 9.8 m/s^2), m/s^2

K : flow consistency index, Pa·s^n

k : proportional constant, -

L : length of TCFR, m

N_p : power number, -

$N_\mathrm{p\_TC}$: power number for Taylor–Couette flow reactor, -

n : power index, -

P : power consumption, J/s

p : pressure, Pa

r : radial position, m

r^* : representative radial position, -

Re : Reynolds number (= $\rho R_\mathrm{i} \omega d / \eta$), -

Re_cell : cell Reynolds number, -

Re_cr : critical Reynolds number, -

Re_eff : effective Reynolds number (= $\rho R_\mathrm{i} \omega d / \eta_\mathrm{eff}$), -

R_i : inner cylinder radius, m

R_o : outer cylinder radius, m

T : torque, N·m

t : time, s

Ta : Taylor number (= $(\rho R_\mathrm{i}\omega d / \eta)(d / R_\mathrm{i})$), -

Ta_cr : critical Taylor number, -

U : velocity magnitude, m/s

U_i : local velocity magnitude, m/s

U_x : velocity in x direction, m/s

U_Y : velocity in y direction, m/s

U_z : velocity in z direction, m/s

U_θ : circumferential velocity, m/s

$\boldsymbol{u}$: velocity, m/s

V : representative velocity, m/s

x : position, m

y : position, m

z : position, m

Greek letters

β : characteristic time, s

ΔV : volume of mesh, m^3

$\dot{\gamma}$: shear-rate, 1/s

$\dot{\gamma}_{\mathrm{eff}}$: effective shear-rate, 1/s

$\dot{\gamma}_i$: local shear-rate, 1/s

η : fluid viscosity, Pa·s

η_0 : zero shear-rate viscosity, Pa·s

η_∞ : infinite shear-rate viscosity, Pa·s

η_{eff} : effective viscosity, Pa·s

η_i : local viscosity, Pa·s

ρ : fluid density, kg/m^3

τ : shear stress, Pa

ω : angular velocity of inner cylinder, rad/s

ω_{cr} : critical angular velocity of inner cylinder, rad/s

References

B. Alibenyahia, C. Lemaitre, C. Nouar, N. Ait-Messaoudene, Revisiting the stability of circular Couette flow of shear-thinning fluids, *J. Non-Newton. Fluid Mech.*, **183–184**, 37–51 (2012)

B. M. Baumert, S. J. Muller, Flow visualization of the elastic Taylor–Couette instability in Boger fluids, *Rheol. Acta*, **34**, 147–159 (1995)

R. B. Bird, R. C. Armstrong, O. Hassager, Dynamics of Polymeric Liquids, vol. I, Fluid Dynamics, 2nd ed., John Wiley & Sons, Inc., U.S.A., 1987

R. B. Bird, W. E. Stewart, E. N. Lightfoot, *Transport Phenomena* 2^{nd} *ed.*, John Wiley & Sons, Inc., 2007

P. J. Carreau, Rheological equation s from molecular network theories, *Trans. Soc. Rheol.*, **16**, 99–127 (1972)

Y. I. Cho, K. R. Kensey, Effects of the non-Newtonian viscosity of blood on flows in a diseased arterial vessel. Part 1: steady flows, *Biorheology*, **28**, 241–262 (1991)

O. Coronado-Matutti, P. R. Souza Mendes, M. S. Carvalho, Instability of inelastic shear-thinning liquids in a Couette flow between concentric cylinders, *J. Fluids Eng.*, **126**, 385–390 (2004)

R. C. Di Prima, H. L. Swinney, Instabilities and transition in flow between concentric rotating cylinders, in: *Hydrodynamic Instabilities and the transition to Turbulence*, Springer-Verlag, 139–180 (1981)

P. K. Dutta, A. K. Ray, Experimental investigation of Taylor vortex photocatalytic reactor for water purification, *Chem. Eng. Sci.*, **9**, 5249–5259 (2004)

M. P. Escudier, I. W. Gouldson, D. M. Jones, Taylor vortices in Newtonian and shear-thinning liquids, *Proc. R. Soc. Lond. A*, **449**, 155−176 (1995)

M. P. Escudier, R. J. Poole, F. Presti, C. Dales, C. Nouar, C. Desaubry, L. Graham, L. Pullum, Observations of asymmetrical flow behavior in transitional pipe flow of yield-stress and other shear-thinning liquids, *J. Non-Newton. Fluid Mech.*, **127**, 143−155 (2005)

A. Fontaine, Y. Guntzburger, F. Bertrand, L. Fradette, M. -C. Heuzey, Experimental investigation of the flow dynamics of rheologically complex fluids in a Maxblend impeller system using PIV, *Chem. Eng. Res. Des.*, **91**, 7−17 (2013)

B. Güzel, I. Frigaard, D. M. Martinez, Predicting laminar−turbulent transition in Poiseuille pipe flow for non-Newtonian fluids, *Chem. Eng. Sci.*, **64**, 254−264 (2009)

R. Hubacz, M. Buczyńska, Starch gelatinization in Couette−Taylor flow apparatus, *Chem. Process Eng.*, **32**, 267−279 (2011)

R. Hubacz, N. Ohmura, E. Dluska, Intensification of processing using apparatus with Couette−Taylor flow, *J. Food Process Eng.*, **36**, 774−785 (2013)

J. Y. Hwang, K. S. Yang, Numerical study of Taylor−Couette flow with an axial flow, *Comput. Fluids*, **33**, 97−118 (2004)

M. Jastrzębski, H. A. Zaidani, S. Wroński, Stability of Couette flow of liquids with power law viscosity, *Rheol. Acta*, **31**, 264−273 (1992)

M. Jenny, E. Plaut, A. Briard, Numerical study of subcritical Rayleigh−Bénard convection rolls in strongly shear-thinning Carreau fluids, *J. Non-Newton. Fluid Mech.*, **219**, 19−34 (2015)

M. Kaminoyama, K. Nishi, R. Misumi, F. Otani, A method for determining the representative apparent viscosity of highly viscous pseudoplastic liquids in a stirred vessel by numerical simulation, *J. Chem. Eng. Japan*, **44**, 868−875 (2011)

K. Kataoka, N. Ohmura, M. Kouzu, Y. Simamura, M. Okubo, Emulsion polymerization of styrene in a continuous Taylor vortex flow reactor, *Chem. Eng. Sci.*, **50**, 1409–1416 (1995)

W. Kozicki, C. H. Chou, C. Tiu, Non-Newtonian flow in ducts of arbitrary cross-sectional shape, *Chem. Eng. Sci.*, **21**, 665–679 (1966)

R. G. Larson, E. S. G. Shaqfeh, S. J. Muller, A purely elastic instability in Taylor–Couette flow, *J. Fluid Mech.*, **218**, 573–600 (1990)

T. J. Lockett, S. M. Richardson, W. J. Worraker, The stability of inelastic non-Newtonian fluids in Couette flow between concentric cylinders: a finite-element study, *J. Non-Newton. Fluid Mech.*, **43**, 165–177 (1992)

T. Makino, T. Kaise, K. Sasaki, N. Ohmura, K. Kataoka, Isolated mixing region in a Taylor -vortex-flow reactor, *Kagaku Kogaku Ronbunshu*, **27**, 566–573 (2001)

K. Matsumoto, M. Ohta, S. Iwata, Numerical analysis of flow dynamics of milk in a milk-filling process, *Kagaku Kougaku Ronbunshu*, **41**, 1–10 (2015)

A. B. Metzner, J. C. Reed, Flow of non-Newtonian fluids–correlation of the laminar, transition and turbulent-flow regions, *AIChE J.*, **1**, 434–440 (1955)

A. B. Metzner, R. E. Otto, Agitation of non-Newtonian fluids, *AIChE J.*,**3**, 3–10 (1957)

M. Nemri, E. Climent, S. Charton, J. Y. Lanoë, Experimental and numerical investigation on mixing and axial dispersion in Taylor–Couette flow patterns, *Chem. Eng. Res. Des.*, **91**, 2346–2354 (2013)

T. C. Niederkorn, J. M. Ottino, Chaotic mixing of shear-thinning fluids, *AIChE J.*, **40**, 1782–1793 (1994)

E. M. Parmentier, A study of thermal convection in non-Newtonian fluids, *J. Fluid Mech.*, **84**, 1–11 (1978)

V. R. Patel, F. Ein-Mozaffari, S. R. Upreti, Effect of time delays in characterizing the continuous mixing of non-Newtonian fluids in stirred-tank reactors, *Chem. Eng. Res. Des.*, **89**, 1919–1928 (2011)

S. Poncet, R. D. Soghe, C. Bianchini, S. Viazzo, A. Aubert, Turbulent Couette–Taylor flows with endwall effects: A numerical benchmark, *Int. J. Heat Fluid Flow*, **44**, 229–238 (2013)

R. J. Poole, M. P. Escudier, Turbulent flow of viscoelastic liquids through an axisymmetric sudden expansion, *J. non-Newton. Fluid Mech.*, **117**, 25–46 (2004)

M. Ramezani, B. Kong, X. Gao, M. G. Olsen, R. D. Vigil, Experiment measurement of oxygen mass transfer and bubble size distribution in an air–water multiphase Taylor–Couette vortex bioreactor, *Chem. Eng. J.*, **279**, 286–296 (2015)

S. Saeed, F. Ein-Mozaffari, Using dynamic tests to study the continuous mixing of xanthan gum solutions, *J. Chem. Technol. Biotechnol.*, **83**, 559–568 (2008)

E. S. G. Shaqfeh, S. J. Muller, R. G. Larson, The effects of gap width and dilute solution properties on the viscoelastic Taylor–Couette instability, *J. Fluid Mech.*, **235**, 285–317 (1992)

V. Sinevic, R. Kuboi, A. A. Nienow, Power numbers, Taylor numbers and Taylor vortices in viscous Newtonian and non-Newtonian fluids, *Chem. Eng. Sci.*, **41**, 2915–2923 (1986)

V. Sobolík, B. Izrar, F. Lusseyran, S. Skali, Interaction between the Ekman layer and Couette–Taylor instability, *Int. J. Heat Mass Trans.*, **43**, 4381–4393 (2000)

T. Tanahashi, *CFD suutiryuutairikigaku*, Industrial Publishing & Consulting, Inc. (1993)

G. I. Taylor, Stability of a viscous liquid contained between two rotating cylinders, *Phil.*

Trans. Roy. Soc. A, **223**, 289−343 (1923)

J. M. White, S. J. Muller, Experimental studies on the stability of Newtonian Taylor−Couette flow in the presence of viscous heating, *J. Fluid Mech*., **462**, 133−159 (2002)

C. Y. Yap, W. I. Patterson, P. J. Carreau, Mixing with helical ribbon agitators: Part III Non-Newtonian fluids, *AIChE J*., **25**, 516−521 (1979)

K. Yasuda, R. C. Armstrong, R. E. Cohen, Shear flow properties of concentrated solutions of linear and star branched polystyrenes, *Rheol. Acta*, **20**, 163−178 (1981)

3. Process intensification of continuous starch hydrolysis with a Taylor–Couette flow reactor

3. 1. Introduction

In the previous chapter (Chapter 2), Re_{eff} for non-Newtonian fluid systems was proposed as the criteria for process design and control. In this chapter, in order to intensify a chemical process, TCFR is applied to chemical reaction with non-Newtonian fluids and the performance is evaluated based on Re_{eff}. As a model reaction, an enzymatic hydrolysis of starch is selected. This reaction is widely found in food processing or bioprocess, etc. Starch is transformed into useful and added-value materials used in many industries through the hydrolsysis.

The starch hydrolysis process consists of two steps; gelatinization and saccharification, as shown in **Fig. 3–1**. The fluid denotes the significant increase in viscosity in the gelatinization process, and the gelatinized starch become non-Newtonian fluid having a shear-thinning property. On the other hand, the viscosity of the fluid drastically decreases in the processing of enzymatic saccharification. One of the major difficulties in designing the starch hydrolysis process is this sharp change in the rheological property. Furthermore, the performance of gelatinization process depends on heat transfer, while that of saccharification process depends on mixing in the reaction. This difference of key factor between gelatinization and saccharification makes difficult to convert a batch process to continuous one using a conventional stirred vessel. At high concentration of starch suspension, conventional mixing operations with a stirred vessel are difficult because gelatinized starch has extremely low fluidity and a cavern is formed around the impeller. There are many challenges in overcoming these problems. Kelder *et al.* (2004) applied a curved tube to starch gelatinization and successfully showed a Dean vortex reduced a channeling phenomenon. However, the concentration of starch suspension was low (100 g/L) compared with the required concentration in industry (300–350 g/L). In order to treat higher concentration of starch, many researchers applied extruders to simultaneous gelatinization and saccharification (e.g. Reinikainen *et al*., 1986; Komolprasert and Ofoli, 1991; Baks *et al*., 2008; Emin and Schuchmann, 2013). However, because extruders were developed for the handling of the concentrated gelatinized starch, it is not perfectly suitable for mixing in the saccharification process. In order to improve the efficiency of continuous starch gelatinization and saccharification, Paolucci-Jeanjean *et al*. (2000) proposed a membrane reactor. However, the concentration of starch suspension was also limited to 100 g/L.

In this chapter, in order to improve the efficiency of the continuous starch hydrolysis process at higher concentration of starch, TCFR was employed. In the gelatinization process, the Couette flow is widely formed because of the high viscous fluid. The Couette flow applies shear to the starch suspension and thus enhances heat transfer compared with the case of no rotation. In addition, due to a shear-thinning property in highly-viscous gelatinized starch, shear flow produced by the rotation of the inner cylinder can reduce drag of fluid flow. Consequently, the gelatinized starch suspension can be transported with lower pump input. In the saccharification process, the Taylor vortex flow can be formed. The cellular vortex motion enhances mixing with enzyme as well as heat transfer. It is expected that the TCFR can break through this difficulty and achieve process intensification of continuous starch hydrolysis.

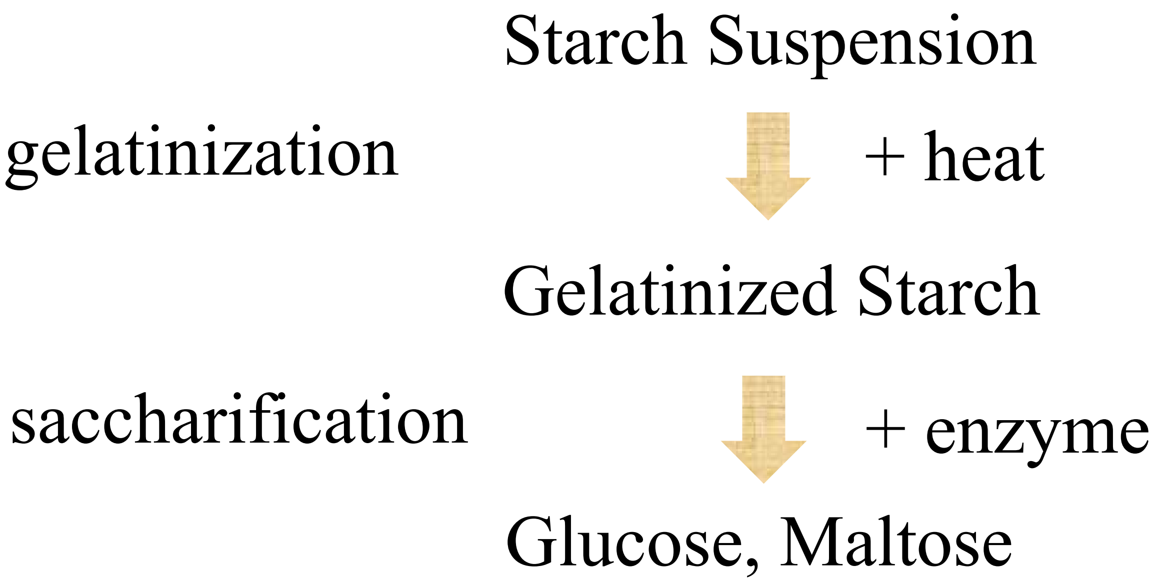

Fig. 3–1 Starch hydrolysis process

3. 2. Materials and methods

3. 2. 1. Experimental apparatus

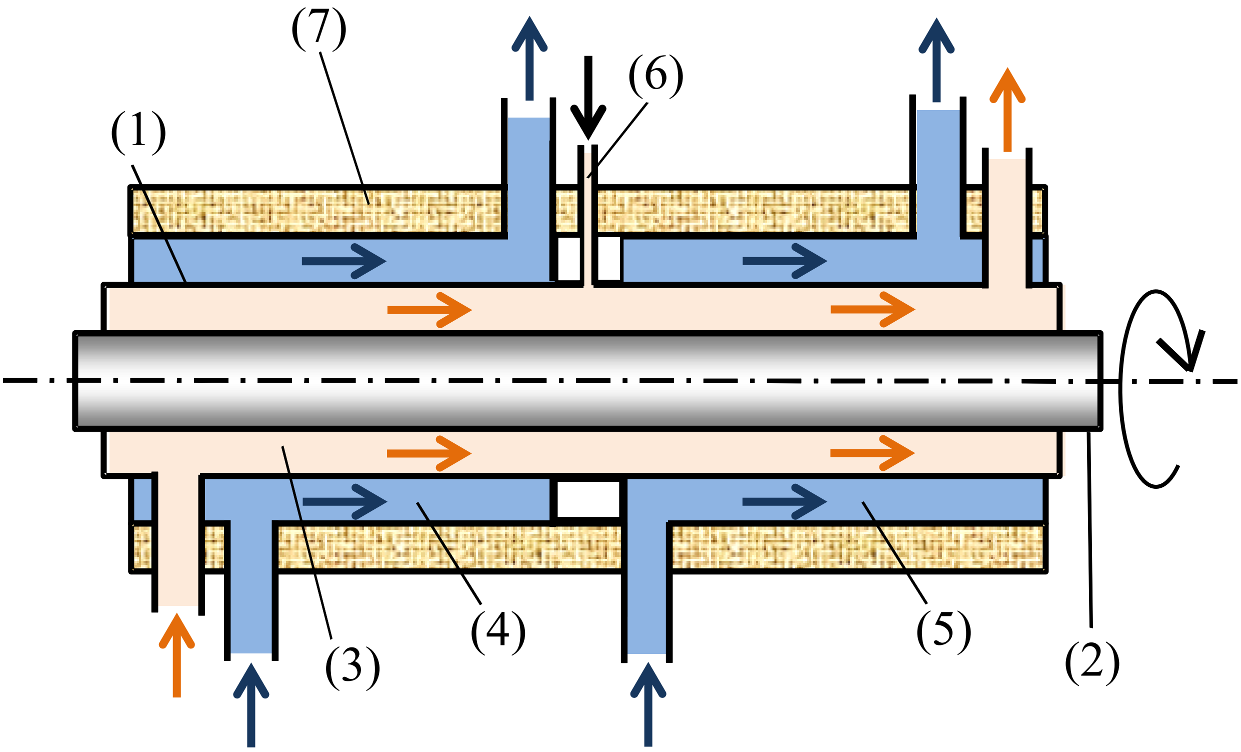

Fig. 3–2 TCFR with water jackets, (1) Stationary outer cylinder (2) Rotating inner cylinder (3) Starch suspension (4) Hot water (5) Variable temperature water (6) Enzyme injection port (7) Insulator

The experimental apparatus (**Fig. 3–2**) consisted of concentric cylinders (length: 300 mm), rotating inner cylinder (outer radius: 12.5 mm), the fixed outer cylinder (inner radius: 17.5 mm) with a heating water-jacket. All parts of this apparatus were made of stainless steel. The starch suspended in 25°C water was introduced into the gap between the cylinders. The water jacket divided into two sections was employed for spatial temperature control for the gelatinization process which requires high temperature and the enzymatic saccharification process where moderate temperature is preferable. The temperature of the anterior half part of the water jacket (gelatinization process: 0 – 150 mm) was 85°C and that of the posterior half part (saccharification process: 150 – 300 mm) was reduced to 35°C. By injecting enzyme (α-amylase: derived from *Bacillus licheniformis*) at the middle point of the reactor, continuous starch hydrolysis was conducted in the downstream. Initial starch concentration of the suspension, C_0, was varied from 50 to 300 g/L. The axial velocity of starch slurries was 0.00024 m/s. The rotation speed of the inner cylinder was varied from 0 to 97 rad/s. The experimental conditions are summarized in **Table 3–1**. Furthermore, rheological properties of the effluent were measured using a stress control rheometer (MCR-301, Anton Paar GmbH or HAAKE Viscotester 550, Thermo Fisher Scientific Inc.).

Table 3−1 Experimental condition

Initial ungelatinized starch concentration C_0 [g/L]	50, 100, 150, 300
Inlet axial velocity of starch slurries u_{ax} [m/s]	0.00024
Rotational speed of the inner cylinder ω [rad/s]	0, 2, 5, 10, 15, 22, 47, 97
Inlet temperature T_{in} [°C]	25
Temperature of gelatinization process T_{ge} [°C]	85
Temperature of saccharification process T_{sa} [°C]	35, 40, 55, 85
Enzyme volumetric flow rate v_e [mL/h]	0.1, 0.3, 0.6, 0.9, 1.8
Starch from wheat (Wako Pure Chemical Industries, Ltd.) Termamyl 120L (α-amylase)	

3. 2. 2. Gelatinization

The gelatinization of starch was conducted by using the TCFR. For this experiment, enzyme was not used. This means that all parts of the reactor volume were utilized for gelatinization. Thus, the temperatures of the two jackets were set at 85°C.

Samples (3 g) taken from the outlet were immediately dissolved in 50°C water of 100 mL and then the solution was kept at 50°C in a thermostatic bath in order to avoid starch retrogradation. At this temperature, gelatinization does not proceed. Afterwards, 0.5 mL of the solution was added to the mixture of iodine reagents 2.5 mL (0.15 % I_2 and 0.5 % KI) and distilled water 4.5 mL. Finally, light absorbance of a wavelength 630 nm was measured at room temperature with a UV−VIS spectrophotometer (MPS2400, SHIMADZU Co., Ltd.) to determine the degree of gelatinization.

3. 2. 3. Enzymatic saccharification

The anterior and posterior half parts of the reactor were used for gelatinization and saccharification, respectively. The α-amylase was introduced through an enzyme injection port installed at the middle of the reactor. The enzyme volumetric flow rate, v_e, was varied from 0.1 −1.8 mL/h through all the hydrolysis experiments. Samples of the product were taken at the outflow of the apparatus. In order to stop enzymatic saccharification, samples were cooled immediately to about 0°C and their pH was reduced to 2 by the addition of HCl. The sample was centrifuged at 2000 G for more than 1800 s to separate solids from the liquid phase. The concentration of the reducing sugar was determined by the dinitro salicylic acid (DNS) method (2-hydroxy-3,5-dinitrobenzoic acid, aqueous solution of 10 g/L 3,5-dinitrosalicylate, 16 g/L NaOH and 300 g/L potassium sodium tartrate 4-hydrate). With the addition of the DNS reagent, the sample became an orange color and the concentration of the reducing sugar, C_{rs}, could be analyzed with the UV−VIS spectrophotometer at a wavelength of 540 nm.

3. 2. 4. Numerical analysis

In order to understand and optimize the starch processing in the TCFR, a numerical calculation is a powerful tool. The numerical simulation of starch gelatinization and saccharification requires simultaneous calculation of flow hydrodynamics, heat transfer, and starch gelatinization and saccharification rate. Such simulations also require knowledge of a model describing rheological properties of wheat starch slurry during the entire processes of gelatinization and saccharification. In the successive processes, the apparent viscosity intricately changes. This viscosity change may cause serious numerical problems. Hubacz *et al.* (2013) experimentally proposed the rheological model during gelatinization. Furthermore, using numerical simulation with the rheological model, they successfully showed that Taylor vortices were effective for the improvement of gelatinization. According to Hubacz *et al.* (2013), gelatinization sufficiently could proceed until the enzyme injection point under this experimental condition. Therefore, the numerical simulation in this study was limited to the saccharification process (150 – 300 mm). However, there is no available model between rheological properties and reaction kinetics for saccharification. **Figure 3–3** shows the relationship between the yield of reducing sugar, C_{rs}/C_0, and rheological properties of the effluent at C_0 = 50 g/L and T_{sa} = 45°C. Keeping the residence time, i.e. reaction time, the yield was varied by controlling the volumetric flow rate of enzyme. As shown in **Fig. 3–3**, if a small amount of gelatinized starch is hydrolyzed, the viscosity dramatically decreases. And, above C_{rs}/C_0 = 0.11, the fluid viscosity was almost independent of C_{rs}/C_0. From these results, because the viscosity decreasing occurs only at the initial stage of saccharification, the effluent viscosity and density can be used for the representative physical properties in the saccharification process.

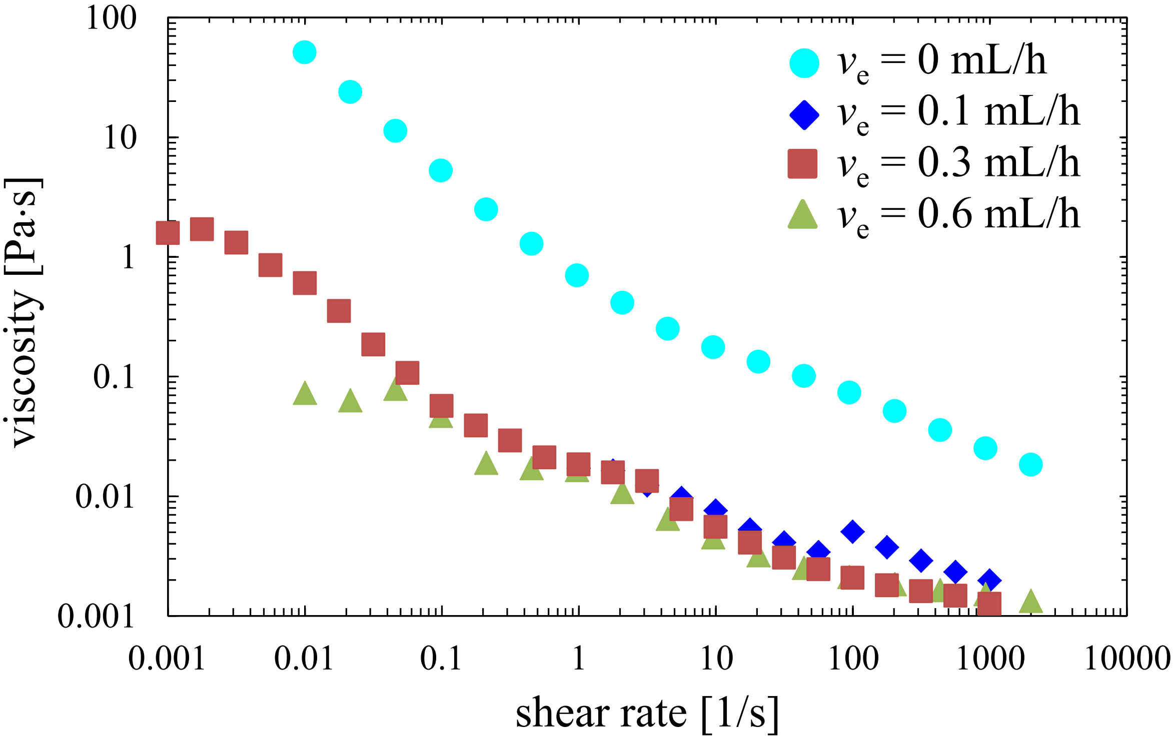

Fig. 3–3 Rheological properties of effluent at various v_e (C_0 = 50 g/L, ω = 10 rad/s)

In this simulation, fluids were considered as the incompressible fluid, and the three-dimensional steady state was assumed. The governing equations are the conservation equation of mass, momentum, heat and species given by

$$\nabla \cdot \boldsymbol{u} = 0 \tag{3–1}$$

$$\frac{\partial \boldsymbol{u}}{\partial t} + (\boldsymbol{u} \cdot \nabla)\boldsymbol{u} = -\frac{\nabla p}{\rho} + \frac{1}{\rho}\nabla \cdot (2\eta \boldsymbol{D}) + \boldsymbol{g} \tag{3–2}$$

$$\frac{\partial}{\partial t}(\rho C_p T) + \nabla \cdot (\rho C_p T \boldsymbol{u}) = \nabla \cdot (\lambda \nabla T) \tag{3–3}$$

$$\frac{\partial}{\partial t}(\rho X_j) + \nabla \cdot (\rho X_j \boldsymbol{u}) = \nabla \cdot (\rho D_j \nabla X_j) \tag{3–4}$$

where $\boldsymbol{u}$ is the velocity, t is the time, p is the pressure, $\boldsymbol{g}$ is the gravitational acceleration, $\boldsymbol{D}$ is the deformation rate tensor, C_p is the specific heat capacity, T is the temperature, λ is the thermal conductivity, X_j is the mass fraction of the species j and D_j is the diffusion coefficient of the species j. Here, the viscous dissipation energy was neglected. As described by Pineda-Gómez *et al.* (2012) and Hubacz *et al.* (2013), the values of C_p, λ, and D_j were chosen as 4,182 J/kg·K, 0.6 W/m·K and 10^{-13} $\mathrm{m^2/s}$, respectively. All the simulation in this study was conducted using ANSYS 14.5 (Fluent, Ansys Inc.). The second-order upwind scheme was used to discretize governing equations. The pressure-velocity coupling was performed usingthe SIMPLE scheme.

The density and viscosity of enzyme were assumed to be same as water, 1000 kg/m^3 and 0.001 Pa·s at 20°C, respectively. Non-Newtonian properties of the effluent were modeled by Carreau model (Carreau, 1972):

$$\eta = (\eta_0 - \eta_\infty)\left[1 + (\beta \cdot \dot{\gamma})^2\right]^{(n-1)/2} + \eta_\infty \tag{3–5}$$

where η_0 is the zero shear-rate viscosity, η_∞ is the infinite shear-rate viscosity, $\dot{\gamma}$ is the shear-rate, β is the characteristic time and n is the power index. Here, the shear-rate is defined as $\dot{\gamma} = \sqrt{2\boldsymbol{D}:\boldsymbol{D}}$, which is the magnitude of the rate of deformation tensor. When the square root is taken, the sign must be so chosen that $\dot{\gamma}$ is a positive quantity. As an example, rheological properties of the effluent for C_0 = 50 and 300 g/L are shown in **Fig. 3–4**. The solid lines in **Fig. 3–4** are viscosity changes obtained by the Carreau model. The model parameters used in the calculation are given in **Table 3–2**.

Table 3–2 Carreau model parameters for various effluents

	η_0 [Pa·s]	η_∞ [Pa·s]	n [–]	β [s]
C_0 = 50 g/L				
ω = 10 rad/s	0.05	0.0007	0.1	0.76
C_0 = 300 g/L				
ω = 10 rad/s	0.5471	0	0.43	25
47 rad/s	0.746	0	0.28	1.6
97 rad/s	14.96	0.002	0.23	50

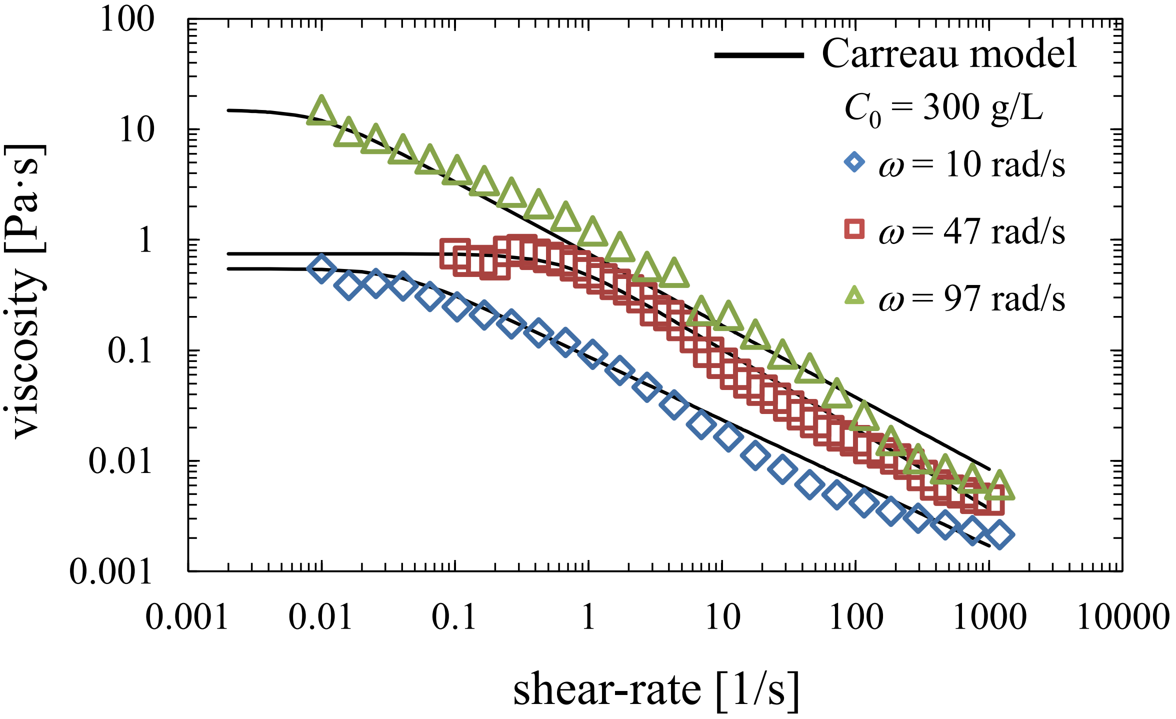

Fig. 3–4 Rheological properties of effluent at various ω (C_0 = 300 g/L)

The 3D simulation was conducted with 2,205,000 cells arrayed in staggered grids. As in the case with the experiment, the enzyme was introduced from a nozzle and joined the gelatinized starch which flowed in the annular space. In this simulation, the run-up inlet zone for the gelatinized starch was 0.02 m. The detailed information about the computational domain was shown in **Fig. 3–5**. The boundary conditions for this simulation were as follows:

- ☐ Inlet boundary conditions: The constant axial inlet velocity of gelatinized starch was imposed at 0.00024 m/s; the temperature of the fluid was 85°C; the constant axial inlet velocity of enzyme from the nozzle, u_e, was 0.00016 m/s which corresponds to $v_e = 1.8$ mL/h.
- ☐ Outer cylinder boundary conditions: All components of velocity were 0 m/s; the temperature was set at 55°C; the temperature of run-up zone was set at 85°C; insulation of heat and mass.
- ☐ Inner cylinder boundary conditions: The circumferential velocity was given by ωR_i [m/s]; the axial and radial velocity were 0 m/s; insulation of heat and mass.
- ☐ Nozzle boundary condition: The temperature of surface set at 25°C; insulation of heat and mass.
- ☐ Outlet boundaries: because of the possibility of “back flows” at the outlet, Fluent Pressure Outlet Boundaries were chosen. It was assumed that the gauge pressure was 0 for the surface of the inner cylinder, for other radial positions the pressure was calculated using the expression $\partial p/\partial r = \rho u_\theta^2/r$.

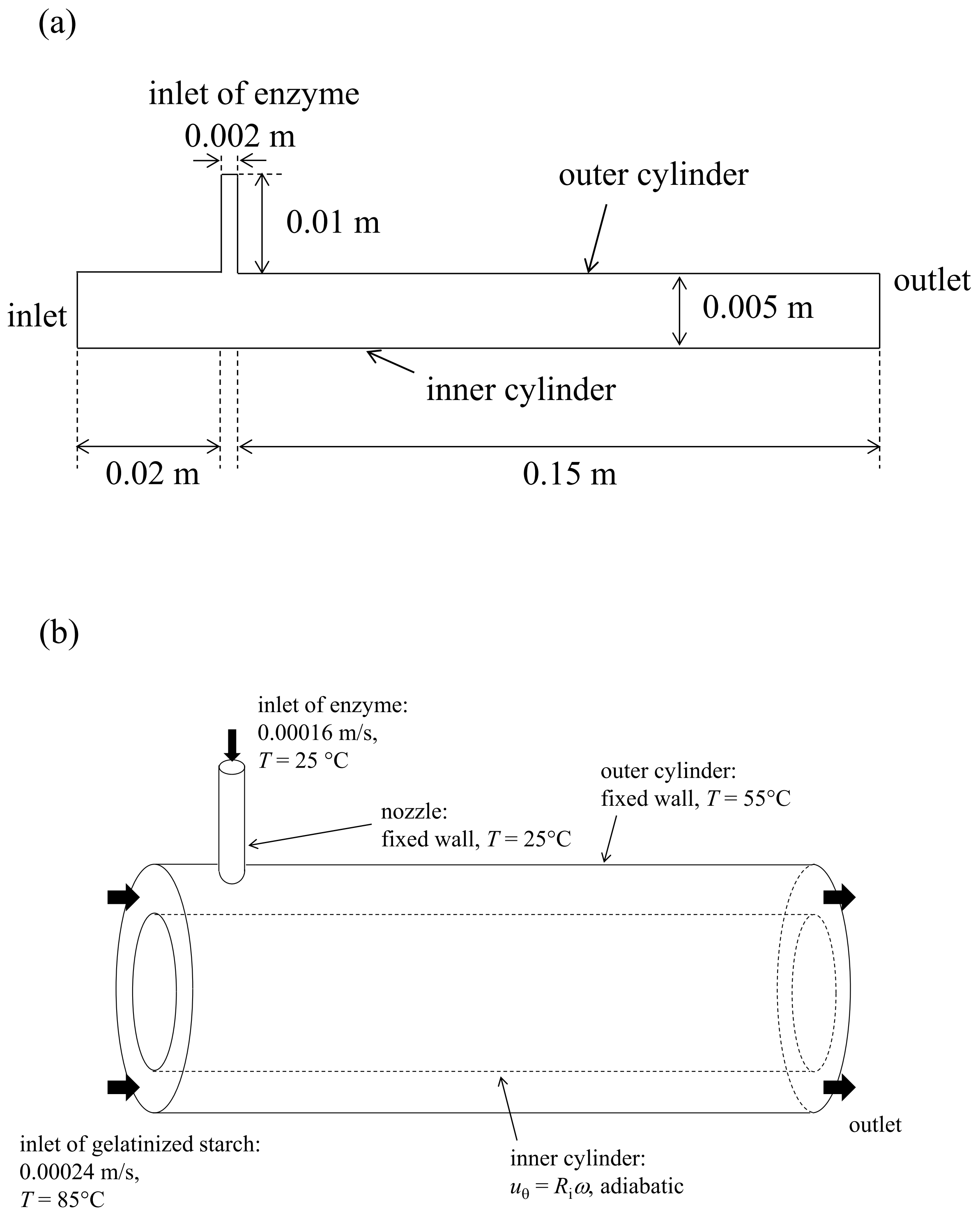

Fig. 3–5 Computational geometry: (a) cross sectional view and (b) three dimensional view

3. 3. Results and discussion

3. 3. 1. Gelatinization

The starch gelatinization kinetics is often represented as a first order reaction kinetic (Zanoni *et al.*, 1995; Gomi *et al.*, 1998):

$$\text{Starch suspension} \xrightarrow{+\text{ Heat}} \text{Gelatinized starch}$$

$$r_{\mathrm{ge}} = k_{\mathrm{ge}} \exp\left(-\frac{E_{\mathrm{ge}}}{RT_{\mathrm{ge}}} \right) C \tag{3–6}$$

where r_{ge} is the rate of starch gelatinization, C is ungelatinized starch concentration, k_{ge} is the reaction rate constant, R is gas constant, T_{ge} is reaction temperature and E_{ge} is activation energy. Because of high E_{ge} (108.3 kJ/mol, Brandam *et al.*, 2003), starch gelatinization rate is strongly affected by temperature. This means heat transfer from the wall to the fluid is important. The heat transfer in a radial direction can be enhanced by rotation of the inner cylinder (e.g. Kataoka, 1975).

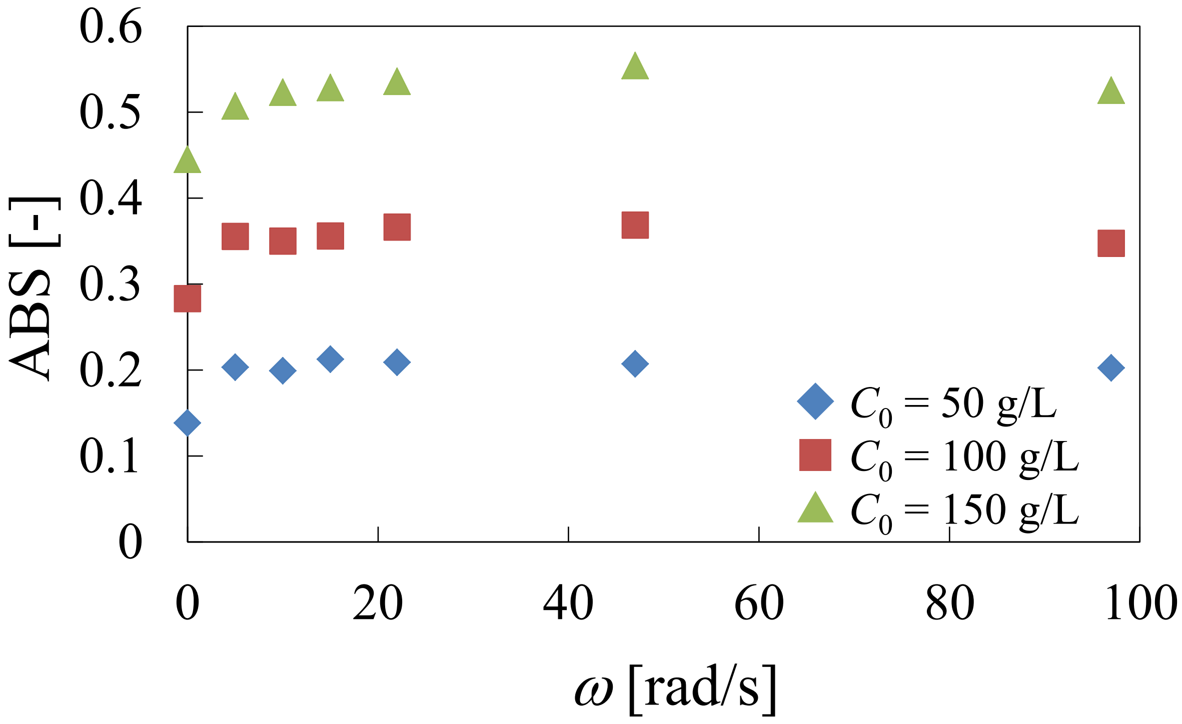

Fig. 3−6 Light absorbance in the effluent at various initial concentrations of starch, suspension and rotational speeds of the inner cylinder

Figure 3−6 shows the light absorbance (ABS) at various rotation speeds of the inner cylinder (ω) with the Couette-Taylor flow reactor. Strictly speaking, the values of ABS cannot directly indicate the degree of gelatinization, because they indicate the degree of structure change after gelatinization. However, as a high value of ABS implies high complexity of starch structure after gelatinization, it can be considered that the higher degree of starch gelatinization is obtained when higher value of ABS. This result indicates that there was much ungelatinized starch with no rotation of the inner cylinder in all cases of C_0. The degree of gelatinization dramatically increases by the rotation of the inner cylinder. According to Hubacz *et al.* (2010), at least in the first inlet part of the apparatus, the rotation of the inner cylinder causes a presence of Taylor vortices and these vortices considerably promote heat transfer. When Taylor vortices are formed, the temperature inside of the apparatus achieves quickly the value of the heat jacket temperature (T_{ge}). Furthermore, the increasing of rotation of the inner cylinder causes lengthening of the zone where Taylor vortices exist (Hubacz and Buczyńska, 2011).

As shown in **Fig. 3–7**, in the case of C_0 = 50 g/L, the temperature finally reached the identical value at L = 0.25 m. However, Hubacz *et al.* (2013) experimentally and numerically reported that the temperature in the vicinity of the inlet of the apparatus became lower without rotation compared with cases of rotation. It is inferred that there is significant temperature gradient in a radial direction around the inlet. The gradient causes the distribution of the degree of gelatinization in the radial direction. The uniform heating of starch/water suspension is one of the most important factors for gelatinization. This means that the mixing in the initial stage is crucial for final gelatinization state. It is, therefore, considered that the ununiformity of degree of gelatinization due to poor mixing in the vicinity of the inlet port resulted into low gelatinization at the outlet port in the case without rotation of the inner cylinder. Sakonidou *et al.* (2003) pointed out that in the absence of an appropriate low-shear agitation to promote gentle mixing of every part of the starch/water suspension and also transfer heat throughout the entire sample mass, there are sections in the test vessel where gelatinization is greatly retarded. Therefore, in order to achieve the sufficient degree of gelatinization, mixing by rotation of the inner cylinder was necessary even at high temperature.

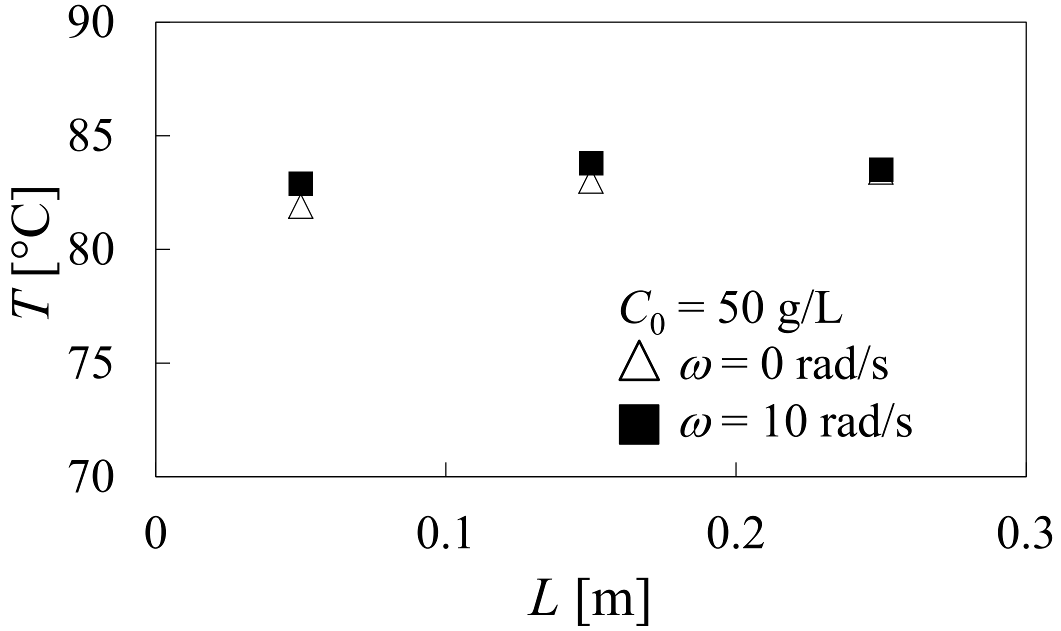

Fig. 3–7 Temperature distribution along the length of apparatus at C_0 = 50 g/L

3. 3. 2. Saccharification

Figure 3–8 shows the dependence of the rotation speed on the product concentration, reducing sugar C_{rs}, obtained from the outlet of the TCFR. The saccharification temperature was varied by controlling the water jacket temperature of the saccharification section. Comparing the case of ω = 0 rad/s with the others, it is found that the rotation of the inner cylinder intensified heat transfer and mixing with enzyme in saccharification as well as in gelatinization. At T_{sa} = 35 and 55°C, since the concentration of reducing sugar obtained at around ω = 10 rad/s was slightly higher than

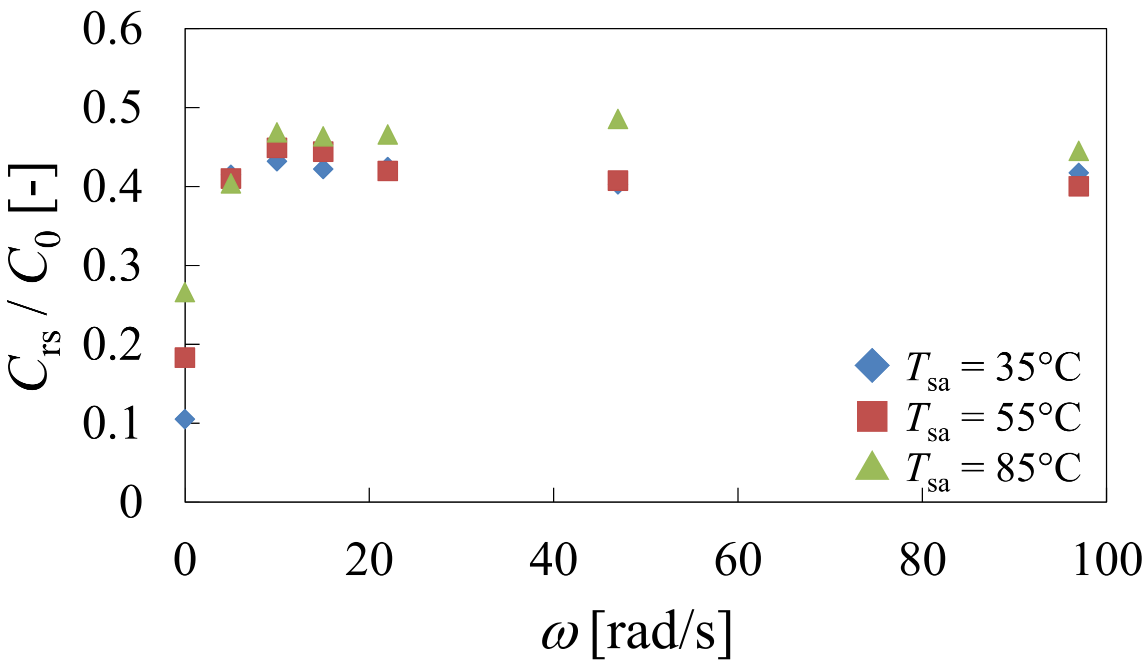

Fig. 3–8 Concentration of reducing sugar produced at various rotational speeds and saccharification temperature at C_0 = 50 g/L, u = 0.00024m/s, v_e = 0.3 mL/h

the others. It is assumed that this region corresponds to a laminar Taylor vortex flow formation. Not only mixing within vortex cell but also axial dispersion are enhanced with increasing of ω. In the case of C_0 = 50 g/L, mixing enhancement was enough at the low rotation speed (more than the critical rotation speed for the generation of Taylor vortices) because of the lower viscosity in the saccharification section. However, the effect of axial dispersion is also enhanced with the increase of rotation speed. Therefore, it is considered that the critical rotation speed was the advantageous operational condition within the performed measurements for C_0 = 50 g/L. While the effect of temperature was dominant for the gelatinization, but not for the saccharification, it is more important for saccharification to mix with the gelatinized starch and enzyme. However, for the case of 85°C, the gelatinization occurred simultaneously in the second half part of the apparatus, and the saccharification degree was slightly improved in the high rotation speed region in **Fig. 3–8**. As for the case of without rotation, the higher temperature gave a higher reducing sugar concentration. Since there is residual ungelatinized starch present, the gelatinization and saccharification occurred simultaneously in the saccharification section. Therefore, the higher reducing sugar concentration was obtained at the higher temperature.

As shown in **Figs. 3–9** and **3–10**, when the initial concentration of starch was 100 and 150 g/L, unlike the gelatinization experiment, the concentration of reducing sugar increased with the rotation speed of the inner cylinder and the temperature increase of the saccharification section. When the gelatinization occurred at the higher concentration, much starch was left ungelatinized. At T_{sa} =35°C, gelatinization does not occur in the saccharification section, but starch retrogradation proceeds. As a result, although the increasing of ω was effective, the C_{rs} / C_0 was totally lower than the other cases. At T_{sa} = 55 and 85°C, starch retrogradation does not proceed. Meanwhile, gelatinization and saccharification occurs simultaneously in the saccharification section at T_{sa} = 85°C. As a result, C_{rs} / C_0 became higher than at T_{sa} = 55°C. In other words, more ungelatinized starch remained at lower T_{sa}. Therefore, a higher temperature showed better performance than the lower temperature since the gelatinization simultaneously occurred in the saccharification section.

Figures 3–9 and **3–10** also indicate a dependence of the rotation speed of the inner cylinder. At lower ω region ($\omega \leq 22$ rad/s), C_{rs} / C_0 greatly increased with the increasing of ω. On the other hand, at higher ω region ($\omega \geq 22$ rad/s), C_{rs} / C_0 slightly increased or almost kept a constant with the increasing of ω. Comparing **Figs. 3– 8–10**, it is found that these critical values of the rotation speed of the inner cylinder existed in all cases of C_0. In saccharification section, it is assumed that Taylor vortex was formed above the critical rotation speed of the inner cylinder and intensified not only heat transfer but also mixing with the enzyme.

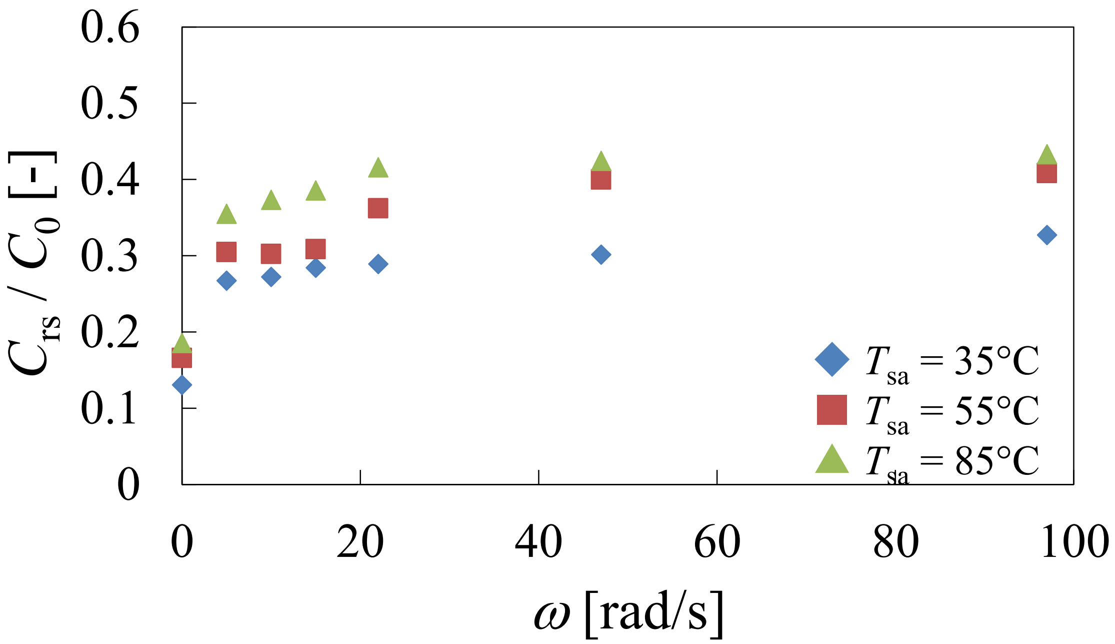

Fig. 3–9 Concentration of reducing sugar produced at various rotational speeds and saccharification temperature at C_0 = 100 g/L, u = 0.00024m/s, v_e = 0.3 mL/h

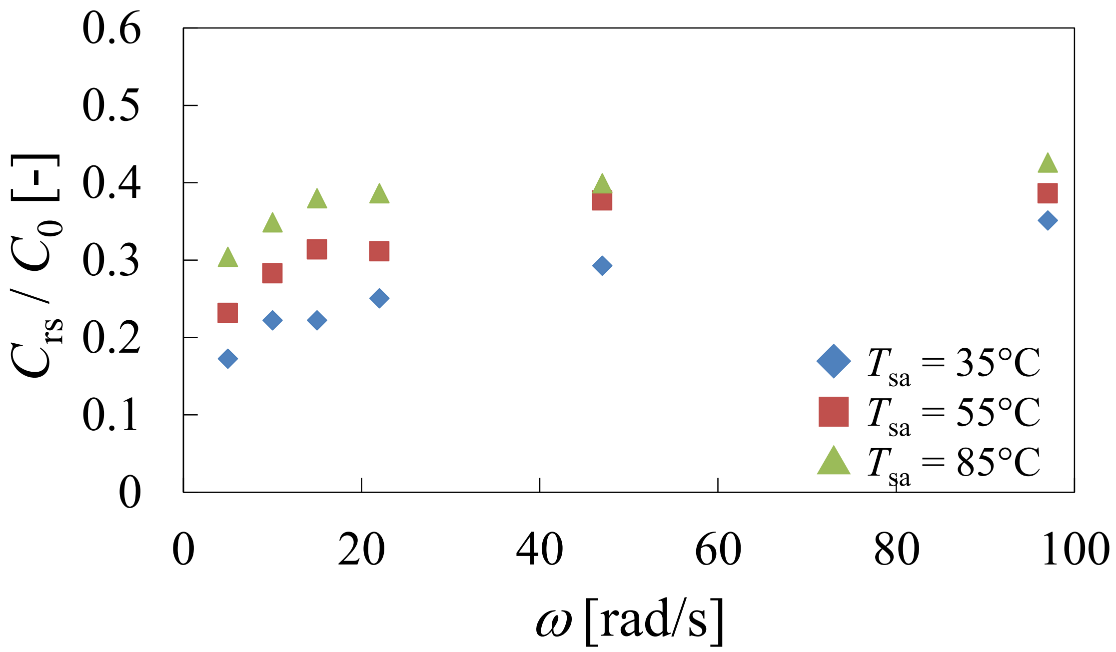

Fig. 3–10 Concentration of reducing sugar produced at various rotational speeds and saccharification temperature at C_0 = 150 g/L, u = 0.00024m/s, v_e = 0.3 mL/h

3. 3. 3. Effect of Reynolds number

The effective Reynolds number, Re_{eff}, as shown in Eq. (3−7), is used as the dimensionless parameter for the rotating flow with shear-thinning fluids.

$$Re_{\mathrm{eff}} = \frac{\rho R_{\mathrm{i}} \omega d}{\eta_{\mathrm{eff}}} \tag{3–7}$$

The formation of counter-rotating toroidal vortices starts when Re_{eff} exceeds a critical Reynolds number, Re_{cr}. Here, in order to calculate Re_{eff}, the proposed method in Chapter 2 of this thesis was used. The theoretical value of Re_{cr} for this radius ratio $R_{\mathrm{i}}/R_{\mathrm{o}} = 0.71$ is approximately $Re_{\mathrm{cr}} = 81.1$ given by the linearized theory (e.g. Di Prima and Swinney, 1981). In the laminar Taylor vortex flow region, intermixing over cell boundaries is suppressed. Furthermore, Kataoka *et al.* (1995) experimentally showed the flow transits from the laminar Taylor vortex flow to the wavy vortex flow at $Re = 791$ for Newtonian fluid system. Upon transition to the wavy vortex flow, wavy motions increase not only the inside mixing but also the intermixing. In this study, since the degree of gelatinization was almost independent of ω except for low rotation speed under this residence time as shown in **Fig. 3–6**, the effect of Taylor vortex flow with respect to its mixing characteristics can be limited to the saccharification section.

For the calculation of Re_{eff}, the effective viscosity, η_{eff}, is required for the shear-thinning property. The viscosity profiles of the effluent are characterized by the Carreau model (Carreau, 1972). The variation in apparent viscosity as a function of shear-rate is shown in **Fig. 3–11**, in the case of $C_0 = 150$ g/L, $\omega = 22$ rad/s, $T_{\mathrm{sa}} = 85$°C.

Also, the Carreau model line is drawn in **Fig. 3–11**. From the radius ratio (R_i / R_o), and the rheological properties of the effluent (n), the proportional constant, k, in Eq. (2–15) in Chapter 2 can be calculated. This leads to the estimation of the effective shear-rate at the given rotational speed of the inner cylinder. As a result, η_{eff} and Re_{eff} each condition can be calculated. In the case of C_0 = 50 and 150 g/L, the effective viscosity of the effluent, and Re_{eff} at T_{sa} = 85°C and various ω are given in **Table 3–3**. Here, the density was measured using a pycnometer. Its value was 1005 kg/m^3 for C_0 = 50 g/L, and 1088 kg/m^3 for C_0 = 150 g/L.

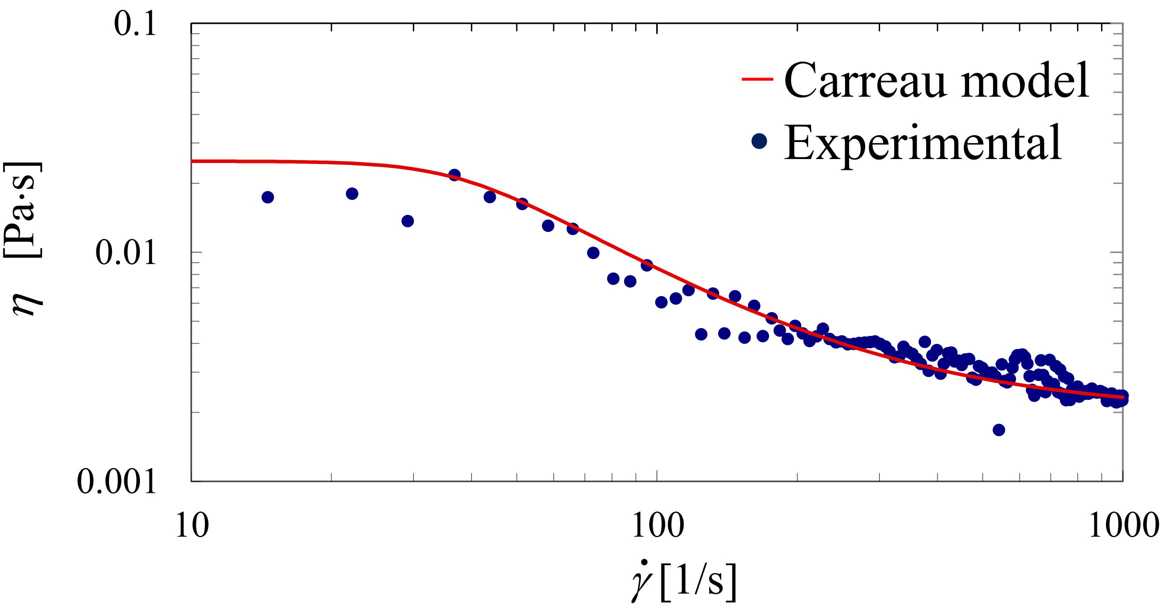

Fig. 3–11 Rheological properties of reducing sugar at C_0 = 150 g/L, u = 0.00024 m/s, ω = 22 rad/s, T_{sa} = 85°C

Table 3–3 Effective viscosity of the effluent and Re_{eff} at various ω (a) C_0 = 50 g/L and (b) C_0 = 150 g/L

(a) C_0 = 50 g/L

ω [rad/s]	2	5	10	15	22
η_{eff} [Pa·s]	9.2×10^{-3}	7.8×10^{-3}	7.1×10^{-3}	7.1×10^{-3}	6.8×10^{-3}
Re_{eff} [–]	13.6	40.3	88.5	132.7	203.6

(b) C_0 = 150 g/L

ω [rad/s]	5	10	15	22	47
η_{eff} [Pa·s]	4.5×10^{-2}	3.0×10^{-2}	2.2×10^{-2}	1.6×10^{-2}	5.3×10^{-3}
Re_{eff} [–]	7.6	22.9	45.7	96.3	607.0

Figure 3–12 and **3–13** shows the relation between Re_{eff} and C_{rs}/C_0 at C_0 = 50 and 150 g/L. As expected in the previous section, it became clear that Taylor vortex forms in the saccharification section near the rotation speed of the inner cylinder where C_{rs}/C_0 starts keeping a nearly constant with the increasing of ω. Actually, as shown in **Fig. 3–12**, it could be confirmed that there appeared Taylor vortices for C_0 = 50 g/L at ω = 10rad/s. In the two cases, C_{rs}/C_0 monotonically increased with the increasing of Re_{eff} up to Re_{cr}. As shown in **Fig. 3–12** and **3–13**, C_{rs}/C_0 kept a constant or slightly increased over Re_{cr}.

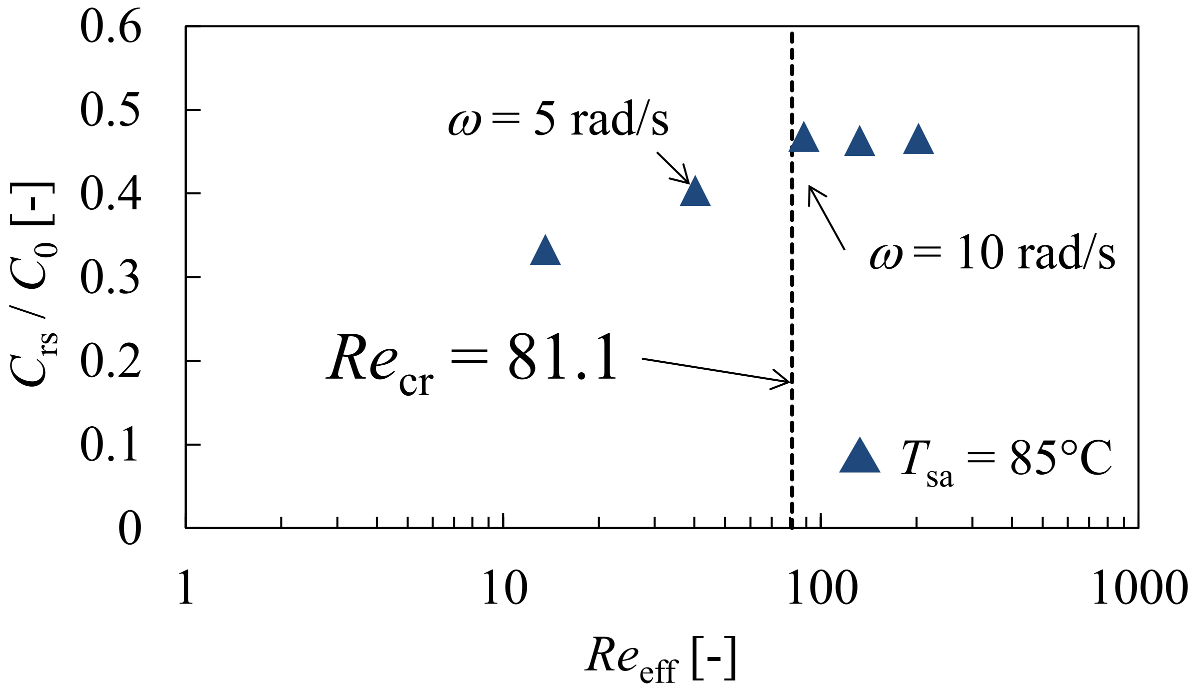

Fig. 3−12 Relation between concentration of reducing sugar and Re_{eff} at C_0 = 50 g/L, u = 0.00024 m/s, T_{sa} = 85°C

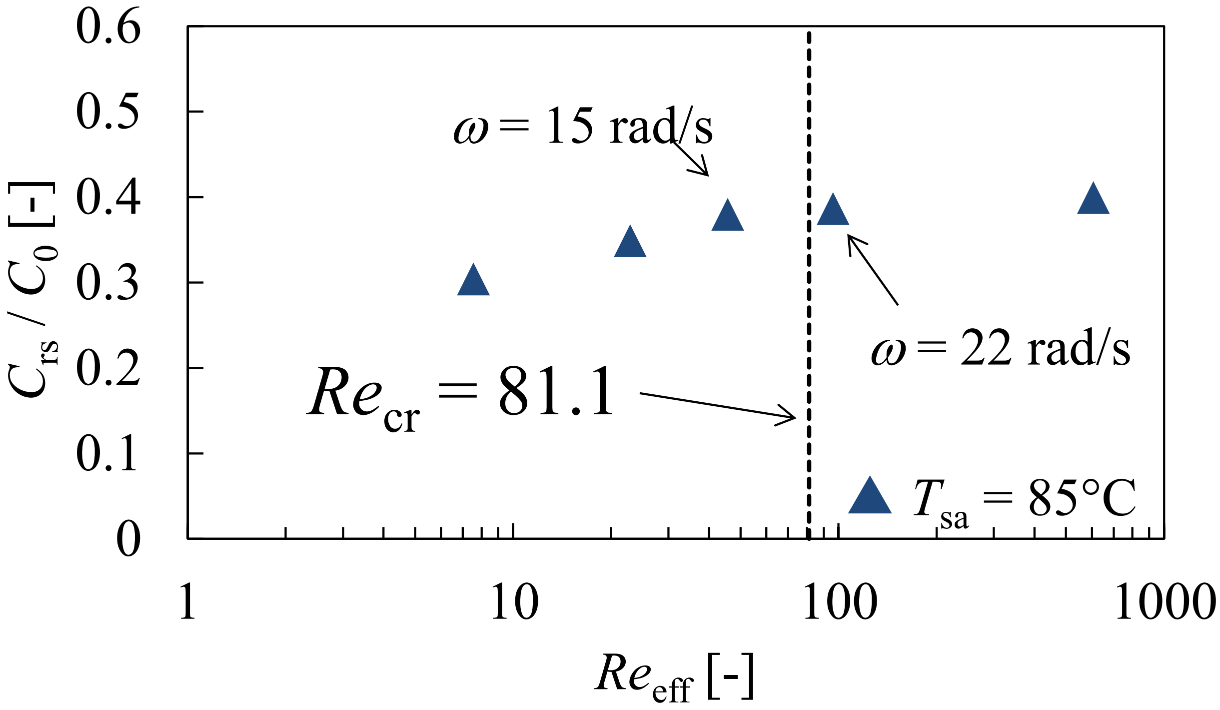

Fig. 3−13 Relation between concentration of reducing sugar and Re_{eff} at C_0 = 150 g/L, u = 0.00024 m/s, T_{sa} = 85°C

Furthermore, the performance of TCFR for a high concentration system at a wide range of Re_{eff} was investigated. **Figure 3–14** shows the dependency of C_{rs}/C_0 on Re_{eff} at C_0 = 50 – 300 g/L and T_{sa} = 40°C. The enzyme-to-substrate ratio was unified as $C_0 : v_e = 1 : 0.006$.

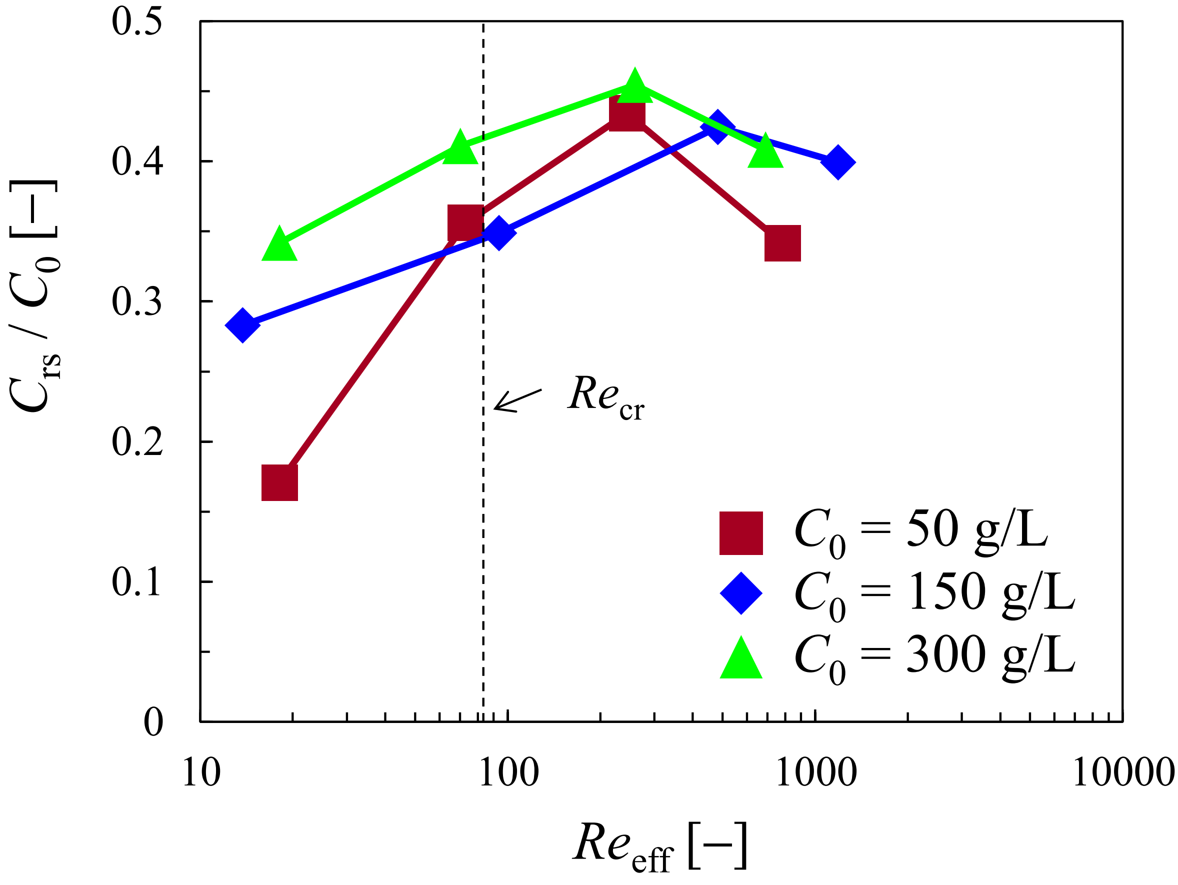

Fig. 3–14 Relation between concentration of reducing sugar and Re_{eff} at C_0 = 50, 150, 300 g/L, u = 0.00024 m/s, T_{sa} = 40°C

As shown in **Fig. 3–14**, even the high concentration starch suspension was effectively and continuously hydrolyzed at Taylor vortex flow region. However, the C_{rs}/C_0 slightly decreased at higher Re_{eff}, above $Re_{eff} = 700$. In this region, wavy instability may be occurred. As discussed above, this can be expected by the effect of enhancement of axial dispersion. This result suggests that, in order to make the best use of the mixing characteristics of the Taylor vortex flow reactor and suppressing axial dispersion, the reactor should be operated in the laminar Taylor vortex flow region. Further, the solid line in **Fig. 3–14** denotes C_{rs}/C_0 obtained for $C_0 = 50$ g/L using a stirred tank reactor with a Rushton turbine. Here, the volume of starch suspension and enzyme, reaction temperature, and reaction time corresponded to the case with the TCFR. The rotational speed of the impeller was set at 350 rpm. It was assumed that this rotational speed is sufficient for the achievement of the state of complete mixing. As shown in **Fig. 3–14**, C_{rs}/C_0 obtained using the TCFR under the laminar Taylor vortex flow region is even equal to C_{rs}/ C_0 obtained using the stirred tank reactor.

Figure 3–15 shows the distribution of enzyme fraction, which was obtained by numerical simulation, at (a) $Re_{eff} = 18$ and (b) $Re_{eff} = 226$. When the enzyme, which is introduced from the upper nozzle, contacts the gelatinized surface at the interface, saccharification will start. At low Re_{eff}, in Couette flow region, the enzyme could not diffuse towards the inner cylinder surface. On the other hand, if there appear Taylor vortices, the enzyme easily diffused in the radial direction. Therefore, due to the enhancement of mixing by Taylor vortices, the saccharification was promoted even at the high concentration of starch suspension.

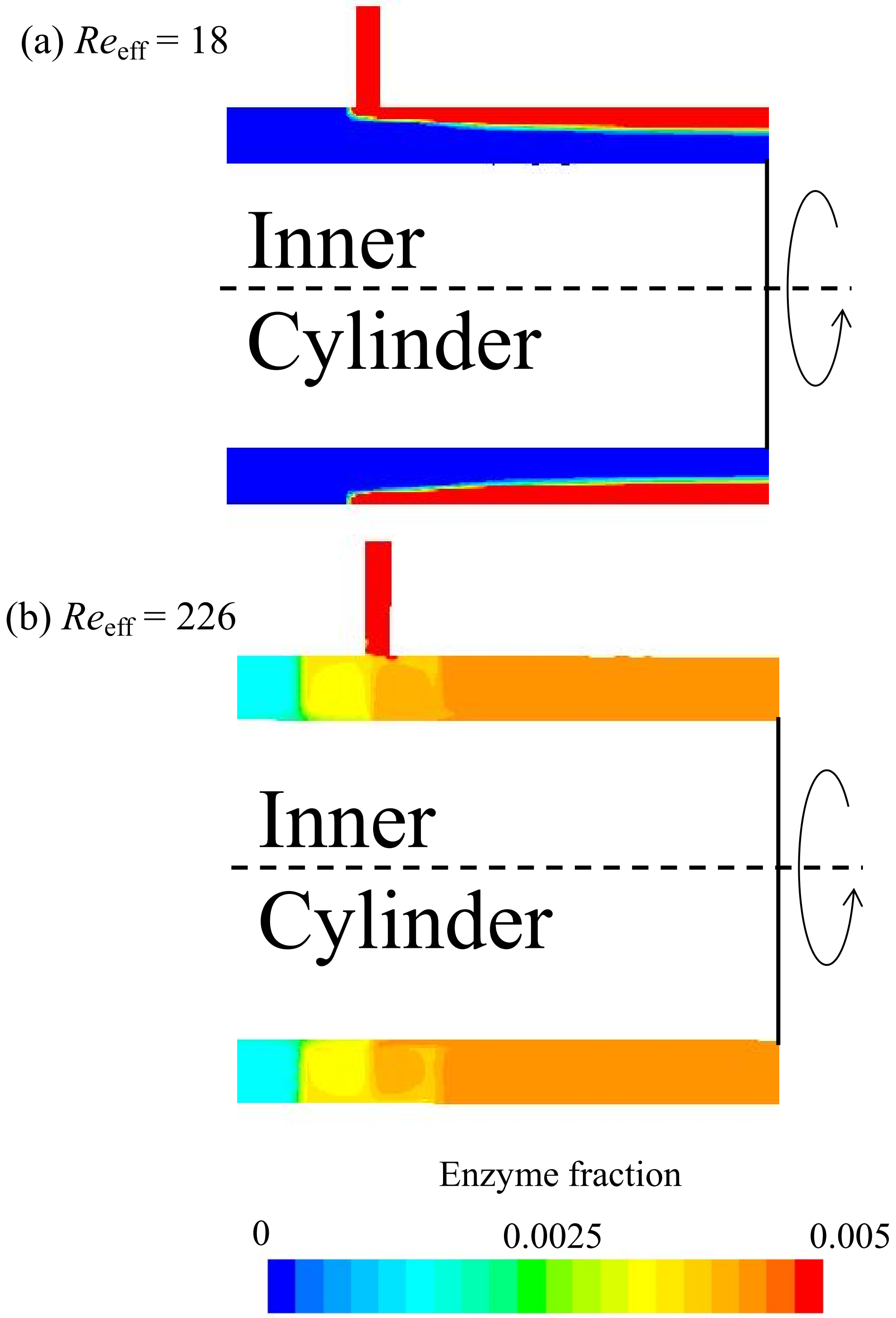

Fig. 3–15 Volume fraction of enzyme (a) $Re_{\mathrm{eff}} = 18$ and (b) $Re_{\mathrm{eff}} = 226$ at $C_0 = 300$ g/L

3. 4. Conclusions

The present study in this chapter discussed the process intensification of starch gelatinization and saccharification by converting a batch to continuous operation using the TCFR with a water jacket.

The rotation of the inner cylinder played an important role for the initial stage of gelatinization because of enhancement of heat transfer and mixing by cellular vortex motion. However, the results show that the degree of gelatinization was almost independent of the rotation speed of the inner cylinder above 5 rad/s, due to the sufficient by long residence time. Saccharification experiments and simulations show that the product concentration increased with a higher rotation speed of the inner cylinder, up to the formation of Taylor vortex flow in the saccharification section. And C_{rs}/C_0 stayed a constant or slightly increased over the Re_{cr} for 50 or 150 g/L, respectively. However, above $Re_{\mathrm{eff}} = 700$, C_{rs}/C_0 slightly decreased. It is assumed that the axial dispersion was promoted at higher Re_{eff}. The effect of temperature on C_{rs}/C_0 could not be observed for the case of 50 g/L starch concentration, but it appeared when the initial concentration was 100 and 150 g/L. This is because a portion of the starch was left ungelatinized in the gelatinization section and simultaneously gelatinized in the saccharification section.

The TCFR enabled one-step continuous starch hydrolysis process even in the case of high concentration of starch suspension. In order to optimize the starch hydrolysis using the TCFR, the further investigation about the axial dispersion at high Re_{eff} is necessary.

Nomenclature

C : concentration of ungelatinized starch, g/L

C_0 : initial concentration of starch suspension, g/L

C_p : specific heat capacity, J/kg·K

C_{rs} : concentration of reducing sugar, g/L

$\boldsymbol{D}$: deformation rate tensor, 1/s

D_j : diffusion coefficient of the species j, m^2/s

d : gap width, m

E_{ge} : activation energy for starch granules gelatinization, kJ/mol

g : gravity acceleration (= 9.8 m/s^2), m/s^2

j : species, -

k : proportional constant, -

k_{ge} : pre-exponential factor for starch granules gelatinization, 1/s

L : length of TCFR, m

n : power index, -

p : pressure, Pa

R : gas constant (= 8.31 J/K·mol), J/K·mol

r : radial position, m

r_{ge} : gelatinization rate, kg/L·s

Re : Reynolds number ($= \rho R_i \omega d / \eta$), -

Re_{cr} : critical Reynolds number, -

Re_{eff} : effective Reynolds number ($= \rho R_i \omega d / \eta_{eff}$), -

R_i : inner cylinder radius, m

R_o : outer cylinder radius, m

T : temperature inside of TCFR, K

T_{in} : inlet temperature, K

T_{ge} : temperature of gelatinization process, °C

T_{sa} : temperature of saccharification process, °C

t : time, s

u_{ax} : inlet axial velocity of starch slurries, m/s

u_e : inlet axial velocity of enzyme, m/s

u_θ : circumferential velocity, m/s

$\boldsymbol{u}$: velocity, m/s

v_e : enzymatic volumetric flow rate, mL/h

X_j : mass fraction of the species j, -

Greek letters

β : characteristic time, s

$\dot{\gamma}$: shear-rate, 1/s

λ : thermal conductivity, W/m·K

η : fluid viscosity, Pa·s

η_0 : zero shear-rate viscosity, Pa·s

η_∞ : infinite shear-rate viscosity, Pa·s

η_{eff} : effective viscosity, Pa·s

ρ : fluid density, kg/m^3

ω : angular velocity of inner cylinder, rad/s

References

T. Baks, F. H. J. Kappen, A. E. M. Janssen, R. M. Boom, Towards an optimal process for gelatinization and hydrolysis of highly concentrated starch–water mixtures with alpha-amylase from B. licheniformis, *J. Cereal. Sci.*, **47**, 214–225 (2008)

C. Brandam, X. M. Meyer, J. Proth, P. Strehaiano, H. Pingaud, An original kinetic model for the enzymatic hydrolysis of starch during meshing, *Biochem. Eng. J.*, **13**, 43–52 (2003)

P. J. Carreau, Rheological equation s from molecular network theories, *Trans. Soc. Rheol.*, **16**, 99–127 (1972)

R. C. Di Prima, H. L. Swinney, Instabilities and transition in flow between concentric rotating cylinders, in: *Hydrodynamic Instabilities and the transition to Turbulence*, Springer-Verlag, 139–180 (1981)

M. A. Emin, H. P. Schuchmann, Analysis of the dispersive mixing efficiency in a twin-screw extrusion processing of starch based matrix, *J. Food Eng.*, **115**, 132–143 (2013)

Y. Gomi, M. Fukuoka, T. Mihori, H. Watanabe, The rate of starch gelatinization as observed by PFG-NMR measurement of water diffusivity in rice starch/water mixtures, *J. Food Eng.*, **36**, 359–369 (1998)

R. Hubacz, N. Ohmura, S. Wroński, Starch gelatinization and hydrolysis in the apparatus with Couette-Taylor flow, *Inż. Apar. Chem.*, **49**, 55–56 (2010)

R. Hubacz, M. Buczyńska, Starch gelatinization in Couette-Taylor flow Apparatus, *Chem. Proc. Eng.*, **32**, 267–279 (2011)

R. Hubacz, N. Ohmura, E. Dluska, Intensification of processing using apparatus with

Couette−Taylor flow, *J. Food Process Eng.*, **36**, 774−785 (2013)

W. M. Jung, S. H. Kang, W. S. Kim, C. K. Choi, Particle morphology of calcium carbonate precipitated by gas-liquid reaction in a Couette-Taylor reactor, *Chem. Eng. Sci.*, **55**, 733−747 (2000)

K. Kataoka, Heat-transfer in a Taylor vortex flow, *J. Chem. Eng. Japan*, **8**, 271−276 (1975)

K. Kataoka, H. Doi, T. Hongo, M. Futagawa, Ideal plug-flow properties of Taylor vortex flow, *J. Chem. Eng. Japan*, **8**, 472−476 (1975)

K. Kataoka, N. Ohmura, M. Kouzu, Y. Simamura, M. Okubo, Emulsion polymerization of styrene in a continuous Taylor vortex flow reactor, *Chem. Eng. Sci.*, **50**, 1409−1416 (1995)

J. D. H. Kelder, K. J. Ptaniski, P. J. A. M. Kerkhof, Starch gelatinization in coiled heaters, *Biotechnol. Prog.*, **20**, 921−929 (2004)

V. Komolprasert, R. Y. Ofoli, Starch hydrolysis kinetics of *Bacillus licheniformi*s α-amylase, *J. Chem. Tech. Biotechnol.*, **51**, 209−223 (1991)

S. Lee, R. M. Lueqtow, Rotating reverse osmosis: a dynamic model for flux and rejection, *J. Memb. Sci.*, **192**, 129−143 (2001)

D. Paolucci-Jeanjean, M. P. Belleville, G. M. Rios, N. Zakhia, Kinetics of continuous starch hydrolysis in a membrane reactor, *Biochem. Eng. J.*, **6**, 233−238 (2000)

P. Pineda-Gómez, A. Rosales-Rivera, M. E. Rodríguez-García, Modeling calcium and water intake in threshed corn grain during thermo-alkaline treatment, *J. Food Eng.*, **113**, 434−441 (2012)

P. Reinikaine, T. Suortti, J. Olkku, Mälkki, P. Linko, Extrusion cooking in enzymatic liquefaction of wheat starch, *starch/stärke*, **38**, 20−26 (1986)

E. P. Sakonidou, T. D. Karapantsios, S. N. Raphaelides, Mass transfer limitations during starch gelatinization, *Carbohydr. Polym.*, **53**, 53–61 (2003)

J. G. Sczechowski, C. A. Koval, R. D. Noble, A Taylor vortex reactor for heterogeneous photocatalysis, *Chem. Eng. Sci.*, **50**, 3163–3173 (1995)

G. I. Taylor, Stability of a viscous liquid contained between two rotating cylinders, *Phil. Trans. Roy. Soc. A*, **223**, 289–343 (1923)

B. Zanoni, A. Schiraldi, J. Simonetta, A naive model of starch gelatinization kinetics, *J. Food Eng.*, **24**, 25–33 (1995)

4. Gas–liquid two-phase Taylor–Couette flow with a ribbed inner cylinder

4. 1. Introduction

In this chapter, intensification of gas–liquid two-phase flow process was discussed. As described in Chapter 1, TCFR is suitable for bio-process or food process, in which shear sensitive materials are treated, because it has a mild but effective mixing performance compared to classical stirred tank reactors (Wroński *et al.*, 2005). In such processes, an aeration operation is frequently required for the microbial growth. In fact, TCFR has been applied to bio-process with the aeration by many researchers (Haut *et al.*, 2003; Kliphuis *et al.*, 2010; Patel *et al.*, 2010; Zhu *et al.*, 2010; Song *et al.*, 2011; Kong *et al.*, 2013; Kong and Vigil, 2013; Qiao *et al.*, 2014). In order to design and optimize TCFR, the understanding of interphase mass transfer is necessary. For gas–liquid systems, it is usually assumed that the liquid side mass transfer resistance at gas–liquid interfaces limits interphase mass transport, and therefore gas side mass transfer is neglected (Deckwer *et al.*, 1974). Several correlations between the liquid side volumetric mass transfer coefficient (k_La) and operational conditions were proposed (Wroński *et al.*, 1999; Dłuska *et al.*, 2001; Dłuska *et al.*, 2004; Gao *et al.*, 2015; Ramezani *et al.*, 2015). From the aspect of process intensification, higher gas hold–up and higher dispersion of gas phase are necessary so as to enhance mass transfer volumetric coefficients (k_La) between two-phases. However, it is difficult to estimate k_La because of the many factors affecting this quantity, such as gas hold–up, bubble size and slip velocity (Gao *et al.*, 2015). These factors depend on the operational condition and physical properties of the gas and liquid phases, as shown in **Fig. 4–1**. In order to intensify mass transfer between gas and liquid phase, at least one of "k_L" and "a" should be intensified. This objective of this chapter aimed at the intensification of specific gas–liquid interfacial area, *a*.

It is well known that the introduction of even a small amount of gas significantly impacts flow patterns of Taylo–Couette flow (Shiomi *et al.* 1993; Djéridi *et al.*, 1999; Hubacz and Wroński, 2004; Maryami *et al.*, 2014). Under lower rotational Reynolds number (*Re*) condition, owing to weak centrifugal force compared with the buoyancy force acting on bubbles, Taylor vortices are easily disrupted, and the bubbles are dispersed uniformly and quickly rise up. This bubbly flow causes a problem of lower gas hold–up. At higher *Re*, bubbles are captured within Taylor vortices and accumulate near the inner cylinder surface at the outflow boundaries of the Taylor vortices (Atkhen *et al.*, 2000; Djeridi *et al.*, 2004; Murai *et al.*, 2005; Deng *et al.*, 2006, Climent *et al.*, 2007; Fokoua *et al.*, 2015). Although higher rotation speed of the inner cylinder might be one of the solutions for this problem, high shear stress due to high rotation speed is not preferable for shear sensitive materials. In order to maintain a vortex structure and to avoid damage to shear sensitive materials, a new strategy is required for development of TCFR applicable to bio-processes or food process.

The vortex formation could be affected by the boundary conditions, e.g., asymmetric boundary conditions (Mullin and Blohm, 2001), short annulus (Ikeda and Maxworthy, 1994; Furukawa *et al.*, 2002), ribbed wall cylinder (Tzeng *et al.*, 2005), internal baffles (Deng *et al.*, 2010), modified cylinder (Li *et al.*, 2015), and conical cylinder (Noui-Mehidi *et al.*, 2005). Recently, Richter *et al.* (2008, 2009) proposed a TCFR with a novel ribbed cylinder and investigated mixing in the reactor by means of the tracer technique and a chemical test reaction. They successfully showed the results for a single phase flow that immobilized and stable vortices were obtained even with axial flows and that micromixing was clearly enhanced while axial dispersion could be simultaneously reduced.

In this chapter, it was investigated that the applicability of the TCFR with a ribbed inner cylinder to gas–liquid two-phase flow to increase gas hold–up by immobilizing and stabilizing the vortices. Therefore, the characteristics of gas–liquid two-phase flow in the TCFR with the ribbed cylinder were experimentally observed. Finally, the performance of the TCFR with ribs was evaluated by specific gas–liquid interfacial area and gas hold–up.

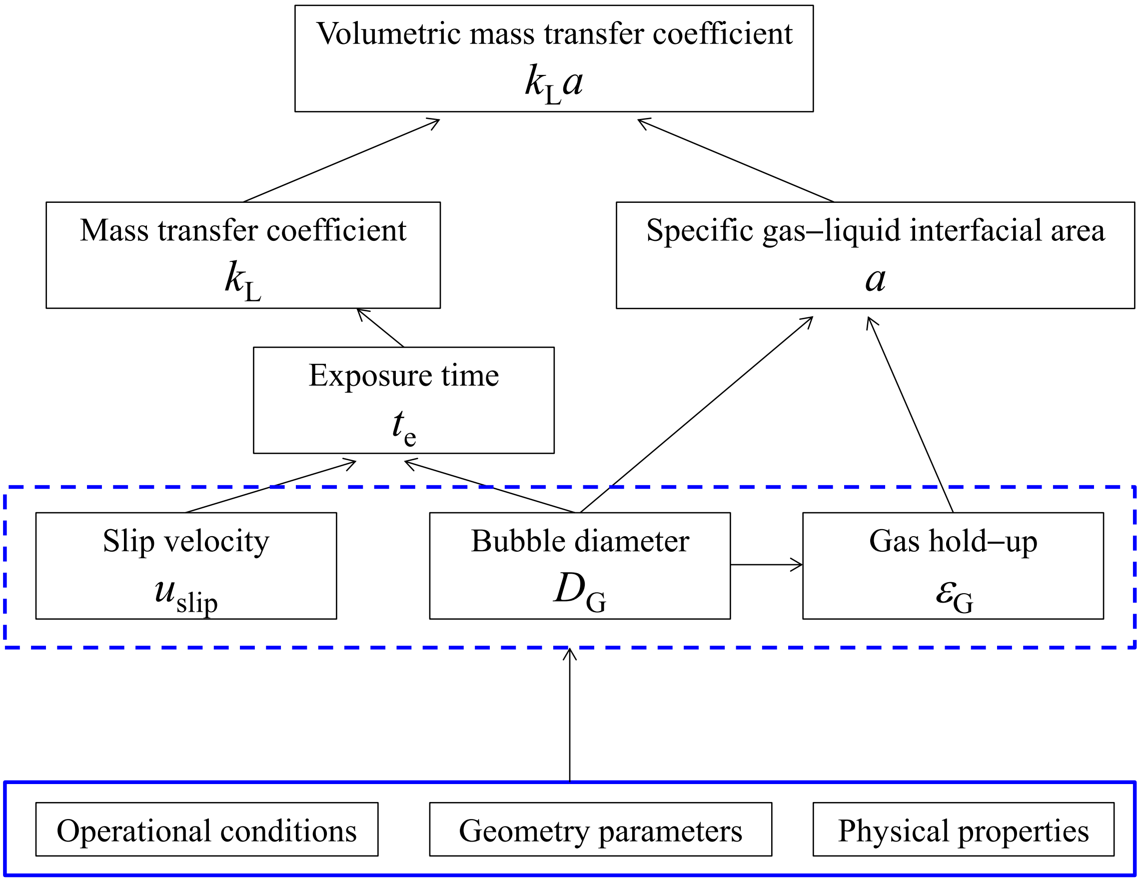

Fig. 4–1 Illustration of the relationships between volumetric mass transfer coefficient and various geometric, operational, and hydrodynamic parameters, quoted from the paper by Gao *et al*. (2015)

4. 2. Experimental

The schematic of vertical CTFR with ribs is shown in **Fig. 4–2**. The distance between two ribs, h_{cell}, was set at 26 mm, which is the same as the theoretical axial wavelength λ (= $2d$). The width of ribs, r_{rib}, was varied from 4 to 10 mm, while the thickness of ribs, h_{rib}, kept a constant value of 4 mm. The experimental apparatus with measuring system is shown in **Fig. 4–3**. The apparatus consisted of an outer cylinder of transparent acrylic resin and an inner cylinder of stainless steel. The outer diameter of the inner cylinder, D_{i} (= $2R_{\mathrm{i}}$), was 50 mm and the inside diameter of the outer cylinder, D_{o} (= $2R_{\mathrm{o}}$), was 76 mm. The radius ration, $R_{\mathrm{i}} / R_{\mathrm{o}}$, was 0.66. For this ratio, Re_{cr} where the first instability occurs is about 78.3 (Taylor, 1923). The height of the annular space, h, was 300 mm and that of liquid phase without aeration, h_0, was 270 mm. An aqueous solution of glycerol was used as the working fluid. The density and viscosity of the working fluid were $\rho = 1150$ kg/m^3 and $\eta = 8.14\times10^{-3}$ Pa·s, respectively.

In order to generate uniform bubbles with diameters of 1–1.5 mm, a compressor drove air through a sparger from the bottom of the apparatus. The liquid was opened to the atmosphere to release bubbles on the free surface. The volumetric flow rate of gas, V_{G}, was controlled by a needle valve and set at 5.0×10^{-7}–5.0×10^{-6} m^3/s. The rotational speed of the rotor, n, was varied from 150 to 300 rpm. As a result, Re, is defined as $Re = \omega\rho R_{\mathrm{i}}d / \mu$, was varied from 721.2 to 1442.5. Here, ω is defined as $\omega = 2\pi n / 60$. With increasing Re beyond Re_{cr}, laminar Taylor vortex flow becomes unstable (Coles, 1965). This instability leads to a wavy vortex flow. A critical Re where the flow transits from laminar Taylor vortex flow to wavy vortex flow has not strictly determined yet. According to Di Prima and Swinney (1981), the critical Re depends strongly on the radius ratio; it is about 1.05Re_{cr} to 1.10 Re_{cr} for R_{i} / R_{o} = 0.95 and is very much larger, 10Re_{cr} or greater, for R_{i} / R_{o} = 0.5. Therefore, it was inferred that this experimental *Re* range corresponded to the range form laminar Taylor vortex flow to wavy vortex flow. A high speed video camera system was used to record the bubble flow in the liquid. A plane sheet of semiconductor laser with the power of 50 W was used to illuminate the vertical cross-sectional flow field. Images of the bubble could be captured by the camera at a frame speed of 250 fps. After the inner cylinder had reached a certain rotational speed, each experiment was performed with an adequate time for vortical structures to form.

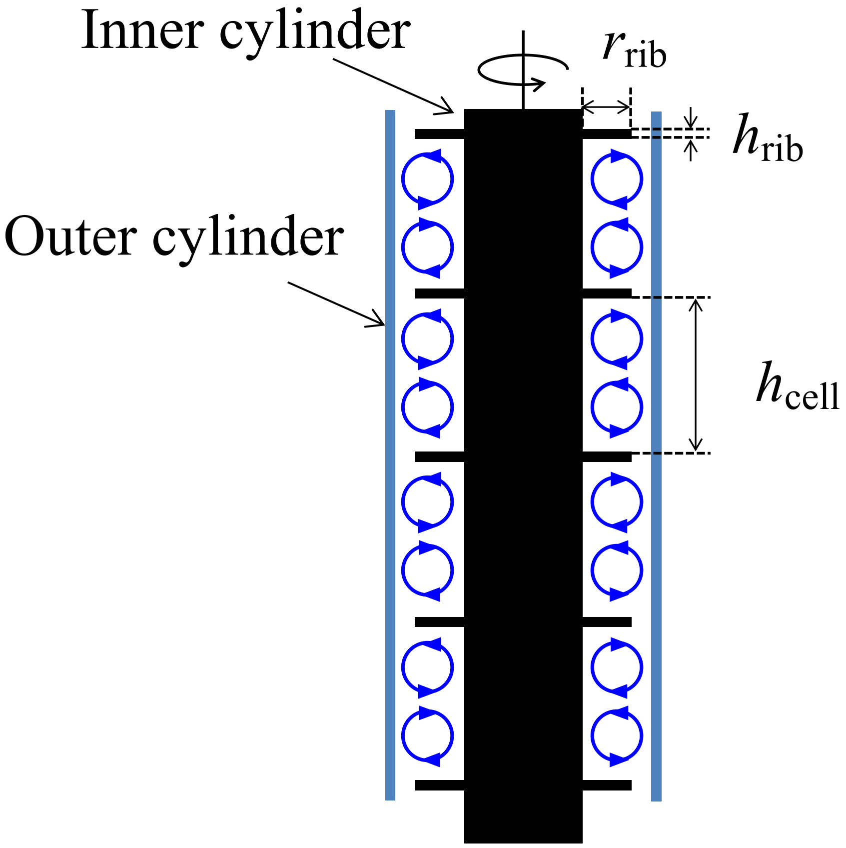

Fig. 4‒2 Schematic of the inner cylinder with ribs

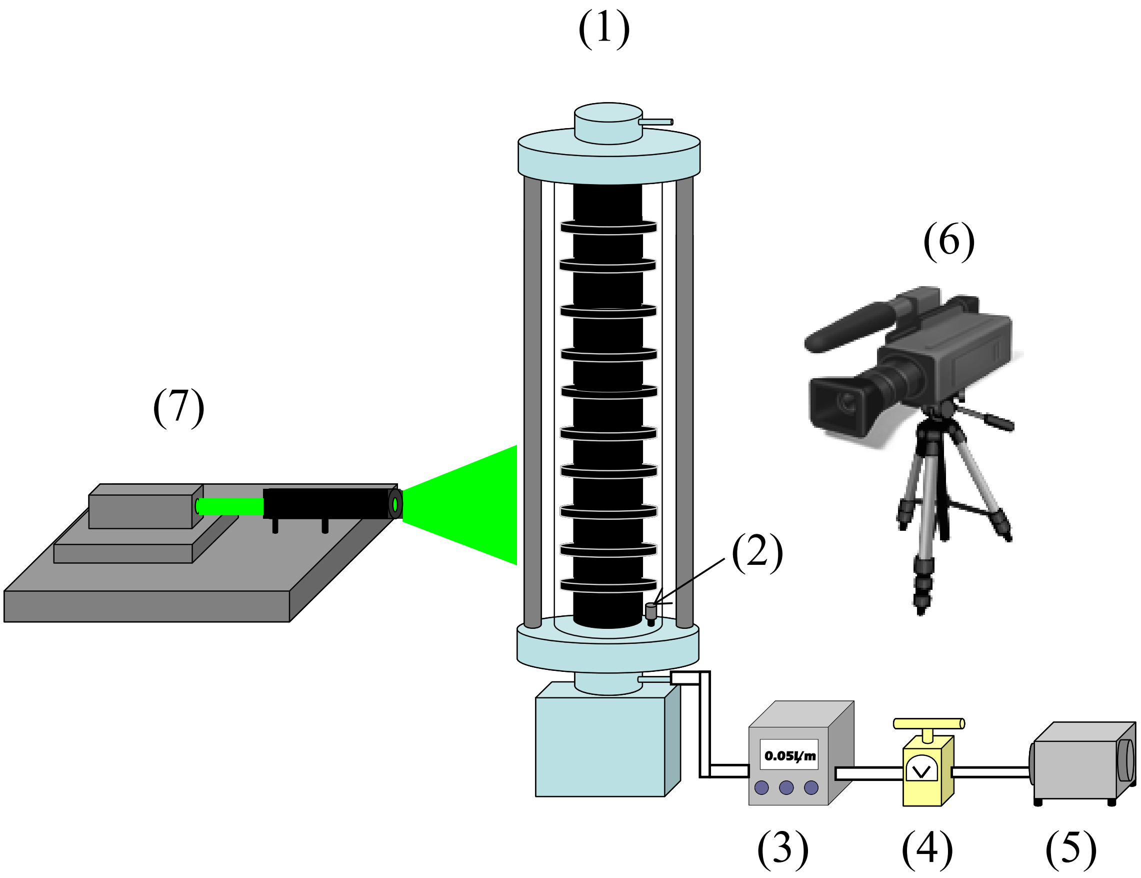

Fig. 4‒3 Experimental apparatus; (1) Taylor vortex flow device (2) sparger (3) flow meter (4) valve (5) compressor (6) video camera (7) laser

4. 3. Results and discussion

4. 3. 1. Vortex structure

Figure 4–4 shows flow visualization with aeration in front views of vortices by adding aluminum platelets with 20 μm. Because the trajectory of each cellular vortex flow differs from one to another, the state of light scattering also varies. As a result, each divided cellular vortex could be observed in **Fig. 4–4**. Clearer cell boundaries can be seen with the increase in the width of ribs, where two darker boundaries are inflow cell boundaries, while one boundary between the darker boundaries is the outflow boundary. In the case of no rib, r_{rib} = 4 and 6 mm, outflow boundary is not clear. Although a rib locates near the outflow boundary, it could not be observed because of suspended aluminum platelets. Without aeration, the operational condition in this study (Re = 913.6) is inferred in a transitional region from laminar Taylor vortex flow to wavy vortex flow. The structure and cell boundaries were apparently stable. With aeration, however, the Taylor vortex could not be generated when the centrifugal force was not enough to suppress the flow instability caused by the buoyancy of bubbles. The critical Reynolds number, Re_{cr}, for gas–liquid two-phase flow has not yet determined. The structure of vortices became unstable and unclear cell boundaries could be observed when ribs were not equipped. On the other hand, only slight periodic wave motion on the cell boundaries could be observed when r_{rib} = 4 and 6 mm. At r_{rib} = 8 mm, no wave motion could be seen. It can be considered that the buoyancy effect of bubbles was weakened by the ribs. However, at r_{rib} = 10 mm, random wave motion appeared on the cell boundaries. Coalescence of bubbles, which will be described in the next section, could be the reason for this phenomenon. These results indicate that a TCFR with a ribbed cylinder could certainly immobilize and stabilize vortices even in gas–liquid two-phase flow.

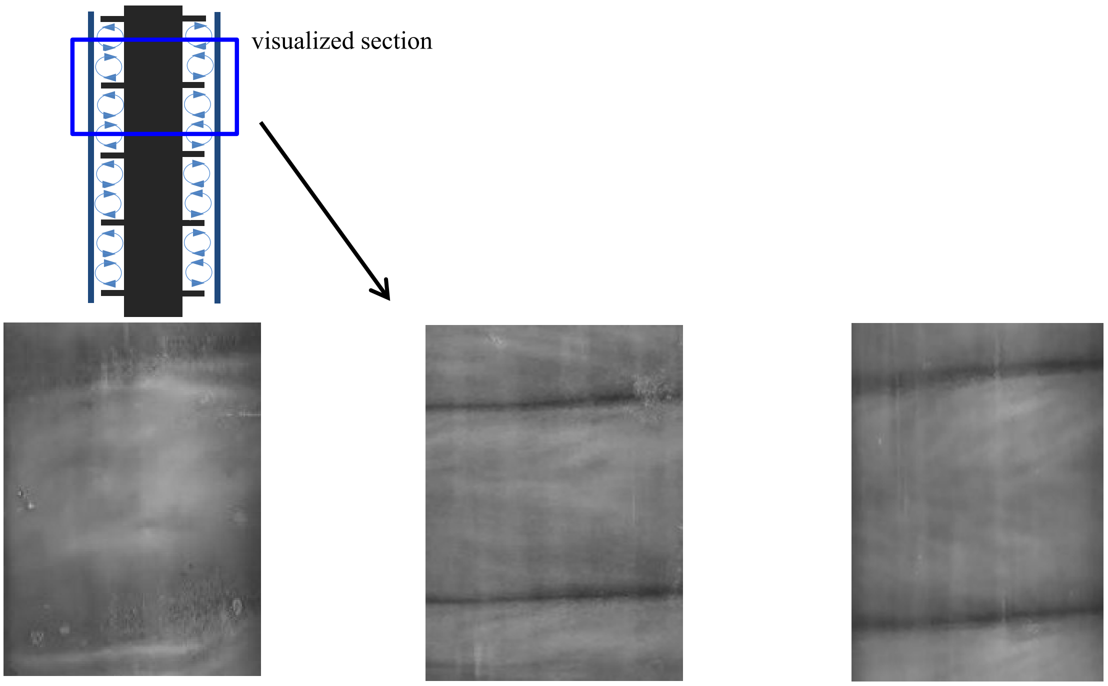

No rib

r_{rib} = 0.4 cm

r_{rib} = 0.6 cm

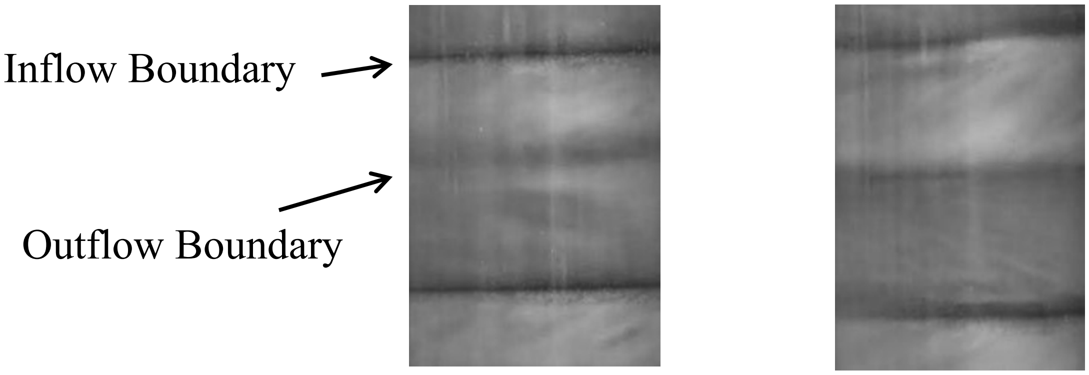

r_{rib} = 0.8 cm

r_{rib} = 1.0 cm

Fig. 4–4 Photographs of flow pattern at the same rotational speed of the rotor (n = 190 rpm, $V_G = 5.0 \times 10^{-6}$ m^3/s)

The stabilization of vortex structure can be inferred from intensification of a centrifugal force by a ribbed rotor. In order to clarify the effect of the ribbed rotor on the velocity field, numerical simulation was conducted using COMSOL Multiphysics® engineering simulation software. In this simulation, the fluid was considered as an incompressible Newtonian fluid in a steady state, and 2D axisymmetric was assumed. For simplicity, the injection of gas was neglected and the calculation region was limited to the one pair of vortex cell. The governing equations were the conservation equations of mass and momentum as shown in Eqs. (4–1) and (4–2):

$$\nabla \cdot \boldsymbol{u} = 0 \tag{4–1}$$

$$\frac{\partial \boldsymbol{u}}{\partial t} + (\boldsymbol{u} \cdot \nabla)\boldsymbol{u} = -\frac{\nabla p}{\rho} + \frac{1}{\rho}\nabla \cdot \left[\eta\left(\nabla \boldsymbol{u} + \nabla \boldsymbol{u}^{T}\right)\right] + \boldsymbol{g} \tag{4–2}$$

where $\boldsymbol{u}$ is the velocity, t is the time, p is the pressure, ρ is the density, η is the viscosity, $\boldsymbol{g}$ is the gravitational acceleration. The circumferential velocity was given by ωR_{i}. The top and bottom wall were assumed as the fixed wall. The number of grids was 2994, and the computational domain is shown in **Fig. 4–5**. *Re* was set at *Re* = 1105.9. **Figure 4–6** shows circumferential velocity distribution of liquid phase at the outflow boundary. The $(r-R_{\mathrm{i}})/d$ means the value of r in the axial direction is normalized by the gap width. The $U_{\theta}/(R_{\mathrm{i}}\cdot\omega)$ means the value of U_{θ} in the circumferential velocity is normalized by the tip velocity of the inner cylinder. This figure clearly shows that the circumferential velocity, U_{θ}, increased with r_{rib}. Higher circumferential velocity of fluid can provide a higher centrifugal force.

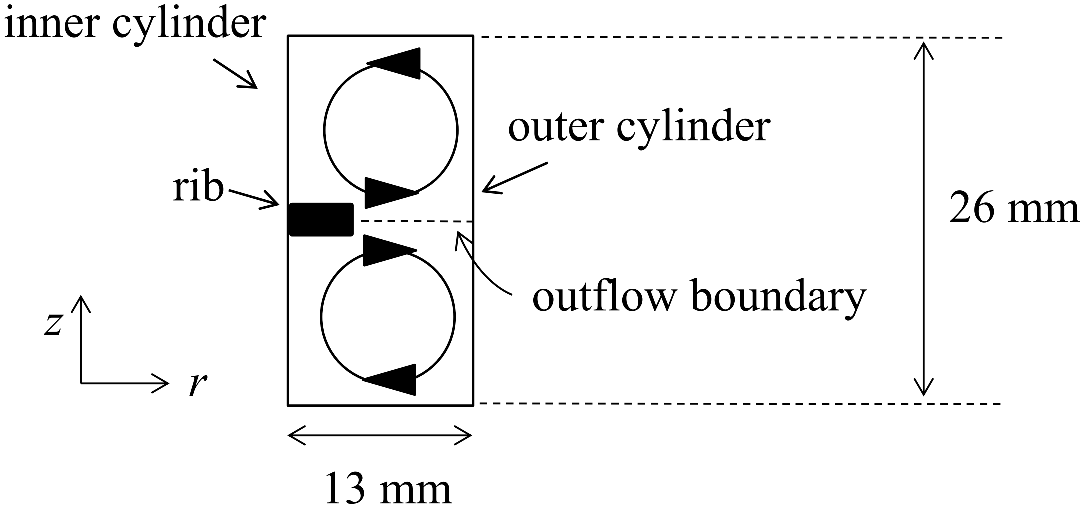

Fig. 4–5 Computational domain for the one pair of Taylor vortex cell with the ribbed rotor

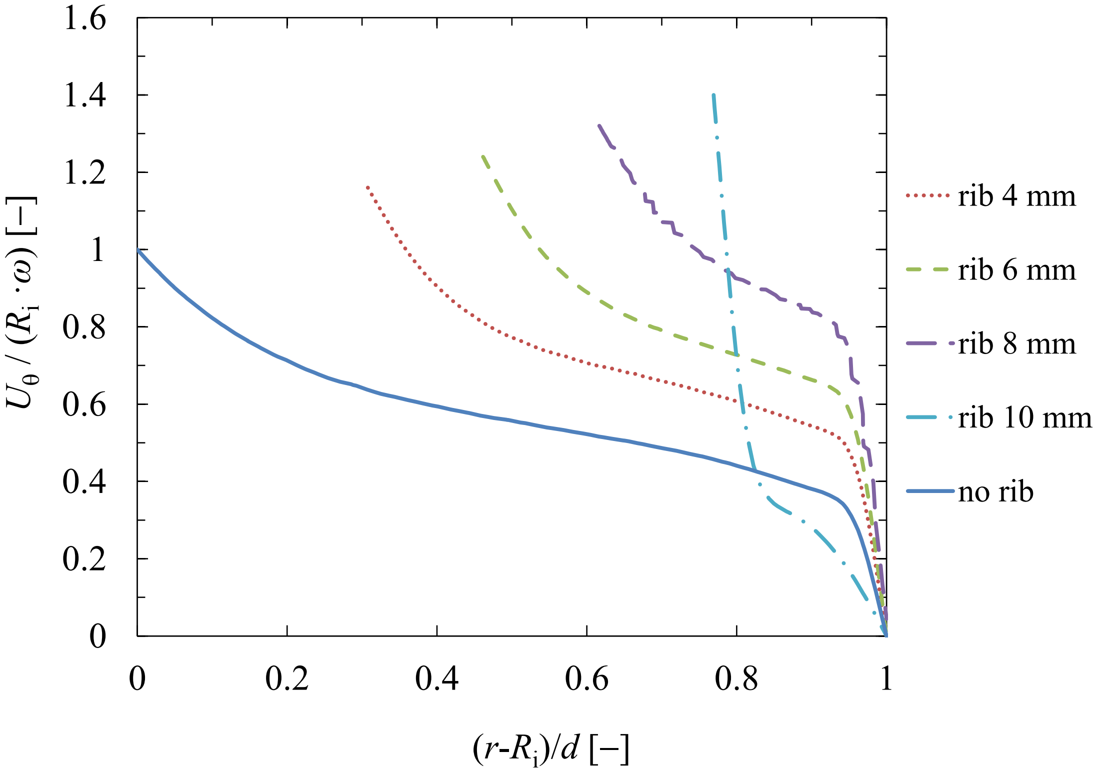

Fig. 4–6 Velocity distribution of circumferential flow in single phase flow
(ω = 24.1 rad/s, corresponds to n = 230 rpm)

Furthermore, **Fig. 4–7** shows the shear stress distribution, (a) no rib, (b) r_{rib} = 6 mm and (c) r_{rib} = 10 mm, in the annular space. Although the area of locally high stress region increased with increasing of r_{rib}, the area was quite small compared to whole area. Therefore, it is expected that a larger centrifugal force by the ribbed rotor intensified the rotational speed of the vortex and the structure of the vortex without enhancement of shear stress field.

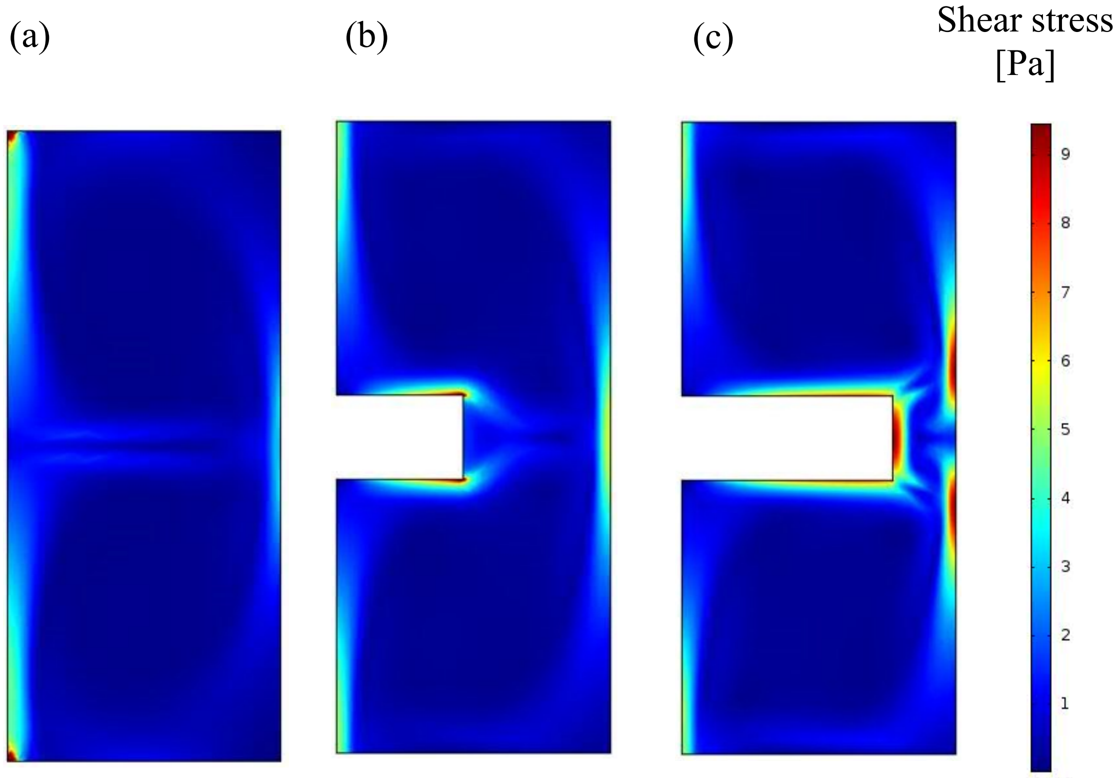

Fig. 4–7 Shear stress distribution for (a) no rib, (b) r_{rib} = 6 mm and (c) r_{rib} = 10 mm (ω = 24.1 rad/s, corresponds to n = 190 rpm)

4. 3. 2. Mean residence time of bubbles

Based on the above experiments, the ribbed TCFR can offer a promising prospect of holding many more bubbles within vortices. This promising prospect may result in increasing interfacial area at even low rotational speed of the rotor. The present work measured the gas hold–up and calculated mean residence time, τ, of gas defined by the following equation:

$$\tau = \frac{\pi\left(R_{\mathrm{o}}^2 - R_{\mathrm{i}}^2\right)\Delta H}{V_{\mathrm{G}}} \qquad (4\text{–}3)$$

where, ΔH [m] is the change of liquid height with aeration and V_{G} [m^3/s] is the gas flow rate. As shown in **Fig. 4–8**, ΔH is the difference in the height of the liquid phase with and without aeration (h_0 = 270 mm). ΔH was measured from the macrophotograph of the upper part of the liquid phase after aeration, which was filmed by a digital video camera.

Figure 4–9 indicates that the τ increased with rotational speed of the rotor. When wider ribs are employed, a stronger centrifugal force stabilizes vortices. It is expected that the stabilized vortices contained much more bubbles within vortices. Particularly when r_{rib} = 10 mm, the value of τ showed a significant increase. The effect of blocking bubbles due to the rib should be taken into consideration in this case.

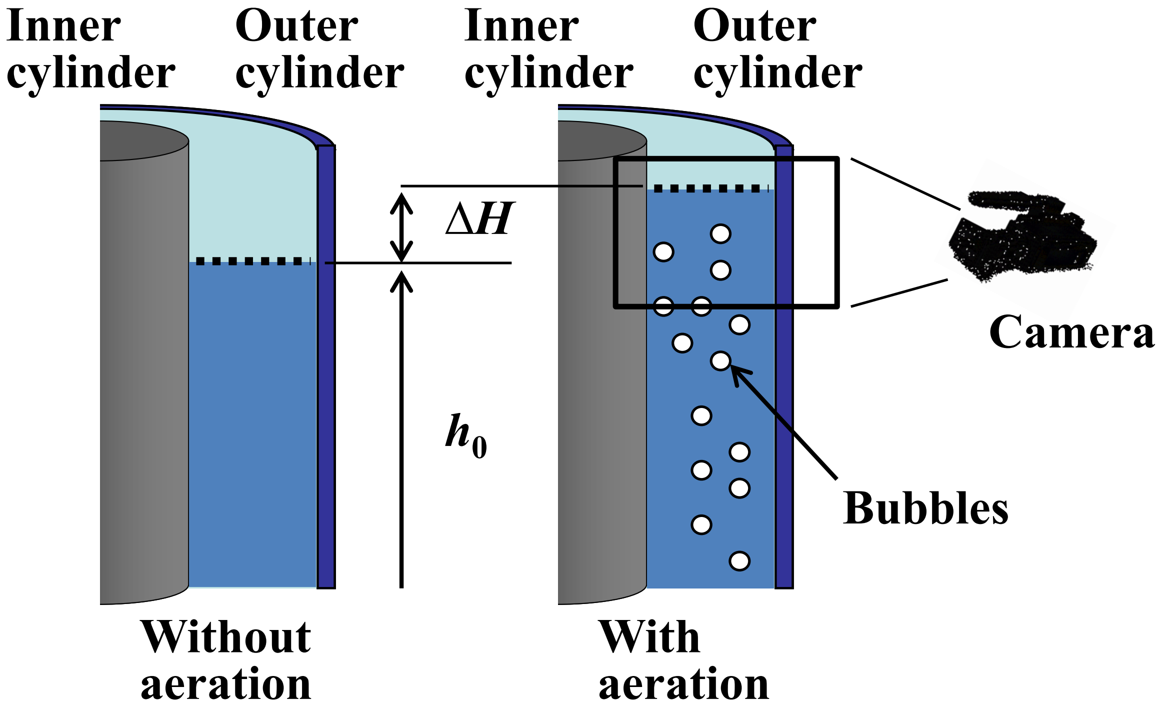

Fig. 4–8 Changes of liquid height with aeration

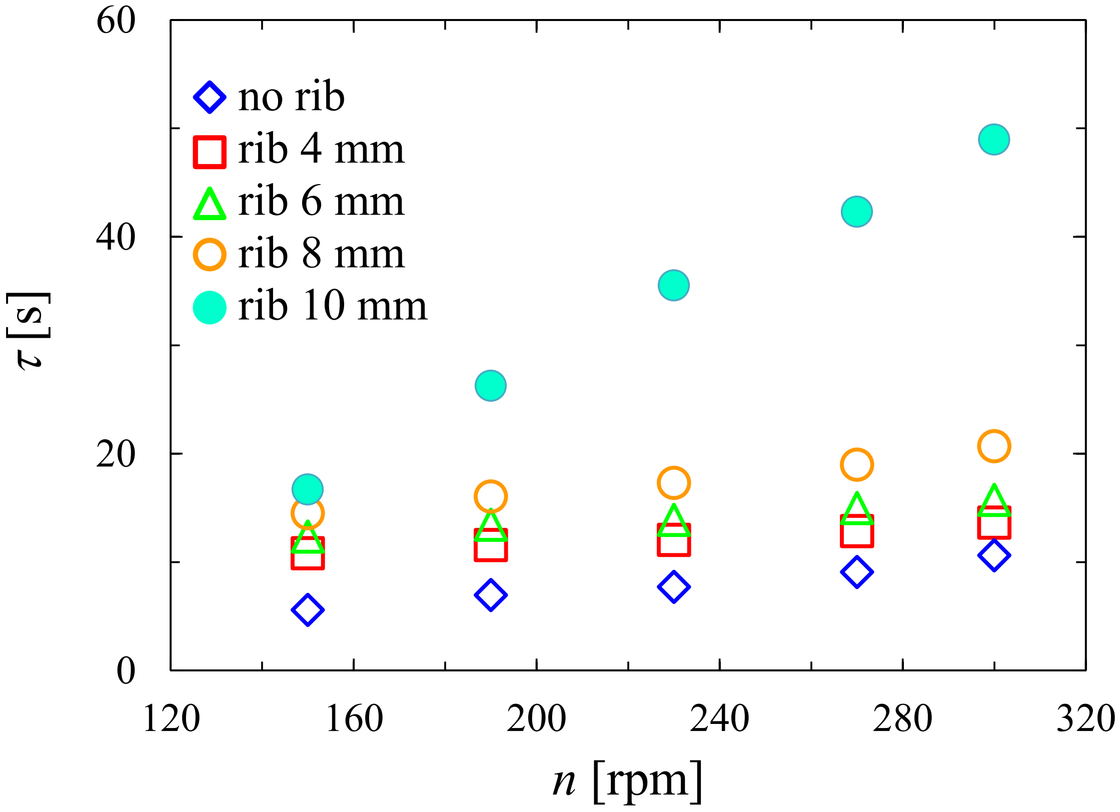

Fig. 4–9 Mean residence time of gas rotational speed of the rotor
($V_G = 5.0 \times 10^{-6}$ m^3/s)

4. 3. 3. Bubble size and interfacial area

The bubble diameter was measured by image analysis from cross-sectional views of the test section. **Figure 4–10** shows the effect of the width of ribs on bubble distribution in cross-sectional views between two ribs at n = 230 rpm and $V_{\mathrm{G}} = 8.33\times10^{-7}$ m^3/s. It was found that more bubbles were captured when wider ribs were employed. According to Bernoulli's law, it is inferred that the pressure at the vicinity of the rib tip becomes low because the circumferential flow velocity is fast. As an example, the pressure distribution at Re = 1105.9 without aeration for no rib and r_{rib} = 6mm is shown in **Fig. 4–11**. Bubbles tend to accumulate in the low-pressure regions located near the inner cylinder, which correspond to outflow boundary (Atkhen *et al.*, 2000; Climent *et al.*, 2007). Focusing on the upper rib, bubbles accumulated beneath the tip of the rib.

Figure 4–12 shows the effect of the rotational speed of the rotor on bubble distribution in cross-sectional views between two ribs at r_{rib} = 8 mm and $V_{\mathrm{G}} = 8.33\times10^{-7}$ m^3/s. As the increase in the rotational speed of the rotor, the bubble diameter increased significantly. This indicates that the strong vertical motion also enhanced bubble coalescence and reduced the number of bubbles.

These results shown in **Figs. 4–10** and **4–12** are summarized in **Fig. 4–13**. In order to represent the average bubble diameter, a Sauter mean diameter was used (Shah *et al.*, 1982; Vasconcelos *et al.*, 2003; Behkish *et al.*, 2007):

$$d_{32} = \frac{\sum_i N_i d_{b,i}^3}{\sum_i N_i d_{b,i}^2} \tag{4–4}$$

d_{32} was obtained from 50 bubbles diameter which were measured from enlarged **Figs. 4–10** and **4–12,** assuming spherical bubbles. It was observed that the mean bubble diameter drastically increased with the increase of rotational speed. In contrast, the wider the ribs were, the smaller the effect of rotational speed on the mean bubble diameter became. When r_{rib} = 10 mm, owing to the anomalous coalescence, bubbles were too large and deformed to measure the diameter.

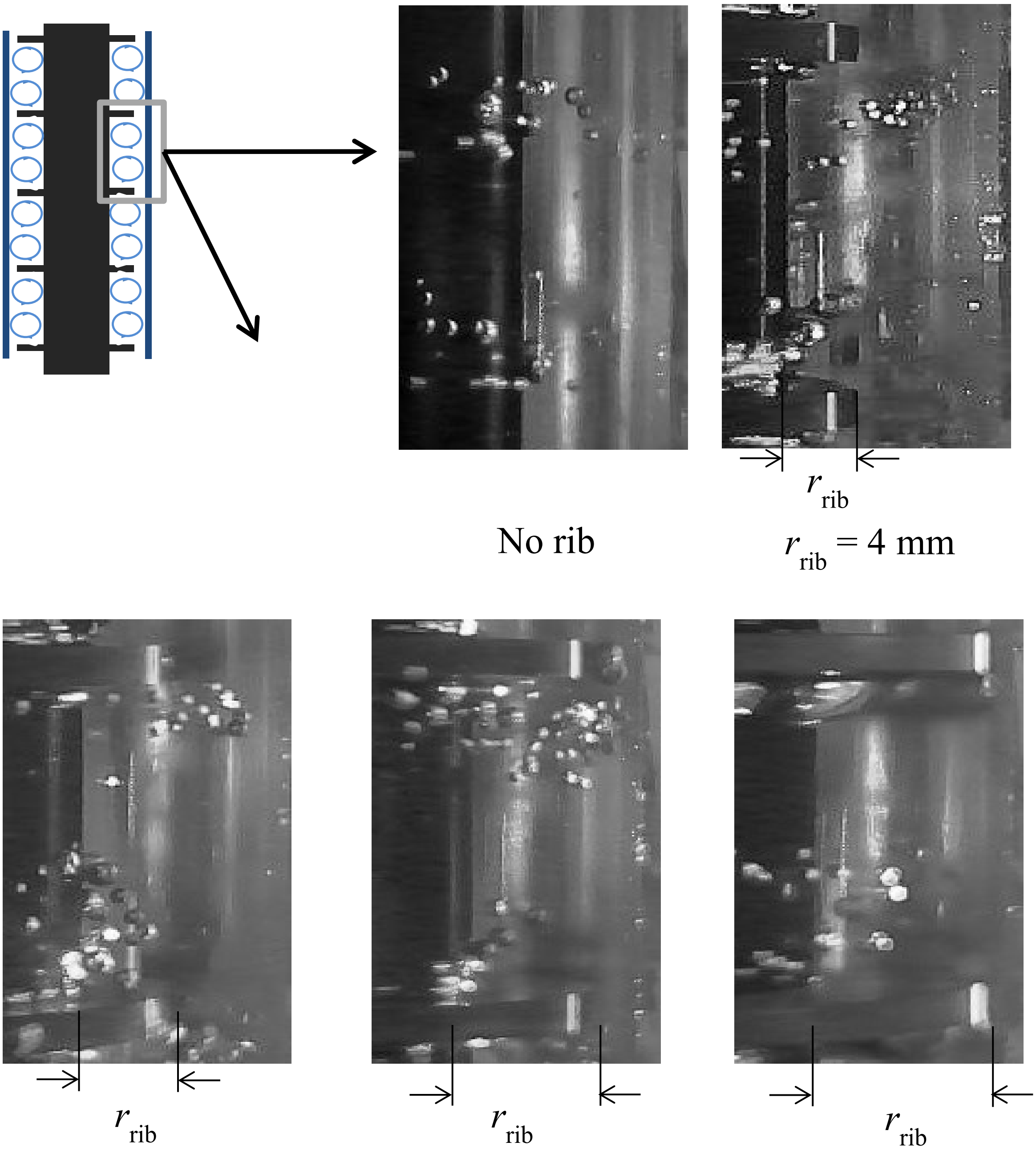

No rib

$r_{\mathrm{rib}} = 4$ mm

$r_{\mathrm{rib}} = 6$ mm

$r_{\mathrm{rib}} = 8$ mm

$r_{\mathrm{rib}} = 10$ mm

Fig. 4–10 Effect of the width of ribs
($n = 230$ rpm, $V_G = 8.33 \times 10^{-7}$ m^3/s)

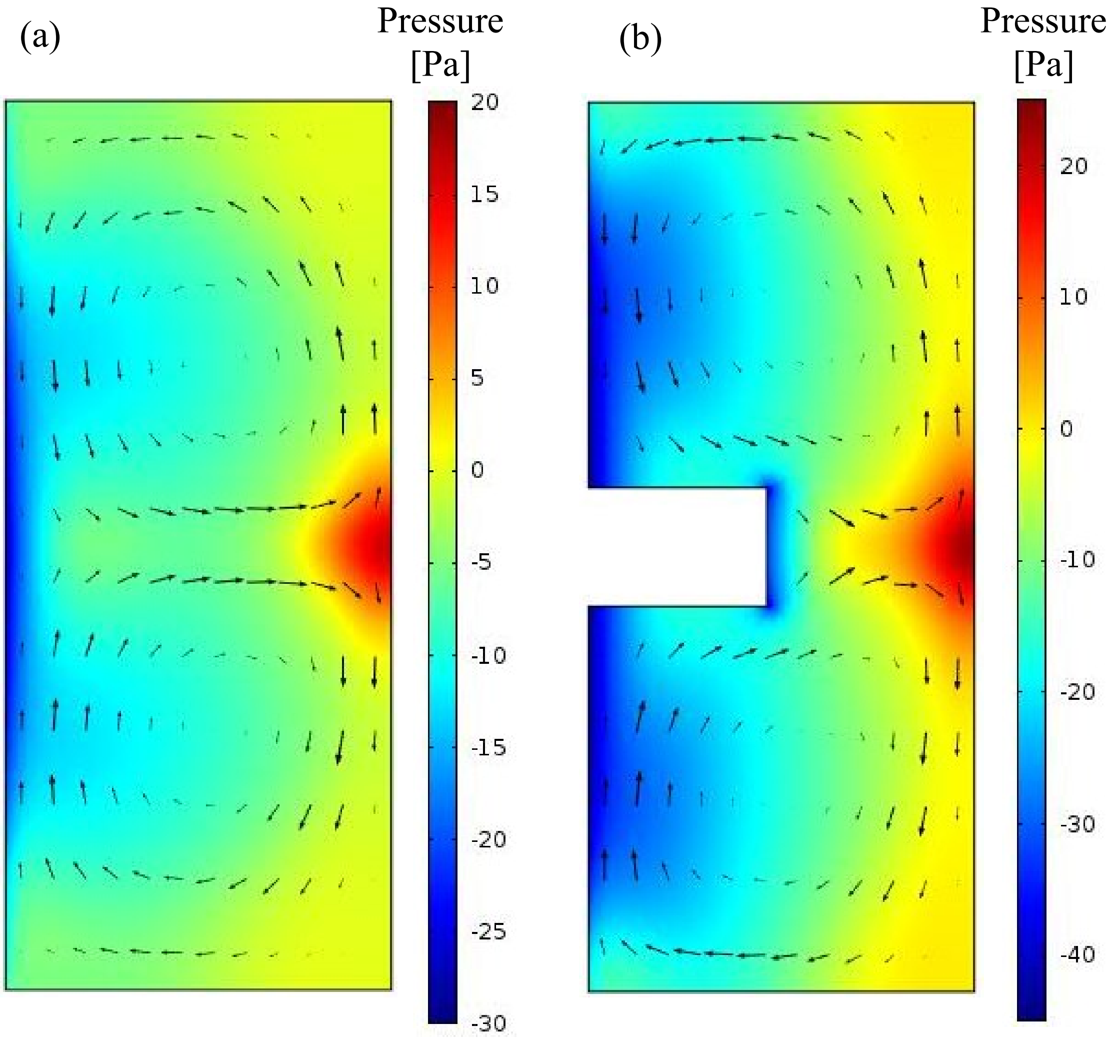

Fig. 4–11 Pressure distribution with velocity vector at $Re = 1105.9$
for (a) no rib, (b) $r_{\mathrm{rib}} = 6$ mm

n = 150 rpm n = 190 rpm n = 230 rpm

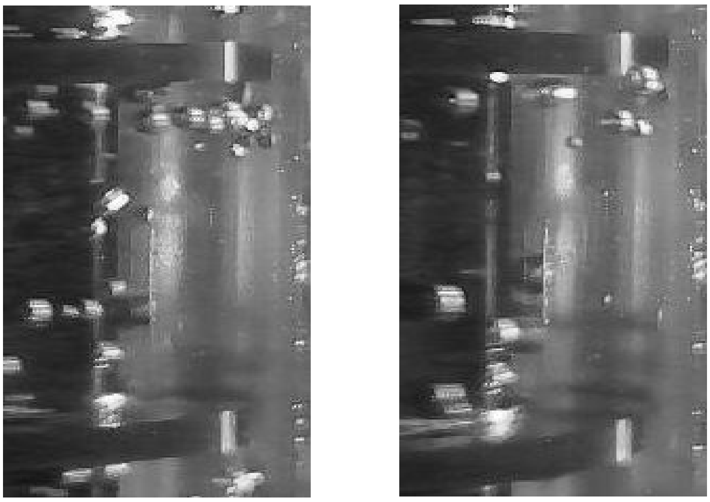

n = 270 rpm n = 300 rpm

Fig. 4–12 Effect of the rotational speed of the rotor
(r_{rib} = 8 mm, $V_G = 5.0 \times 10^{-6}$ m^3/s)

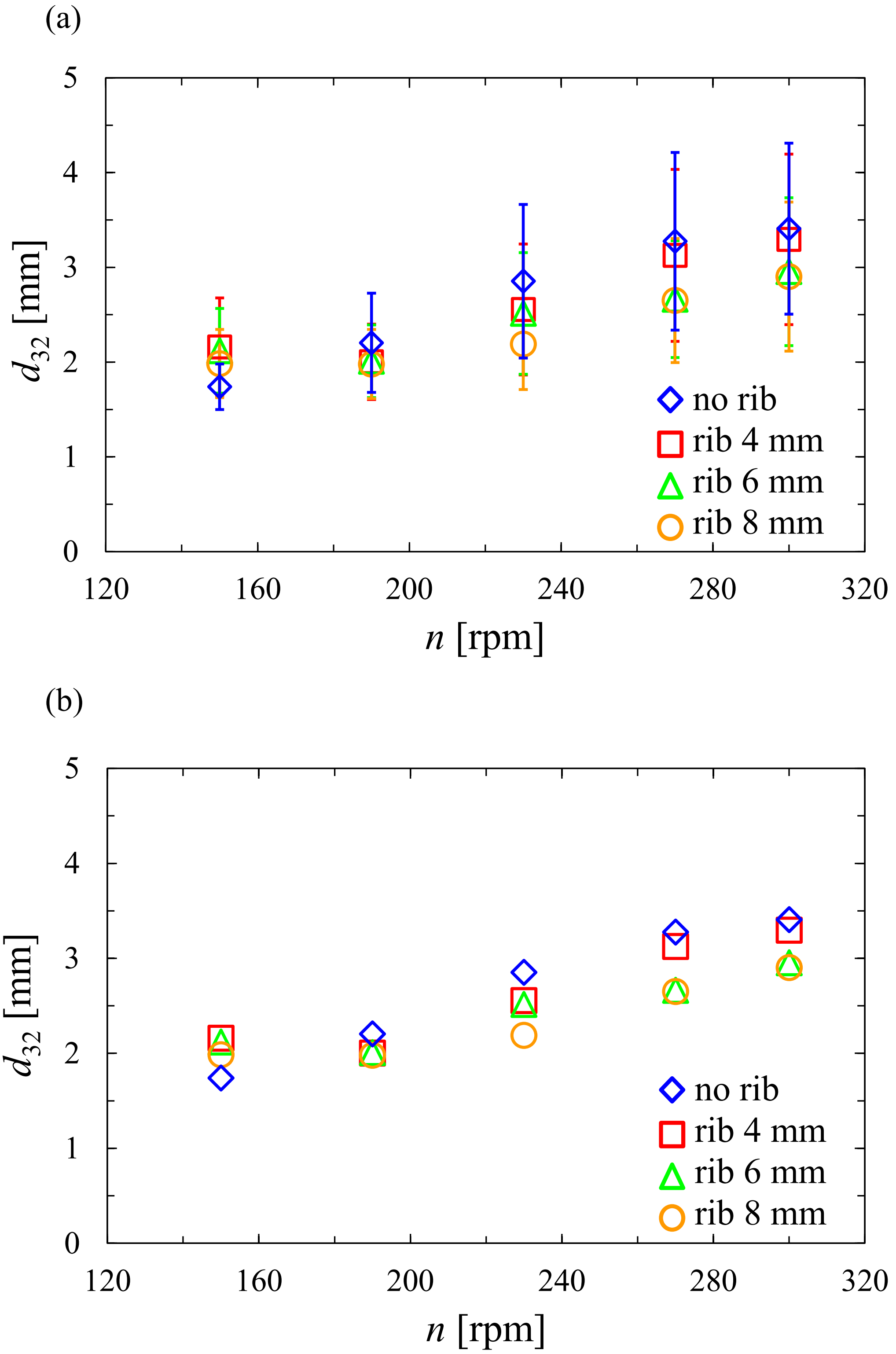

Fig. 4–13 Sauter mean bubble diameter against the rotational speed of the rotor ($V_G = 5.0 \times 10^{-6}$ m^3/s):
(a) with error bars and (b) without error bars

The increase of specific gas–liquid interfacial area between gas and liquid as well as gas hold–up is crucial for intensification of a gas–liquid contactor. Smaller bubbles are preferable for increasing the specific interfacial area. From the gas hold–up and bubble diameters, the specific gas–liquid interfacial area of the bubble is obtained by the following equation, assuming spherical bubbles (Popovic and Robinson, 1989):

$$a = \frac{6\varepsilon_{\mathrm{G}}}{d_{32}} \tag{4–5}$$

$$\varepsilon_{\mathrm{G}} = \frac{\Delta H}{h_0 + \Delta H} \tag{4–6}$$

where, ε_{G} [–] is gas hold–up. The mean diameter of bubbles as well as the gas hold–up increases with rotational speed owing to coalescence of bubbles. This trade–off relation resulted in that the specific gas–liquid interfacial area had a peak value against the rotational speed of rotor, as shown in **Fig. 4–14**. The above results suggest that there exists an optimum operational condition for the specific gas–liquid interfacial area in the TCFR with ribs. Furthermore, the specific gas–liquid interfacial area was drastically intensified by the ribbed inner cylinder. Especially, at n = 230 rpm, the specific interfacial area with r_{rib} = 8 mm was as about 2.5 times as the no rib inner cylinder.

Figure 4–15 shows the comparison between the data on specific interfacial area in stirred tank (Dłuska *et al.*, 2004) and the one in TCFR. Although the operational condition in stirred tanks is not optimized for the comparison with the TCFR, a simple comparison can be conducted. The experimental by Dłuska *et al.* (2004) was carried out in a stirred tank with total volume 2 L using a four pitched-blade turbine in O_2–NaOH solution system. It should be noted that the gas flow rate in their experiment, V_G = 1.25 × 10^{-5} m^3/s, was more than twice as large as the flow rate in study. Nevertheless, at the same rotational speed the higher value of a could be obtained by the TCFR with ribs. Therefore, it is expected that the reduction of apparatus size can be achieved by the TCFR with ribs compared to the traditional stirred tank. In future, the comparison of power consumption between the TCFR and the stirred tank should be discussed.

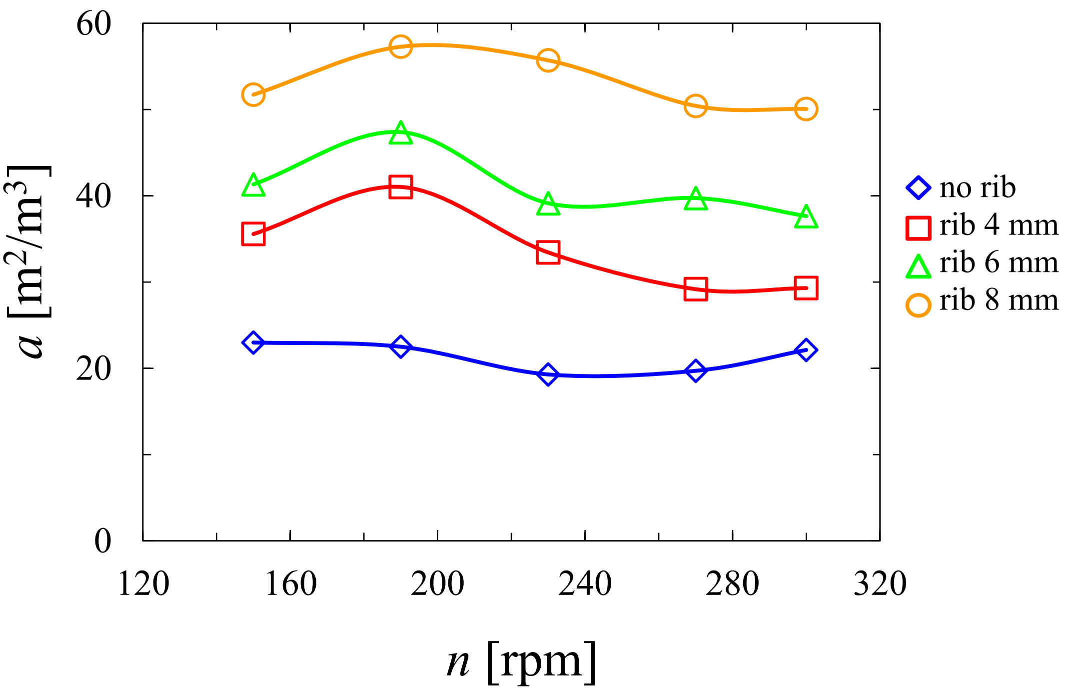

Fig. 4–14 Specific interfacial area between gas and liquid against the rotational speed of the rotor (V_G = 5.0 × 10^{-6} m^3/s)

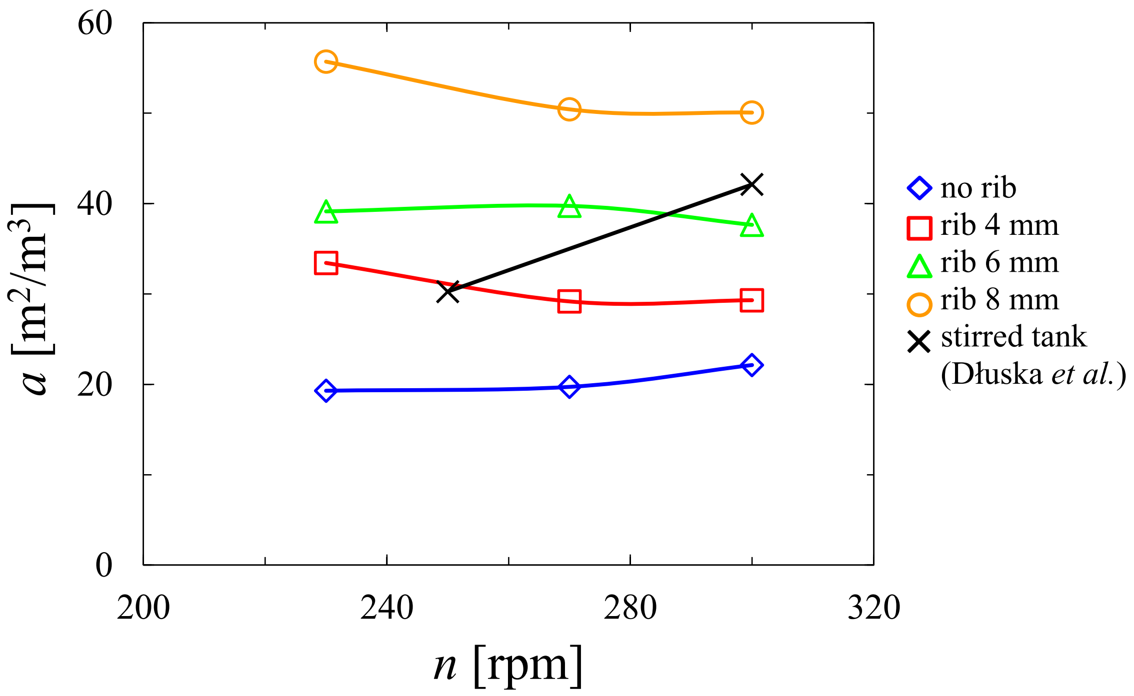

Fig. 4–15 Comparison of specific interfacial area
between the TCFR and the stirred tank
($V_G = 5.0 \times 10^{-6}$ m^3/s for the TCFR, 1.25×10^{-5} m^3/s for the stirred tank)

4. 4. Conclusions

The study in this chapter examined the performance of gas–liquid two-phase flow in a Taylor–Couette flow reactor (TCFR) with a ribbed inner cylinder. A pair of counter-rotating vortices appeared between two ribs, and the vortices were immobilized and stabilized even in gas–liquid two-phase flow. It was found that the mean residence time of gas largely increased with the ribbed rotors, and more bubbles were captured when wider ribs were employed. Bubbles tended to accumulate in the low pressure regions located near the inner cylinder, which correspond to the outflow boundary. While gas hold–up increased with r_{rib}, bubble diameter became larger as r_{rib} increases. This result indicates that bubble coalescence occurred.

On the other hand, because of the coalescence of bubbles, the mean diameter of bubbles also increased with rotational speed of the rotor. This trade–off relation resulted in the specific gas–liquid interfacial area, a, between gas and liquid having a peak value against the rotational speed of the rotor. This result suggests that there exists an optimum operational condition in the TCFR with ribs. Furthermore, from the fact that the specific interfacial area drastically increased with ribs, the TCFR with ribs has potential for process intensification. The higher value of a was obtained using the TCFR with ribs compared to the stirred tank. In future, the discussion about the comparison of power consumption between the TCFR with ribs and the stirred tank is required for the practical application of the TCFR with ribs.

Nomenclature

a : specific gas–liquid interfacial area, m^2/m^3

D_i : inner cylinder diameter, mm

D_o : outer cylinder radius, mm

d : gap width, mm

d_b : bubble diameter, mm

d_{32} : Sauter mean bubble diameter, mm

g : gravity (=9.8 m/s^2), m/s^2

h : height of TCFR, mm

h_{cell} : distance between ribs

h_{rib} : rib thickness, mm

h_0 : liquid height without aeration, mm

k_L : liquid side mass transfer, m/s

N : number of bubbles, -

n : rotational number of inner cylinder, rpm

p : pressure, Pa

r : radial position, m

Re : Reynolds number (=$\rho R_i \omega d/\eta$), -

Re_{cr} :critical Reynolds number, -

R_i : inner cylinder radius, mm

R_o : outer cylinder radius, mm

r_{rib} : rib width, mm

t : time, s

t_{e} : exposure time, s

U : velocity magnitude, m/s

U_{θ} : circumferential velocity, m/s

$\boldsymbol{u}$: velocity, m/s

u_{slip} : slip velocity, m/s

V_{G} : gas flow rate, m^3/s

z : axial position, m

Greek letters

ΔH : change of liquid height with aeration, mm

ε_G : gas hold–up, -

η : viscosity, Pa·s

λ : axial wavelength, m

ρ : density, kg/m^3

τ : mean residence time of gas, s

ω : angular velocity of inner cylinder, rad/s

References

K. Atkhen, J. Fontaine, J. E. Wesfreid, Highly turbulent Couette–Taylor bubbly flow patterns, *J. Fluid Mech.*, **422**, 55–68 (2000)

A. Behkish, R. Lemoine, L. Sehabiague, R. Oukaci, B. I. Morsi, Gas holdup and bubble size behavior in a large-scale slurry bubble column reactor operating with an organic liquid under elevated pressures and temperatures, *Chem. Eng. J.*, **128**, 69–84 (2007)

E. Climent, M. Simonnet, J. Magnaudet, Preferential accumulation of bubbles in Couette-Taylor flow patterns, *Phys. Fluids*, **19**, 083301 (2007)

D. Coles, Transition in circular Couette flow, *J. Fluid Mech.*, **21**, 385–425 (1965)

W. D. Deckwer, R. Burckhart, G. Zoll, Mixing and mass transfer in tall bubble columns, *Chem. Eng. Sci.*, **29**, 2177–2188 (1974)

R. Deng, C. -H. Wang, K. A. Smith, Bubble behavior in a Taylor vortex, *Phys. Rev. E*, **73**, 036306 (2006)

R. Deng, D. Y. Arifin, Y. C. Mak, C. H. Wang, Taylor vortex flow in presence of internal baffles, *Chem. Eng. Sci.*, **65**, 4598–4605 (2010)

R. C. Di Prima, H. L. Swinney, Instabilities and transition in flow between concentric rotating cylinders, in: *Hydrodynamic Instabilities and the transition to Turbulence*, Springer-Verlag, 139–180 (1981)

H. Djéridi, J. F. Favé, J. Y. Billard, D. H. Fruman, Bubble capture and migration in Couette–Taylor flow, *Exp. Fluids*, **26**, 233–239 (1999)

H. Djeridi, C. Gabillet, J. Y. Billard, Two-phase Couette–Taylor flow: Arrangement of the dispersed phase and effects on the flow structures, *Phys. Fluids*, **16**, 128–139 (2004)

E. Dłuska, S. Wroński, R. Hubacz, Mass transfer in gas–liquid Couette–Taylor flow reactor, *Chem. Eng. Sci.*, **56**, 1131−1136 (2001)

E. Dłuska, S. Wroński, T. Ryszczuk, Interfacial area in gas−liquid Couette−Taylor flow reactor, *Exp. Therm. Fluid Sci.*, **28**, 467−472 (2004)

G. N. Fokoua, C. Gabillet, A. Aubert, C. Colin, Effect of bubble's arrangement on the viscous torque in bubbly Taylor-Couette flow, *Phys. Fluids*, **27**, 034105 (2015)

H. Furukawa, T. Watanabe, Y. Toya, I. Nakamura, Flow pattern exchange in the Taylor–Couette system with a very small aspect ratio, *Phys. Rev. E*, **65**, 1−7 (2002)

X. Gao, B. Kong, M. Ramezani, M. G. Olsen, R. D. Vigil, An adaptive model for gas−liquid mass transfer in a Taylor vortex reactor, *Int. J. Heat Mass Transfer*, **91**, 433−445 (2015)

B. Haut, H. B. Amor, L. Coulon, A. Jacquet, V. Halloin, Hydrodynamics and mass transfer in a Couette–Taylor bioreactor for the culture of animal cells, *Chem. Eng. Sci.*, **58**, 777–784 (2003)

R. Hubacz, S. Wronski, Horizontal Couette−Taylor flow in a two-phase gas−liquid system: flow patterns, *Exp. Therm. Fluid Sci.*, **28**, 457–466 (2004)

E. Ikeda, T. Maxworthy, Spatially forced corotating Taylor–Couette Flow, *Phys. Rev. E*, **49**, 5218–5224 (1994)

A. M. Kliphuis, L. de Winter, C. Vejrazka, D. E. Martens, M. Janssen, R. H. Wijffels, Photosynthetic efficiency of Chlorella sorokiniana in a turbulently mixed short light-path photobioreactor, *Biotechnol. Prog.*, **26**, 687−696 (2010)

B. Kong, J. L. Shanks, R. D. Vigil, Enhanced algal growth rate in a Taylor vortex reactor, *Biotechnol. Bioeng.*, **110**, 2140–2149 (2013)

B. Kong, R. D. Vigil, Light-limited continuous culture of Chlorella vulgaris in a Taylor vortex reactor, *Environ. Prog. Sustainable Energy*, **32**, 884–890 (2013)

G. Li, X. Yang, H. Ye, CFD simulation of shear flow and mixing in a Taylor–Couette reactor with variable cross-section inner cylinders, *Powder Technol.*, **280**, 53–65 (2015)

R. Maryami, S. Farahat, M. J. Poor, M. H. S. Mayam, Bubbry drag reduction in a vertical Couette–Taylor system with superimposed axial flow, *Fluid Dyn. Res.*, **46**, 055504 (2014)

T. Mullin, C. Blohm, Bifurcation phenomena in a Taylor–Couette flow with asymmetric boundary conditions, *Phys. Fluids*, **13**, 136–140 (2001)

Y. Murai, H. Oiwa, Y. Takeda, Bubble behavior in a vertical Taylor-Couette flow, *J. Phys.: Conf. Ser.*, **14**, 143–156 (2005)

M. N. Noui–Mehidi, N. Ohmura, J. Wu, “A numerical study of Taylor vortex flow in a finite length tapered annulus, *J. Phys.: Conf. Ser.*, **14**, 20–29 (2005)

N. Patel, V. Choy, T. White, G. Munkvold, J. Thibault, Design of a novel Couette flow bioreactor to study the growth of fungal microorganism, *J. Biotechnol.*, **145**, 264–272 (2010)

M. K. Popovic, C. W. Robinson, Mass transfer studies of external-loop airlifts and a bubble column, *AIChE J.*, **35**, 393–405 (1989)

J. Qiao, C. M. J. Lew, A. Karthikeyan, C. H. Wang, Production of pex protein from qm7 cells cultured in polymer scaffolds in a Taylor–Couette bioreactor, *Biochem. Eng. J.*, **88**, 179–187 (2014)

M. Ramezani, B. Kong, X. Gao, M. G. Olsen, R. D. Vigil, Experimental measurement of oxygen mass transfer and bubble size distribution in an air-water multiple Taylor-Couette vortex bioreactor, *Chem. Eng. J.*, **279**, 286–296 (2015)

O. Richter, H. Hoffmann, B. Kraushaar-Czarnetzki, Effect of the rotor shape on the mixing characteristics of a continuous flow Taylor-vortex reactor, *Chem. Eng. Sci.*, **63**, 3504–3513 (2008)

O. Richter, H. Hoffmann, B. Kraushaar-Czarnetzki, Investigation of mixing in a rotor shape modified Taylor-vortex reactor by the means of a chemical test reaction, *Chem. Eng. Sci.*, **64**, 2384–2391 (2009)

Y. T. Shah, B. G. Kelkar, S. P. Godbole, W. –D. Deckwer, Design parameters estimations for bubble column reactors, *AIChE J.*, **28**, 353–379

Y. Shiomi, H. Kutsuna, K. Akagawa, M. Ozawa, Two-phase flow in an annulus with a rotating inner cylinder (flow pattern in bubbly flow region), *Nucl. Eng. Des.*, **141**, 27–34 (1993)

R. Song, T. Tanzeglock, M. Soos, M. Morbidelli, A. Périlleux, T. Solacroup, H. Broly, Minimizing hydrodynamics stress in mammalian cell culture through the lobed Taylor–Couette bioreactor, *Biotechnol. J.*, **6**, 1504–1515 (2011)

G. I. Taylor, Stability of a viscous liquid contained between two rotating cylinders, *Phil. Trans. Roy. Soc. A*, **223**, 289–343 (1923)

S. C. Tzeng, W. P. Ma, K. D. Huang, T. S. Wu, Flow structure in an inner rotating annular channel with ribbed wall cylinder, *Jpn. J. Appl. Phys.*, **44**, 8711–8715 (2005)

G. I. Taylor, Stability of a viscous liquid contained between two rotating cylinders, *Phil. Trans. Roy. Soc. A*, **223**, 289–343 (1923)

J. M. T. Vasconcelos, J. M. L. Rodrigues, S. C. P. Orvalho, S. S. Alves, R. L. Mendes, A. Reis, Effect of contaminants on mass transfer coefficient in bubble column and airlift contactors, *Chem. Eng. Sci.*, **58**, 1431–1440 (2003)

S. Wroński, E. Dłuska, R. Hubacz, E. Molga, Mass transfer in gas–liquid Couette–Taylor flow in membrane reactor, *Chem. Eng. Sci.*, **54**, 2963–2967 (1999)

S. Wroński, E. Dłuska, R. Hubacz, Studies of two-phase Couette-Taylor flow reactor performance, *Trends Chem. Eng.*, **9**, 55–63 (2005)

X. H. Zhu, D. Y. Arifin, B. H. Khoo, J. Hua, C. H. Wang, Study of cell seeding on porous poly (d, l-lactic-co-glycolic acid) sponge and growth in a Couette–Taylor bioreactor, *Chem. Eng. Sci.*, **65**, 2108–2117 (2010)

5. Conclusions

5. Conclusions

This thesis aimed to achieve PI of Taylor–Couette flow reactor (TCFR) by overcoming bottlenecks of complex fluid processes. The conclusions of each chapter are as follows.

In Chapter 2, the definition of Reynolds number (*Re*) for a Taylor–Couette flow with a shear-thinning fluid was discussed. Since the shear-thinning property causes spatial distribution of fluid viscosity in a TCFR, the effective *Re* (Re_{eff}) was defined based on an effective viscosity (η_{eff}) obtained by a numerical simulation. η_{eff} was the average viscosity using a weight of dissipation function. As a result, the following contents were clarified in Chapter 2.

- ☐ When R_i/R_o is greater than 0.71, Re_{cr} corresponded well with the theoretical value for Newtonian fluid. In contrast, in the TCFR with wider gaps (less than R_i/R_o = 0.71), Re_{cr} for shear-thinning fluids deviated from the theoretical Re_{cr}, especially for $n = 0.3$, due to a wider viscosity distribution.
- ☐ The $\dot{\gamma}_{\mathrm{eff}}$ estimated from η_{eff} in the rheological property was proportional to the rotational speed of the inner cylinder. The proportional constant, *k*, depended not only on the apparatus geometry but also on the rheological property.
- ☐ A correlation equation for calculating *k* from R_i/R_o and n was suggested. It was experimentally confirmed that the correlation equation made it possible to predict the critical condition without numerical simulation.

In Chapter 3, in order to intensify the non-Newtonian fluid process by converting batch to a continuous operation, the TCFR was employed. Starch gelatinization and saccharification were selected as typical examples of non-Newtonian fluid processes. Here, the flow condition was expressed by Re_{eff} defined in Chapter 2. The following contents were clarified in Chapter 3.

- ☐ The rotation of the inner cylinder played an important role for the initial stage of gelatinization because of an enhancement of heat transfer and mixing by Taylor vortex.
- ☐ The effect of temperature could not be observed for the case of 50 g/L starch concentration, but it did appear when the initial concentration was 100 and 150 g/L. This is because a portion of the starch was left ungelatinized in the gelatinization section and simultaneously gelatinized in the saccharification section.
- ☐ Saccharification experiments indicated that the product concentration increased with a higher rotation speed of the inner cylinder, up to the formation of Taylor vortex flow in the saccharification section. The concentration remained constant or slightly increased over the Re_{cr} for 50 or 150 g/L, respectively. However, above $Re_{\mathrm{eff}} = 700$, the C_{rs}/C_0 slightly decreased. It is assumed that the axial dispersion was promoted at higher Re_{eff}.
- ☐ Using the TCFR, starch suspension of high concentration could be efficiently and continuously hydrolyzed.

In Chapter 4, gas–liquid two-phase flow in a novel TCFR with a ribbed inner cylinder was experimentally and numerically investigated. In this device, a pair of counter–rotating vortices appears between two ribs. Principally, the effects of ribs on flow dynamics, gas hold–up, and specific interface area were investigated. The following contents were clarified in Chapter 4.

- ☐ The ribbed inner cylinder immobilized and stabilized Taylor vortices even in gas–liquid two phase flow due to the enhanced centrifugal force. As a result, more bubbles were trapped in Taylor vortices; consequently, the mean residence time of bubbles was increased.
- ☐ Bubbles tended to accumulate in the low pressure regions located near the inner cylinder, which correspond to the outflow boundary, and bubble coalescence occurred.
- ☐ Because of the coalescence of bubbles, the mean diameter of bubbles also increased with rotational speed of the rotor. This trade–off relationship resulted in the specific interfacial area between gas and liquid having a peak value against the rotational speed of the rotor. This result suggests that there exists an optimum operational condition for the specific interfacial area in the TCFR with ribs.
- ☐ The specific interfacial area drastically increased using the ribbed rotor. For example, at n = 230 rpm, the specific interfacial area with r_{rib} = 8 mm was about 2.5 times the area for no rib.

The results of Chapter 2 and 3 indicated that the TCFR has potential for PI of non-Newtonian fluid processes. Further, the results of Chapter 4 showed that the TCFR with the ribbed inner cylinder provides the excellent performance for mass transfer between gas and liquid with a mild shear stress field. Based on these results, the process of complex fluids including non-Newtonian fluid, chemical reaction and gas–liquid two-phase flow, such as food processes or bio-processes, could be intensified using the TCFR with the ribbed inner cylinder. This indicates that a detailed investigation for flow dynamics of non-Newtonian fluid with aeration will be required in the future. In this study, the investigation about flow transition for non-Newtonian fluids was limited especially to the region from Couette flow to laminar Taylor vortex flow. It is necessary to determine other transition regions, e.g. the transition to wavy Taylor vortex flow or turbulent flow, based on Re_{eff} proposed in this study. Also, the construction of Re_{eff} for shear-thickening fluid, viscoplastic fluid and viscoelastic fluid will be necessary. Further, although turbulence enhances mixing or heat/mass transfer, there are few studies about turbulent flow dynamics of non-Newtonian fluid. In future, these studies should be actively conducted. Further, the investigation about the mixing performance of Taylor vortex cell with non-Newtonian fluids is beneficial from both practical and hydrodynamic viewpoints. Finally, at the same power input, the performance of TCFR for chemical reaction with complex fluids should be compared with the performance of a traditional stirred tank reactor.

List of Achievements

Publications

<Chapter 2>

1. Hayato Masuda, Takafumi Horie, Robert Hubacz, Mitsuhiro Ohata and Naoto Ohmura:

“Numerical analysis of the flow of fluids with complex rheological properties in a Couette−Taylor flow reactor”

Theo. Appl. Mech. Japan, **63**, 25−32, (2015)

2. Hayato Masuda, Takafumi Horie, Robert Hubacz, Mitsuhiro Ohata and Naoto Ohmura:

“Prediction of onset of Taylor−Couette instability for shear-thinning fluids”

In preparation

<Chapter 3>

3. Hayato Masuda, Takafumi Horie, Robert Hubacz, Naoto Ohmura:

“Process intensification of continuous starch hydrolysis with a Couette−Taylor flow reactor”

Chem. Eng. Res. Des., **91**, 2259−2264 (2013)

<Chapter 4>

4. Hayato Masuda, Weibin Zheng, Takafumi Horie, Naoto Ohmura:

“Enhancement of gas hold-up with a Taylor vortex flow system equipped with ribs”

J. Chem. Eng. Japan, **46**, 27−32 (2013)

Presentations

Invited lecture

増田 勇人

テイラー・クエット流反応装置を用いた非ニュートン流体プロセスの強化

第 11 回反応工学部会若手会講演会, 2015（9 月　北海道大学）

International conferences

1. [Oral] Hayato Masuda, Takafumi Horie, Robert Hubacz, Noato Ohmura:
“Effects of mixing on starch hydrolysis using a Couette−Taylor flow reactor”
International Symposium on Mixing in Industrial Processes 8, Melbourne, Australia, 14th−17th, Sep., Session3 (2014)

2. [Oral] Hayato Masuda, Takafumi Horie, Robert Hubacz, Noato Ohmura:
“Numerical and experimental investigation of continuous starch hydrolysis with a Couette−Taylor flow reactor”
The 24th International Symposium on Transport Phenomena, Yamaguchi, Japan, 1st−5rd, Nov., pp. 402−407 (2013)

3. [Poster] Hayato Masuda, Takafumi Horie, Robert Hubacz, Noato Ohmura:
“Process intensification of continuous starch hydrolysis with a Taylor−Couette flow reactor”
14th European Conference on Mixing, Warsaw, Poland, 10th−13th, Sep., pp. 293−298 (2012)

4. [Poster] Hayato Masuda, Shinichiro Matsuka, Takafumi Horie, Robert Hubacz, Noato Ohmura:

“Continuous starch gelatinization and hydrolysis with a Taylor–Couette flow reactor”

The 3rd International Congress on Green Process Engineering (*GPE2011*), Kuala Lumpur, Malaysia, 6th–8th, Dec., ID 209, 8 pages (2011)

5. [Poster] Hayato Masuda, Weibin Zheng, Takafumi Horie, Naoto Ohmura:

“Enhancement of gas holdup with a Taylor vortex flow system equipped with ribs”

1st International Symposium on Multiscale Multiphase Process Engineering (*MMPE*), Kanazawa, Japan, 4th–7th, Oct., P–46, 5 pages (2011)

Domestic conferences

1. [口頭] 増田 勇人, 堀江 孝史, Hubacz Robert, 大村 直人

Carreau モデル流体における Taylor–Couette 流の有効レイノルズ数および流動特性:

第 63 回レオロジー討論会, 2015 （9 月　神戸大学）

2. [口頭] 増田 勇人, 堀江 孝史, Hubacz Robert, 大村 直人
テイラー・クエット流装置における Carreau モデル流体の代表粘度およびせん断速度:
化学工学会, 第 47 会秋季大会, 2015 （9 月　北海道大学）
3. [口頭] 増田 勇人, 堀江 孝史, Hubacz Robert, 大村 直人
shear-thinning 流体におけるテイラー・クエット流の流動遷移:
化学工学会, 第 80 年会, 2015 （3 月　芝浦工業大学）
4. [口頭] 増田 勇人, 堀江 孝史, Hubacz Robert, 大村 直人
クエット・テイラー流装置における shear-thinning 流体流れの数値解析:
第 28 回数値流体力学シンポジウム, 2014 （12 月　東京 タワーホール船堀）
5. [口頭] 増田 勇人, 堀江 孝史, Hubacz Robert, 大村 直人
クエット・テイラー流反応装置における複雑なレオロジー特性をもつ流体の流動状態の数値解析:
第 63 回理論応用力学講演会(NCTAM2014), 2014 （9 月　東京工業大学）
6. [口頭] 増田 勇人, 堀江 孝史, Hubacz R, 大村 直人
連続式クエット・テイラー流装置を用いたデンプン加水分解における流動状態の効果:
化学工学会, 第 79 年会, 2014 （3 月　岐阜大学）
7. [口頭] 増田 勇人, 堀江 孝史, Hubacz Robert, 大村 直人

テイラー・クエット流反応装置を用いたデンプン連続糖化プロセス強化:
化学工学会, 第78年会, 2013 （3月　大阪大学）

8. [口頭] 堀江 孝史, 増田 勇人, Hubacz Robert, 大村 直人
テイラー・クエット流反応装置を用いた連続操作による糖化プロセス強化:
化学工学会, 第77年会, 2012 （3月　工学院大学）

Awards

1.神戸大学大学院工学研究科プレミアムアワード, 2014年2月

2.化学工学会　粒子・流体プロセス部会　シンポジウム賞（プレゼンテーション賞）, 2015年9月

Acknowledgement

First and foremost, I would like to my deepest gratitude to my supervisor Prof. Dr. Naoto Ohmura of Department of Chemical Science and Engineering in Kobe University, for his continuous encouragement, valuable suggestions and productive discussions. Also, I have been attracted by his warm personality. It would be impossible to accomplish my doctoral dissertation without his encouragement and guidance. He gave me many opportunities, e.g. presentations in conferences, and studying abroad in Poland. Through these experiences, I could grow up as not only a person but also a researcher.

I am very grateful to Assistant professor Dr. Takafumi Horie of Department of Chemical Science and Engineering in Kobe University, for his fruitful discussions, patient guidance, and technical support. He was sometimes kind, and sometimes strict. I was really happy that I spent time under his guidance. When I was depressed, he cheered me up. I appreciate all his help.

I am also grateful to Mr. Norihisa Kumagai of Department of Chemical Science and Engineering in Kobe University, for his experimental support, kind suggestions and encouragement.

I would like to thank Assistant professor Dr. Robert Hubacz of Faculty of Chemical and Process Engineering in Warsaw University of Technology, for his valuable suggestions and productive discussions. During my stay in Poland, he and his wife supported me. I could spend precious time thanks to them.

I would like to express my sincere gratitude to Prof. Dr. Mitsuhiro Ohta of Department of Energy System, Institute of Technology and Science in The University of Tokushima for his precious suggestions, helpful discussions, reviewing the thesis and

valuable advices. He always supported my research life.

I wish to express my special thanks to Prof. Dr. Akio Tomiyama of Department of Mechanical Engineering in Kobe University, and Prof. Dr. Hiroshi Suzuki of Department of Chemical Science and Engineering in Kobe University, for reviewing the thesis and their precious advices.

I would like to thank Associate professor Dr. Yoshiyuki Komoda of Department of Chemical Science and Engineering in Kobe University, for providing some laboratory and analytical equipment.

I also would like to thank Prof. Dr. Satoru Nishiyama, Associate professor Dr. Hironobu Imakoma, Associate professor Dr. Tooru Ooya, Associate professor Dr. Chiaki Ogino, and Assistant professor Dr. Keita Taniya of Department of Chemical Science and Engineering in Kobe University, for their valuable advices and warm support.

I would like to express my gratitude to Ms. Emi Okamura in Transport Science and Engineering Laboratory in Kobe University for her support and encouragement.

I am grateful to all staffs in Department of Chemical Science and Engineering in Kobe University. KTC are acknowledged for the financial support.

This research was partially supported by the Ministry of Education, Science, Sports and Culture of Japan, Grant-in-Aid for Scientific Research (A), (No. 20246115) from the Japan Society for the Promotion of Science (JSPS). I am grateful to JST (Japan Science and Technology Agency) for its financial support on this project (A-STEP No. AS231Z04343B).

I would like to thank all colleagues in Transport Science and Engineering Laboratory and Drying Process Engineering Laboratory in Kobe University. Thank you to Tatsuyuki Esaki, Naoko Hamashima, Yusuke Ozawa, Hisato Tanaka, Michinobu Sato,

Daichi Nagatmo, Hironobu Uenishi, Ayumi Enomoto, Mayuko Nabata, Ayuna Yamane, Takaaki Akagi, Koki Tanaka, Naoki Yamashita and, Kenta Hirai for their experimental support and encouragement.

Finally, I wish to deepest gratitude to my family, Ichiro Masuda, Misako Masuda, Risa Masuda and grandfathers and mothers, Tamio Masuda, Michiko Masuda, Tadao Sato, Kyoko Sato for their great and warm support. I could spend wonderful days at Kobe University, thanks to them.

January, 2016

Hayato Masuda

Doctor Thesis, Kobe University
“Process intensification of Taylor–Couette flow reactor with complex fluids”, 159 pages
Submitted on January 22, 2016
The date of publications is printed in cover of repository version published in Kobe University Repository Karnel.